9-12-2014

Optically Pumped Type-II Mid-Infrared Tunable Distributed Feedback Lasers

Xiang He

Candidate

Department

This dissertation is approved, and it is acceptable in quality and form for publication:

Approved by the Dissertation Committee:

, Chairperson

Optically Pumped Type-II Mid-Infrared Tunable Distributed Feedback Lasers

by

Xiang He

B.S., Optoelectronics, Harbin Institute of Technology, P. R. China, 1997

M.S., Optical Science and Engineering, University of New Mexico, 2008

DISSERTATION

Submitted in Partial Fulfillment of the

Requirements for the Degree of

Doctor of Philosophy

Optical Science and Engineering

The University of New Mexico

Albuquerque, New Mexico

July, 2014

Dedication

To

my parents, Youfeng He and Yonglian Liu,

my brother and sister in-law, Jiang He and Ping Du

for unconditional support, encouragement and patience through all these years.

Acknowledgments

I would like to thank my advisor, distinguished Professor Steven R. J. Brueck, for his supports, streaming knowledge, expertise and insightful guidance through all these years of my study and work in his research group. I can't imagine a better mentor for my graduate study and research.

I would like to thank Dr. Ron Kaspi from Air Force Research Laboratory (AFRL) who grew the samples for this project, loaned me equipments for device characterization and gave thoughtful advices. Without samples and the previous research carried out in his research group in AFRL, I would not be able to fabricate these tunable DFB laser devices.

I am also deeply grateful to my committee member, professor Mansoor Sheik-Bahae and Professor Peter Eliseev for their advices, guidance and supports.

I also want to thank Dr. Steve Benoit for his contribution to the device simulation work as well as helps in chirped grating calculation in this project.

I appreciate Joseph Chavez and other members in Dr. Kaspi's group in AFRL for device lapping, cleaving and bonding and all kinds of help. They also conducted tests on some of the devices to confirm and compare with what I did here in the Center for Hight Technology Materials (CHTM).

Finally, I would like to thank Andrew Frauenglass, Dr. Liang, Xue, Dr. Alexander Neumann, Dr. Yuliya Kuznetsova, Dr. Alexander Raub, other group members and all other faculty, staff and students at CHTM for their help and friendship.

Optically Pumped Type-II Mid-Infrared Tunable Distributed Feedback Lasers

by

Xiang He

B.S., Optoelectronics, Harbin Institute of Technology, P. R. China, 1997

M.S., Optical Science and Engineering, University of New Mexico, 2008

Ph. D., Optical Science and Engineering, University of New Mexico, 2014

Abstract

Optically-pumped type-II mid-infrared index-coupled tunable distributed feedback (DFB) semiconductor lasers have been developed to provide continuous-wave (CW) single longitudinal mode (SLM) operation with features including narrow spectral linewidth, high output power, good beam quality and wide continuous wavelength tunability for applications such as remote sensing or spectroscopy in the 3 to 5 μm midwave-infrared range of atmospheric transmission window.

In the demonstration of this type of laser, a hyperbolically chirped grating was patterned using interferometric lithography (IL) with spherical wavefronts which was then transferred into the top clad of the slab waveguide epi-structure of the laser device. Wavelength tuning is achieved by translationally projecting pump stripe at

different positions of this chirped grating on the laser device, thus different grating periods along the pump stripe at different pump positions select different lasing wavelengths. Primary results were acquired on one device of 4 mm in lateral dimension with continuously tuning range of about 80 nm centered at 3100 nm, single facet output power of 830 mW and typical spectral linewidth of 1.2 nm at 2.5×threshold pumping. Fabry-Perot (F-P) interferometer was used as artificial target gas to demonstrate potential application of gas spectroscopy with this type of laser.

Contents

List of Figures

List of Tables

Glossary

Abbreviations

AR	Anti-Reflection
ARC	Anti-Reflection Coating
CMT	Coupled Mode Theory
DAQ	Data Acquisition
DBR	Distributed Bragg Reflector
DFB	Distributed Feedback (Laser)
DL	Diode Laser
FMS	Frequency Modulation Spectroscopy
FNC	Facet Normal Configuration
FOM	Figure of Merit
F-P	Fabry-Perot
FSR	Free Spectral Range

FWHM	Full Width Half Maximum
GCAA	Grating Assisted Co-Directional Coupler
GCSR	Grating Coupled Sampled-Reflector
GNC	Grating Normal Configuration
HR	High Reflection
IA	Integrated Absorber
ICL	Interband Cascade Laser
ICP	Inductively Coupled Plasma (Etcher)
IL	Interferometric Lithography
LEF	Linewidth Enhancement Factor
LN_2	Liquid Nitrogen
LSHB	Lateral Spatial Hole Burning
MBE	Molecular Beam Epitaxy
MEMS	Micro-Electro-Mechanical System
Mid-IR	Middle Infrared
MMI	Multi-Mode Interface
OPSL	Optically Pumped Semiconductor Laser
PEB	Post Exposure Bake
PL	Photo-Luminescence

ppb	Part Per Billion
PR	Photoresist
QCL	Quantum Cascade Laser
QD	Quantum Dot
QW	Quantum Well
QWire	Quantum Wire
RT	Room Temperature
SEM	Scanning Electron Microscope
SG	Sampled Grating
SHB	Spatial Hole Burning
SLM	Single Longitudinal Mode
SMSR	Side Mode Suppression Ratio
SNR	Signal Noise Ratio
SOA	Semiconductor Optical Amplifier
SSG	Super-Structure Grating
TE	Transverse Electric (Field)
TLAS	Tunable Laser Absorption Spectroscopy
TMM	Transfer Matrix Method
VCSEL	Vertical Cavity Surface Emitting Laser

WDM	Wavelength Division Multiplexing
WDMA	Wavelength Division Multiple Access
WMS	Wavelength Modulation Spectroscopy

Customized Definition

Lateral Chirp	Grating period variation along the direction of the grating lines, or in the direction normal to the pump stripe.
Longitudinal Chirp	Grating period variation perpendicular to the grating line orientation or along the pump stripe.

Symbols

Γ	Confinement Factor
Λ	Grating Period
θ	Incident Angle of Interfering Beams
β	Sample/Die Tilting Angle
α	Sample/Die Azimuthal Rotation Angle or Grating Tilting Angle
κ	Coupling Coefficient
κL_g	Coupling Strength, L_g is length of grating

Chapter 1

Introduction to Distributed Feedback Lasers

1.1 Overview

Distributed Feedback (DFB) lasers are laser devices with spatially periodic (some times, even quasi-periodic or aperiodic) corrugation structure such as grating or other form of refractive index modulation along the entire length of gain medium or cavity, in which the periodic structure provides coherent distributed reflection as optical feedback to select and lock the laser to operate at a single longitudinal frequency. A DFB laser was first demonstrated by Kogelnik and Shank in an optically pumped gelatine medium in 1971 [1]. DFB lasers should not be confused with distributed Bragg reflector (DBR) lasers which have gratings as distributed feedback mirrors on either end or even arbitrary sections of the cavity, although both DFB and DBR lasers utilize distributed reflection for longitudinal mode selection. For further knowledge or related concepts about DFB lasers, please refer to these text books [2–8].

Depending on the location of the periodic corrugation structure relative to the ac-

tive region, DFB lasers are categorized into index-couple, gain-coupled and complex-coupled types [9–11]. Simply speaking, for the case that the periodic structure is located outside of the active region or in the cladding layers if the laser cavity takes a waveguide form, then this periodic structure only modulates the real part of the refractive index and is an index-coupled DFB laser. In comparison, gain-coupled DFB lasers have the periodic corrugation inside the gain medium/active region of the device, essentially with periodic modulation of the imaginary part of the refractive index. Complex-coupled DFBs are those have the combination of index and gain coupling. Our tunable DFB laser to be presented in this dissertation falls into the index-coupled DFB category. For index-coupled DFB lasers, the gain medium involves relatively simple epitaxial growth procedure without active region regrowth or post-growth as required by gain-coupled DFBs because the periodic structure could be patterned prior to or after the active region is grown. The main drawback of this type of DFB laser devices is that they don't operate exactly at Bragg wavelength defined by the product of grating period and effective refractive index because of existing stop band [12] or in other words the the oscillation condition can't be reached at the exact Bragg wavelength. What is even worse is that two degenerate DFB modes symmetric with respect to the Bragg frequency might lase at the same time or hop between one and the other in operation due to their similar lasing thresholds. This is not only undesirable but also against the intention of the introduction of a grating for single-longitudinal mode operation. Due to the imperfect fabrication such as unequal fractional facet periods in the process of device facet cleaving, these two degenerate DFB modes could have asymmetric thresholds such that only one mode lases. But two modes lase simultaneously or mode hopping between the two could still happen under different especially high pump power conditions, without extra controls. This problem can be partially solved with anti-reflection (AR) and high-reflection (HR) coatings on the laser device's front and rear facet respectively or any forms of unequal loss introduced to these two degenerate DFB modes. Even

though the difference of front/rear facet reflection could be controlled with different coatings, the facet phases due to the random cleaving positions relative to the grating phase as mentioned above will still cause uncertainty that affects the yield of single-longitudinal mode operation. For index-coupled DFBs, the best solution to break the DFB mode degeneracy is to introduce a quarter Bragg wavelength shift or $\pi/2$ phase shift segment in grating usually at the center of the laser cavity, which then latches the lasing wavelength exactly at the Bragg wavelength. Unfortunately, this method meanwhile brings some side effects such as uneven intra-cavity longitudinal electric field intensity called spatial hole burning (SHB) especially at high pump level that degrades laser performance [9, 13–19]. To solve the SHB issue, more phase shifts of different values at different locations [20–22] in the cavity were introduced to achieve a relative even cavity longitudinal field intensity distribution but these also makes the design and fabrication of DFB laser devices more complicated. When these shifts are patterned with e-beam lithography, it will unavoidably increase the cost of fabrication meanwhile lower the production throughput. Or if the phase shifts are fabricated using optical lithography with masks, then it might be technically challenging for the first or low order of grating period which usually is of few hundred nanometers given by $\lambda/2n_{mode}$. Where λ is the lasing wavelength in vacuum and n_{mode} is the effective group refractive index of the lasing mode.

In contrast to index-coupled DFB lasers, gain and complex coupled DFB lasers which have periodic structures patterned in the active region or gain medium of the cavity do not have DFB mode degeneracy issue that the emission is exactly at the Bragg wavelength. But as mentioned above, a periodic gain medium requires post-growth after periodic structure was patterned in it, which needs delicate process controls including lowering surface defects density before regrowth and as such involves more complicated fabrication procedures. SBH issues also need to be considered in the design of the gain/complex-coupled DFBs [23].

Most DFB lasers are either fiber lasers or semiconductor lasers. In this chapter and dissertation, we will only concentrate on semiconductor DFB lasers. Semiconductor DFB lasers often times are built with an integrated grating structure, e.g. a corrugated waveguide. The grating structure may be fabricated in or on top of the active region in the cladding or in an laterally coupled structure, where the gratings locate laterally on both sides of the active region for greater index modulation because of closer distance between grating and active region. Other than fulfilling the function of single longitudinal mode operation and wavelength selection, grating in DFB lasers also contributes to narrow spectral linewidth of devices. The linewidth is typically a few hundred MHz or even in the KHz range with special designs, feedback techniques or stabilization techniques involved. All these special features of DFB laser make it ideal for applications such as WDMA in fiber-communication, spectroscopy and any experiments require a very stable and high spectral resolution.

In this chapter, recent research work exploring different active region types for Mid-IR, particularly in the range of 3 to 5 μm as well as different forms of DFB lasers based on these active regions will be first introduced. Then different wide wavelength tuning methods will be presented for comparison with our approach presented in the Chapter 2, although some of them are not directly DFB-related technique and originally developed mainly for fiber-communication systems.

1.2 Mid-Infrared DFB Semiconductor Lasers

DFB lasers operate at different wavelength ranges determined by their gain material spectra. Considering that the main goal or motivation of our tunable DFB laser project is to develop light source for gas remote sensing and spectroscopy in Mid-IR range, we mainly focus on the semiconductor lasers with active region or gain medium epi-structures designed for wavelength range of first atmospheric transmis-

sion window, 3 to 5 μm range as mentioned in the previous section.

In this section, an overview of the four major types of semiconductor lasers in this Mid-IR wavelength range classified mainly according their active region gain media and the energy band alignment structures, namely type-I diode laser (DL), quantum cascade laser (QCL), interband quantum cascade laser (ICL) as well as type-II optically pumped semiconductor laser (OPSL) is presented. QCL and ICL are electrically pumped and also require bias voltage applied to align energy levels in neighboring quantum wells or different active regions in the gain medium for electron tunneling enhancement as shown in Fig. 1.1. DL could be optically pumped but mainly electrically pumped for convenience. Unique possibilities of these four types of lasers as well as their limiting factors are discussed. Based on these four different active region types, several designs or approaches of DFB structures to achieve single-longitudinal mode laser operation will also be presented.

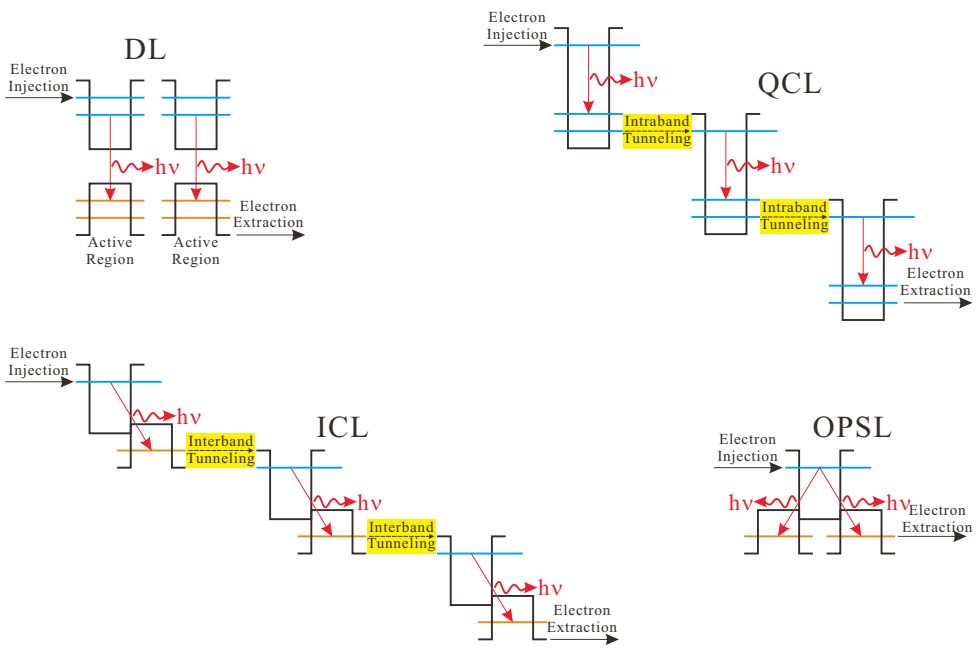

Figure 1.1: Schematic sketch of energy band diagram and the radiative recombination processes in the active regions of DLs, QCLs, ICLs, OPSLs

It is well known that one of the major applications of Mid-IR laser devices is their use in gas-sensing equipments whose underlying measurement principle is tunable laser absorption spectroscopy (TLAS) [24, 25]. Basically in TLAS, tunable laser sources are scanned over the rotational-vibrational absorption spectral lines of target gas molecules to acquire information about composition and concentration. Although this spectroscopic measurement could also be carried out with a wide or finite spectral bandwidth light sources such as nonlinear optics based optical parametric oscillator (OPO), continuous-wave (CW) single-mode with narrow spectral linewidth and tunable light sources are preferred. Usually, these type of light sources are fabricated into the form of DFB or DBR devices with wavelength tunability and they become prerequisite for gas mixtures analysis with high selectivity and sensitivity in the part per billion (ppb) range.

1.2.1 Different Active Region Types of Mid-IR Semiconductor Lasers

1.2.1.1 Type-I Diode Lasers (DLs)

Type-I diode laser is based on double heterostructure pioneered by work from Alferov and Kroemer [26–32], but developed and optimized with quantum wells (QW), quantum wires (QWire) or quantum dots (QD) inserted into the potential well of the double heterostructure to introduce quantum effects and provide higher carrier density at particular energy levels. Although QD DLs have been demonstrated in lab decades ago, QW lasers remain the mainstream type of commercialized semiconductor lasers at present.

Distinct from QCL and ICL structure described below, all QW DLs are pumped in a parallel manner. Talking about electrically pumped DLs, the bias voltage only

needs to be slightly higher than the theoretical limits given by the actual lasing wavelengths. This renders DLs extremely efficient in converting electric power to optical power [33], which is crucial for portable spectroscopic apparatuses driven by batteries. However, limited by the type-I energy band configuration, this type of DLs can't emit photons with energy lower than the QW material's band gap. Till early 1990s, the emission wavelength demonstrated with type-I Sb-based DLs was at $\sim$2 μm [34–39] then later got pushed into longer wavelength by continuously adding indium to the $Ga_xIn_{1-x}As_ySb_{1-y}$ [40, 41]. For this material system, the barrier for carrier confinement is $Al_xGa_{1-x}As_ySb_{1-y}$ with aluminum content up to 50%. Cladding of laser waveguide structure is made of exactly same composition but different content ratio. With this material system, DL devices have reached up to and slight beyond 3 μm [42], which might be close the limit to this design because as indium content in the QW increases for longer lasing wavelength, the band offset relative to carrier barrier layers decreases so that hole confinement is eventually completely lost. The only possible solution to this issue at the moment is switching to quinternary $Al_xGa_yIn_{1-x-y}As_zSb_{1-z}$ barrier materials which can still offer enough confinement for both electrons and holes [43]. Obviously, epitaxial growth with such many-component alloy is very challenging for energy band engineering, lattice constant matching and reasonable yield. 3.4 to 3.6 μm emission at room temperature (RT) by type-I DLs based on quinternary material system have been reported lately [43–46]. Another limiting factor for type-I DLs in the Mid-IR range is Auger recombination which has a coefficient that increases by one order higher as the emission wavelength goes from 2 to 3 μm [47–49].

1.2.1.2 Quantum Cascade Lasers (QCLs)

To access light emission below the host band gap energy, radiative transitions need to happen either between the sub-bands in conduction/valence band or between effective

energy bands in a type-II QW or super lattices (SL) epi-structures (Type-II QW are utilized by ICLs and OPSLs to be introduced next.). QCLs are representative of light source devices based on intra-band transitions [50, 51]. Usually, QCLs exploit these intra-band transitions in the conduction band due to the fact that electrons have lower effective mass and less complex band gap engineering requirements than holes. As mentioned earlier, all QCLs are electrically pumped and require proper bias voltage to align different transition energy levels in the cascading active regions so that electron tunneling happens conveniently, as shown in the Fig. 1.1. Because of this mechanism, one carrier passes several active cascades while traveling through the whole QCL epitaxial structure and generates more than one photon resulting in a quantum efficiency greater than 1 [52].

The most obvious advantage of QCLs compared with other types of semiconductor lasers is their outstanding performance in long wavelength emission at room temperature or even higher. Given a properly designed active region, CW emission wavelength beyond 10 μm at RT can be achieved [53]. In pulsed operation mode, wavelength over 100 μm can be reached at lower temperatures [54]. But on the shorter wavelength side, QCLs' performance degrades rapidly in the range from 3 to 4 μm, due to an insufficient conduction band offset for effective electron confinement. By finding the right composition of different material systems and right composition ratio to offer higher band offset for electron confinement, emission wavelength of QCLs has been extended significantly to shorter wavelength side. Using InAs(Sb)/Al(As)Sb structures on InAs, so far the highest energy QCL emission has been achieved at 2.6 μm at cryogenic temperatures [55]. Generally, it's difficult for QCLs to emit shorter than 3 μm at cryogenic temperature even in pulse mode. Reaching RT operation is very difficult [56–58]. The reason is believed to be the pronounced Γ-L valley scattering at short wavelengths, and a satisfactory solution has not emerged as yet. Nonetheless, QCLs at ∼3.3 μm areo still a very good candidate for detection of hydrocarbon stretches. For example, InP-based QCLs deliver

appealing performance in the range of 3.3–3.5 μm although not quite good enough for spectroscopic applications [59]. So far, CW operation of QCLs at RT is limited to wavelength above 3.8 μm, whereas it could be extended to shorter wavelength as progresses are made [60]. Due to extremely fast phonon mediated relaxation processes on the order of 1 ps, QCLs have to be pumped with fairly high current until the threshold is reached, while showing comparably low external efficiencies per active stage [61]. In conjunction with the high bias voltage required for mini-band alignment in tens of cascades, this leads to relatively high power consumption and needs extra effort for thermal management, which also lowers the overall efficiency of the QCL devices [62, 63].

1.2.1.3 Interband Cascade Lasers (ICLs)

Common to both ICLs and OPSLs as shown in the Fig. 1.1, the approach to tailor the emission wavelength almost independently of bandgap energy or band offsets can be acquired using spatially indirect type-II transitions between neighboring different material layers offering electrons and holes respectively, e.g. InAs and $Ga_xIn_{1-x}Sb$ sandwiched between AlSb barrier layers which offer efficient carrier confinements. Different from DLs and QCLs which have been demonstrated in all common III-V materials systems including (AlGaIn)(As), (AlGaIn)(AsP) or (AlGaIn)(AsSb) on suitable substrate, ICLs and OPSLs utilize the broken gap alignment of InAs/Ga(In)Sb/AlSb layering sequences so that they are accordingly limited to this type-II material system. Due to the fact that electrons and holes are located in different layers, the transition probability characterized by the spatial overlap of electron and hole wave function overlap is lower as compared with type-I QW transitions. But with so called W-shaped QW configuration (as shown in Fig. 2.1) consisting of one layer of InGaSb offering holes sandwiched by two layers of InAs providing electrons, the e-h recombination probability can be still up to $\sim$70% of

the value of a type-I QW which means this type of QW configuration offers sufficient gain for lasing. Also, type-II QW's effectively suppress Auger processes which deplete carriers from radiative recombination particularly due to the high energetic separation of the split-off band. In addition, the small in-plane effective hole mass accompanied by a reduced density of states helps decrease threshold carrier density needed to reach population inversion [64]. Combining this type of QW structure with the concept of cascade designs led to the appearance of ICL devices as shown in the Fig. 1.1. ICLs are relative newer in terms of theoretical development [65] and experimental realization [66], but device performance is steadily increasing such that CW operation above RT at 3.75 μm was reported in 2008 [67]. For the wavelength range from 3 to 4 μm, it is very impressive for ICLs to tune the emission wavelength by only changing the W-shaped active region dimensions with the remainder of the device design remaining the same [68]. Multiple and single mode ICLs with this approach have been reported to achieve CW operation at RT in this range in recent years [69, 70]. Compared with DLs and QCLs, ICL outperforms both particularly in the wavelength range from 3.3 to 3.7 μm [71].

1.2.1.4 Optically Pumped Semiconductor Lasers (OPSLs)

Different from the aforementioned three types of lasers, this type of laser is optically pumped instead of being electrically pumped as its name indicates. OPSL's active region is actually very similar to that of ICL as shown in the Fig. 1.1. Since no cascadable design is intended, the epitaxial growth of the active region is fairly simple compared with QCL and ICL. It also does not require a bias voltage to be applied for cascading processes and can be made convenient for optical pump for some special device design as our tunable DFB laser device to be introduced in Chapter 2. More information about Mid-IR OPSL could be found in the book, *Mid-infrared Semiconductor Optoelectronics*, edited by A. Krier [72]. And the detailed

introduction to this type of semiconductor laser gain medium will be presented in Chapter 2, together with our unique method of wavelength tuning.

1.2.2 Different Grating Patterning Approaches to DFB Mid-IR Semiconductor Lasers

As mentioned in the beginning of this section, an essential requirement especially for applications such as spectroscopy and gas sensing is single longitudinal mode (SLM) operation, with a narrow spectral linewidth. Although quite some different technical approaches could be applied to achieve single-mode operation in lasers, we will focus on DFB lasers based on the aforementioned active region types in this sub-section.

There are generally three major different approaches to fabricated DFB lasers based on the four types of active regions discussed above. These three approaches are all optimized for electrically pumped DFB semiconductor lasers taking the form of ridge waveguide. The first approach is to use a metal such as a chromium grating patterned on both sides of the ridge waveguide with an embedded gain medium fabricated previously [73]. The metal grating interacts with the evanescent part of the guided optical modes thus introduces extra loss to all modes except the lasing one. This approach works well for DLs but is very difficult to apply on QCLs and ICLs mainly because the grating or periodic corrugation can't be patterned close enough to the active region so that its interaction with optical mode is too weak. The second approach is to etch a grating that extends over the side walls of the laser ridge, which provides modulation of the effective refractive index (both real and imaginary parts) to select the lasing wavelength [74, 75]. This approach has been applied on QCLs successfully in recent years. For QCL or ICL, the deep etch to form the high aspect ratio gratings needs to go through active region layers, so refractive index modulation from grating is much stronger than the first approach.

But the quality of the deep etch needs to be carefully controlled especially when the grating period is small for relatively short lasing wavelengths. The final approach is to etch a grating on the top of laser ridge usually formed by wet etch that its cross-section takes trapezoid-like shape. For electrically pumped lasers, contacts are then deposited on the whole surface of the ridge including the sloped side walls atop the grating so that the grating located between the contact and optical modes modulates both the refractive index and gain at the same time to select a single wavelength in operation [76, 77]. Top grating approach is conventional, convenient and has been applied on all different types of semiconductor lasers. To have enough perturbation or modulation of refractive index in DFB devices, the top clad thickness of the laser waveguide epitaxial structure usually needs to relatively thin or the clad refractive index needs to be well controlled for interaction between grating and optical modes. We adopted this top grating approach for refractive index modulation on our tunable DFB laser device. But due to the optical pump design, a ridge waveguide structure can not be used, as shown in Chapter 2.

1.3 Widely Tunable Semiconductor Laser

Generally speaking, many different technologies for wavelength tuning have been demonstrated on different types of lasers. For example, an intra-cavity birefringent crystal could be rotated to achieve over 200 nm tuning range for a solid state laser. In this section, introduction to wavelength tuning techniques is limited to those that have been applied to semiconductor lasers. There are quite some different wavelength tuning approaches implemented by different research groups, such as thermal/temperature tuning, external cavity, MEMS/VCSEL, grating coupled sampled-reflector (GCSR), sampled-grating DBR (SGDBR) [78–80], super-structure gratings (SSG) DFB [81–84], and selectable DFB array [85–89]. All these technical

approaches have been applied on semiconductor lasers for different purposes or applications, with different wavelength ranges. Some of them involve the use of gratings in the laser structure, some do not necessarily have grating as shown in this section.

1.3.1 Temperature Tuning

Temperature or thermal tuning as its name indicates is to tune the laser output wavelength by varying the operation temperature of the device. It mainly utilizes the effect that band gap energy changes as temperature varies, although refractive index, thermal expansion also get involved slightly as operating temperature changes. Temperature tuning is usually not practical for wide wavelength tuning applications because of the detuning of gain spectral peak with respect to the wavelength selection mechanism of the laser cavity. Also the output power normally varies significantly when temperature variation is too large. But still when it was applied on QC-DFB lasers which have a huge operating temperature range, this approach generated single mode tuning range of 150 nm as laser heat sink temperature increased from 10 K to 300 K [90]. Additionally, the selectable DFB array approach to be presented later in this section for wide wavelength tuning uses temperature tuning on each individual DFB laser device in the array for about 3 to 4 nm tuning range. Temperature wavelength tuning is continuous, but it has to be conducted at fairly slow speed on the order of milli-second to allow thermal equilibrium to be achieved.

1.3.2 MEMS/VCSEL Tunable Lasers

This technical approach to wavelength tuning is more or less limited to vertical cavity surface emitting lasers (VCSEL) through varying cavity length. Single mode lasing can be easily achieved with this type of laser, benefiting from its large free spectral range (FSR) due to the ultra-short cavity length. In its implementation,

the top distributed reflector in single wavelength VCSEL is replaced with a mirror mounted on cantilever or piezo actuator fabricated with micro-electro-mechanical systems (MEMS) technique which raises or lowers under control that equivalently changes the cavity length thus tunes the laser wavelength [91–95]. This wavelength tuning approach can usually achieve tuning range of tens of nanometers, and the latest tuning range from F. Taleb *et al.* reached 117 nm [96]. As mentioned in the beginning, this technology can hardly be integrated or applied onto the DBR or DFB lasers which usually are fabricated in the form of edge emitters.

1.3.3 External Cavity Tunable Laser

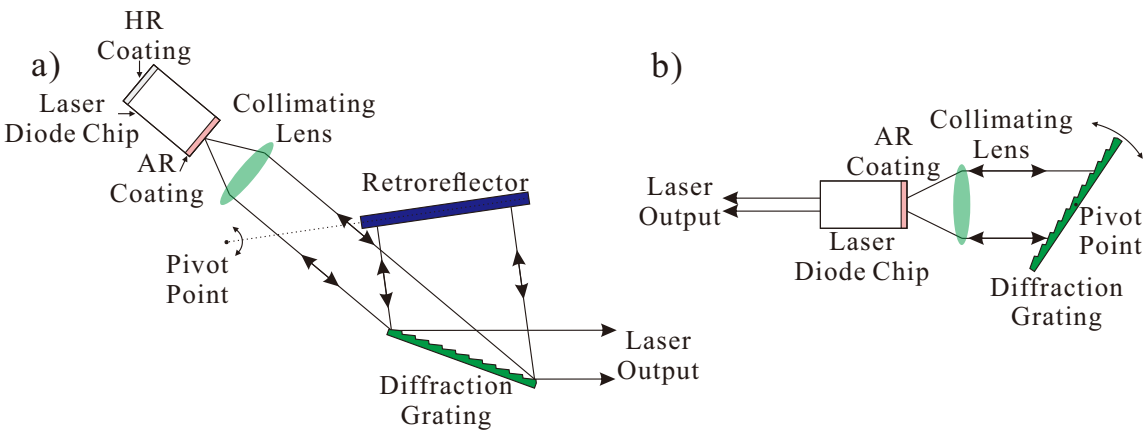

Figure 1.2: Schematic for external-cavity tunable laser

External-cavity tunable lasers take cavity arrangements as illustrated in Fig.1.2, in which a) is so-called Littman-Metcalf Cavity and b) is Littrow configuration. This type of laser generally consists of a linear cavity with a semiconductor gain medium and an external cavity diffraction grating and a mirror or combination of two as shown in b) aligned in above configurations that rotates at different angles to select different lasing wavelengths [97–105]. Although the highly dispersive diffraction grating functions well to select single wavelength to lase, the laser cavity is still con-

ventional F-P cavity which means the lasing longitudinal mode hops from one F-P mode to the next. Of course, the mode spacing or the free spectral range (FSR) is small because of large cavity length. To correct this, Intel has reported to use two independently temperature-tuned etalons to increase mode spacing to achieve truely continuous wavelength tuning. Most of the scientific research tunable lasers with this technology do not have these extra optical parts in the cavity but still achieve quasi-continuous wavelength tuning. The main drawbacks of this type of laser are manufacturability and reliability issues given the need for assembling numerous micro parts and holding them in precise alignment. In addition, high quality anti-reflection coatings are required to cover wide wavelength ranges. This wavelength tuning technique can be combined with different gain media to achieve tens of nanometers tuning range easily. To the knowledge of author, an external cavity QCL reported by A. Hugi achieved wavelength record of about 3.8 μm of tuning range [105].

1.3.4 Super-Structured Grating or Grating-Coupled DBR Tunable Lasers

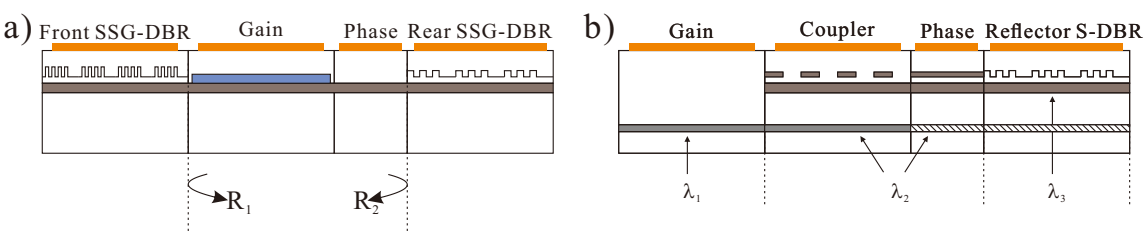

Figure 1.3: a) Super-Structured-Grating-DBR (SSGDBR) and b) Grating-Coupled Sampled-Reflector (GCSR) Tunable Lasers

These two types of semiconductor lasers as shown in Fig. 1.3 are presented together because they both use super-structured gratings or sampled gratings while the particular wavelength tuning mechanism of the two is not exactly the same.

Both types of laser were originally developed for wavelength division multiplexing (WDM) in fiber-communication systems, but there is no reason they can not be applied on Mid-IR lasers. Sampled grating DBR (SGDBR) is actually a special case of super-structured grating DBR lasers (SSGDBR). Super-structured gratings are usually designed as phase modulation of the constant period gratings and could take the form of periodic bursts of a chirped grating [106]. In comparison, sampled-gratings are normally amplitude modulation of grating, as shown in the Fig. 1.3 which is a constant-period grating modulated by a periodic square wave function with larger period. SSGs typically require e-beam lithography for fabrication, but SGs can be easily patterned by combination of holographic and photo-lithography or photo-lithography alone if grating period is sufficiently large. For both types of modulated gratings, the desired reflection spectrum of the whole grating as function of wavelength or frequency is a multiple-peaked comb for wavelength tuning purposes.

SGDBR as a simplified SSGDBR case shown in the Fig. 1.3 a) typically consists of four sections: gain, phase, front mirror, and back mirror. In the front and rear mirror sections, periodically sampled DBR gratings are patterned to form a comb-like reflectivity spectrum as mentioned above. The sampling periods (corresponding to the spacing between the comb-teeth in reflectivity spectrum) in these two sections differ and reflectivity peak positions of the two gratings can be tuned independently with injection current or bias voltage variation, so that only one of mirror reflectivity peaks from each of the two section overlaps or coincides to select the lasing wavelength in tuning range. In the process of wavelength tuning, adjacent reflectivity peaks can be aligned by differentially tuning the front and back mirrors, then the laser will operate at this new wavelength. Another way of understanding this tuning mechanism is that the laser is tuned by the beating effect between the two different mirror reflection combs, namely the Vernier effect. Mathematically, if the reflectivity from the front and back mirrors are R_1 and R_2 respectively, the lasing wavelength is determined by R_1R_2. If injection current is used to tune the reflectivity comb of

these two mirrors, then the laser output wavelength is function of $R_1(I_1)R_2(I_2)$. In this case, the total wavelength tuning capability of the device is the product of $\Delta n/n$ and $\delta\lambda/\Delta\lambda$, where $\Delta n/n$ is the single grating tuning capability and $\delta\lambda/\Delta\lambda$ is the difference in spacing between the mirror reflection peaks of the two mirrors divided by mean mirror peak spacing. This design can accomplish discontinuous tuning range from 50 to 100nm and quasi-continuous tuning range of about 20nm [81]. Due to the grating losses from current injection for tuning, the differential efficiency and chip output power are limited. But the good feature of this type of laser is that it is very convenient to integrate semiconductor optical amplifier (SOA) or other optical modules with the laser [107]. It is ideal for monolithic design and optical integrated circuits.

GCSR tunable lasers appeared later than SGDBR and actually incorporate a grating-assisted co-directional coupler (GACC) with a SGDBR. GCSR tunable laser is accomplished by using the property of GACC or vertical-coupler filter as shown in the coupler section of the Fig. 1.3 b). The enhanced tuning of this type of device derives from the refractive index tuning relative to the difference in modal refractive indices between the two coupled waveguides as illustrated in the coupler section of GCSR in the Fig. 1.3, $\Delta n/(n_1\text{-}n_2)$ rather than $\Delta n/n_1$ as in most other tunable filters [108]. Because the filter is broad band, a back multiple-order sampled-grating reflector is required for good mode selectivity to achieve single mode lasing. GCSR structure is fairly complex with two vertical waveguides, three different bandgap regions, three changes in lateral structure and two different gratings and is very difficult to fabricate compared with a SGDBR. Nonetheless, significant efforts have led to relatively good performance such as 40 nm continuous or 114 nm discontinuous wavelength tuning range with SMSR of >30 dB have been achieved by different research groups [108–111].

Practically, the above two types of tunable lasers achieve wavelength tuning

through differential variation of current injection in different mirrors or filter sections which turns out be very complicated requiring current injection look-up tables or microelectronic circuits for operation. All these could bring in some potential operation reliability issues.

1.3.5 Selectable DFB Array Tunable Laser

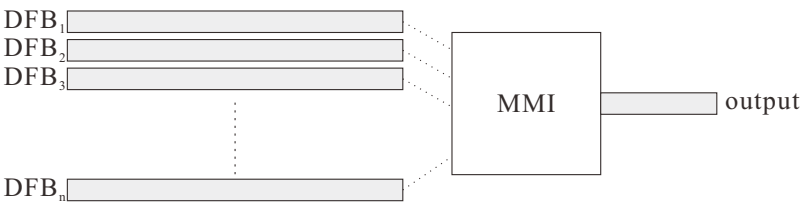

Figure 1.4: Schematic of selectable DFB array tunable lasers

Selectable DFB array as illustrated in the Fig. 1.4, consists of a array of N different single longitudinal mode DFB lasers that operate at a series of closely spaced but discrete wavelengths. Different single DFB lasers can be selected and coupled through multi-mode interface (MMI) or MEMS mirror to output for expected wavelength. The wavelengths in between these different wavelengths can be acquired by temperature-tuning on individual DFB laser, usually in range of 3 to 4 nm with temperature variation of 30–40 °C. So the total wavelength tuning range of the DFB laser array is $4N$ nm. This approach has been applied to different types of semiconductors from fiber-communication to far infrared wavelength ranges for wavelength tuning purposes [88,112–114]. The whole array of DFB lasers is fabricated monolithically on a single die. It is a relatively easier implementation of tunable laser compared with SSGDBR or SGDBR approaches, but still unavoidably involves fairly complicated design, structure, processing and temperature control mechanisms. Usually custom-designed controller or electronic circuit is required to power each single DFB device in the array and DC current bias circuitry is also used to control the operation tem-

perature for wavelength tuning. In addition, some controlling interface for computer is required for the control of laser firing. Often times, the array consists of tens of single DFB laser devices which makes the fabrication processes difficult and yield low to guarantee all of them work properly. Unexpected variation in performance of different single device are always observed due to the above reasons. Other than that, some tapered waveguide or other low loss beam combining schemes need to be developed to couple out the whole array of laser into a single output and special attention needs to be paid for temperature control and heat dissipation. Through this approach and combined with QCL, about 700 nm of single longitudinal mode continuous tuning has been demonstrated [88].

1.4 Projection Motivation

The motivation of our research project presented in this dissertation, as mentioned earlier, is to develop a tunable DFB laser device based on type-II quantum wells (QW) gain medium in the Mid-IR range, especially in the range of 3 to 5 μm within one of the atmospheric transmission windows that is ideal for for gas remote sensing and spectroscopy applications. In this range, there are quite some signature absorption spectral lines for identifying molecular vibrations of bonds between different atoms, for example, N-H stretch at $\sim$3 μm, C-H stretch at $\sim$3.3 μm. The target features and performance characteristics of our tunable DFB laser device are listed as following,

1. Continuous-wave (CW) operation,

2. Single longitudinal mode operation and mode-hopping free,

3. Narrow spectral linewith on the order of 1 nm,

4. Wide wavelength tunable range of about 100 nm, suitable for atmospheric pressure broadened molecular spectroscopy,

5. High output power up to the order of 1 Watt.

1.5 Outline of the Dissertation

The dissertation is presented in five chapters, including Chapter 1 for general introduction to DFB lasers. In this chapter, four different types of active region and epitaxial structures of gain media in the Mid-IR wavelength range from 3 to 5 μm, and several technical approaches to implement SLM operation and wavelength tuning were presented.

Chapter 2 covers the design and fabrication of our optically pumped tunable DFB laser device. Specifically, it includes slab waveguide mode solver for effective refractive indices, confinement factor, coupling strength calculation and chirped grating period calculation as well, followed by fabrication.

Chapter 3 presents the experimental results of the tunable DFB laser device characterization, including threshold, single facet output power, spectral linewidth and tuning range.

Chapter 4 presents some preliminary simulation results based on transfer matrix method (TMM) for determining laser emission wavelength and also proof of continuous wavelength tuning.

Chapter 5 summarizes the research work of this project at the moment and also proposes the future work .

Chapter 2

Device Design and Fabrication

2.1 Our Approach to Tunable DFB Lasers

Different from other methods introduced in Chapter 1 to implement wavelength tuning, our approach is to fabricate an index-coupled DFB laser with location-dependent hyperbolically chirped grating etched in the top clad layer of the device to select the lasing wavelength. The tuning mechanism can be explained as such that as the optical pump stripe is translated relative to the device to different lateral positions, different grating periods at the excited locations select different lasing wavelengths. In contrast to other electrically pumped laser designs with effective ridge structure for lateral mode confinement, our laser does not have ridge structure. The optical pump stripe laterally defines the so-called activated region within where the DFB laser device lases, which makes it a laterally gain-guided device. In summary, this type of tunable DFB laser device is analogous to the previously introduced selectable DFB array in the sense of offset grating periods at different locations(ridges), but with infinitesimal small continuous grating period offset and needs to be pumped optically.

The method for wavelength tuning of our DFB laser is very straightforward, while the fabrication of this chirped grating can be a challenge. Interferometric lithography (IL) technology was chosen to pattern the chirped grating, thanks to its obvious advantages in patterning periodic structures such as gratings over large area with adequate flexibility of varying period, simple experimental setup and high throughput. Normal IL with collimated incident beams produces only straight gratings which do not fulfill the function required for our approach to achieve wavelength tuning. For that reason, interference between two spherical waves is utilized to form the chirped gating to be presented in this chapter. The idea is not brand new [115–118], but to the knowledge of author, no other research groups have used chirped gratings for wavelength tuning purposes.

In this chapter, design and fabrication, including the calculation of the grating period and the IL experiment setup for chirped grating patterning of the tunable DFB laser will be presented systematically.

2.2 Introduction to Gain Medium–Type-II Quantum Well

GaSb based type-II quantum wells (QW) have been widely used for Mid-IR optically pumped semiconductor lasers (MIR-OPSL), which was first proposed by J. Meyer *et al*. [119] and demonstrated by researchers at MIT the Lincoln Laboratory [120]. A generic design of the type-II QW gain medium for optically pumped device is shown in Fig. 2.1 a). The InGaSb layer, functioning as hole well is surrounded by two coupled InAs electron wells. Two layers of integrated absorbing layer (IA) are grown on either side of this InGaSb and InAs sandwich structure, to generate carriers after absorbing the excitation light and inject them into the InAs and InGaSb wells. In

this QW structure, electrons can be confined very well. But the composition of the IA that leads to the energy band offset, as well as the thickness of InGaSb are critical for efficient hole injection and confinement. In addition, the composition of IA also has effect on the total effective refractive index since it constitutes a substantial portion of the core layer of slab waveguide structure in OPSL shown in the Fig. 2.1 b). The beauty of this material system and epi-structure is that by varying only the thickness of the InAs layers, the gain spectrum can be tuned to cover very wide range from Mid-IR to long-wave IR, from ∼2 to ∼10 μm [72, 121] without significantly altering the electron and hole wave functions overlap so that there is no accompanying loss of gain. But the drawback of this structure is that it loses hole confinement as temperature increases to about 150K, so lasers with this type of gain medium only operate in CW mode at around liquid nitrogen (LN_2) temperature [122]. The energy band alignment of these total 5 layers of different materials forms a "W" shape, which is also the reason this type of quantum well is commonly called W-QW.

The optically pumped tunable DFB laser presented in this dissertation is based on the above introduced gain medium and epi-structure but with integrated absorber optimized for a 1.9 μm pump source meanwhile offering a low confinement slab waveguide design with better output beam quality and reduced filamentation [123–127]. As shown in the Fig. 2.1 a), it consists of a 8 mono-layer thick center layer of $In_{.4}Ga_{.6}Sb$ sandwiched by two layers of InAs of about 4 mono-layer thick. Two layers of ∼100 nm thick integrated absorber (IA) composed of $In_{.2}Ga_{.8}As_{.18}Sb_{.82}$ are grown next to the InAs layers with optimized band gap, band-alignment and thickness to efficiently absorb the pump power and inject excited carriers into the type-II QW, offering carrier confinement as well.

A wafer with the above epi-structure, V9-18, was grown with molecular beam epitaxy (MBE) by Dr. Ron Kaspi at Air Force Research Laboratory (AFRL). The cross-section view of the wafer is shown in Fig. 2.1 b). Basically, it is a slab waveguide

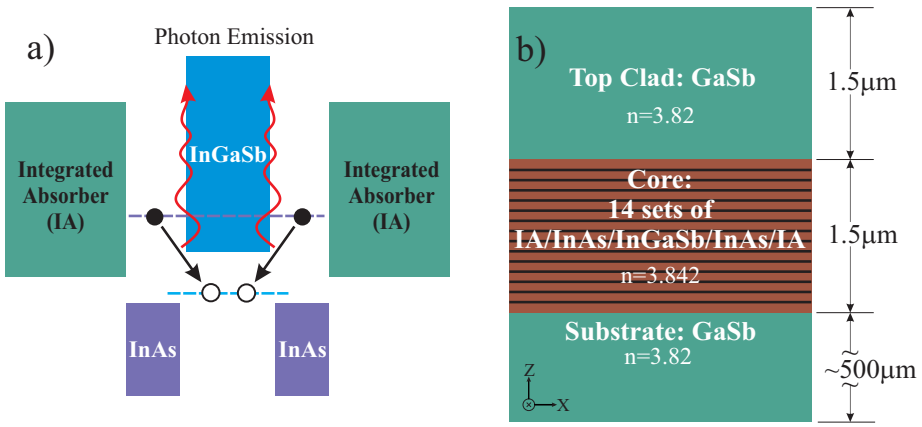

Figure 2.1: Epi-structure of the wafer with type-II QW gain medium

structure consisting of 3 major layers. Grown on a GaSb:Te substrate also functioning as a bottom cladding layer, the core layer of the slab waveguide in red is 1.5 μm thick and contains 14 sets of W-shaped type-II QWs as shown in part a) of the figure, corresponding to the black lines in core layer shown in part b). 1.5 μm core thickness is determined for all IAs to both fully absorb the pump power and to function as a single transverse mode slab waveguide at the same time. The equivalent refractive index of core layer is about 3.842 as labeled. A 1.5 μm of GaSb layer is grown atop of the core layer as top clad, in which the chirped grating will be patterned. GaSb layers have refractive index of about 3.82. So the difference of the refractive indices between core and clads is 0.022, a low confinement waveguide design for better output beam quality as mentioned. Wafer V9-18's PL spectral peak measured at 80K by AFRL is centered at 3.06μm, with FWHM of about 100nm.

2.3 Device Design

In the design of our tunable DFB laser, the most important part is the chirped grating for wavelength tuning. Other than that, there are generally three constraints

that need to be taken into account for grating design of DFB lasers, namely

1. Target grating period needs to match the gain medium's gain spectral peak at the operation temperature of ∼80K, to fully utilize the material gain to maximize laser output power;

2. Coupling strength κL_g should be in the range between 1 and 3, enough to offer strong feedback for wavelength selection but not so high as to cause issues such as uneven intra-cavity field intensity or spatial hole burning (SHB);

3. Confinement factor Γ should be higher than 0.3 to have enough modal gain for laser device to easily reach threshold and have high output power.

In addition, there are a few other concerns particularly for our device design that need to be considered such as grating angle and the control of lateral and longitudinal chirp. All of these will be introduced in the following sections.

In the analysis of grating on this index-coupled DFB laser device, including wavelength selection, coupling strength and the confinement factor, effective refractive index approach introduced in the Chapter 3 of *Diode Laser and Photonic Integrated Circuits* by L. A. Coldren, S. W. Corzine and M. L. Mašanović is applied [8]. This approach was developed to unify transfer matrix method (TMM) in analysis of both DBR and DFB structures. When it is applied for DFB devices, the only difference from when being applied on DBR structures, is that all of the refractive indices of different layers in DBR are replaced with the effective refractive indices solved in the slab waveguide analysis with a top clad thickness corresponding to the distances from either ridge top or groove bottom of the grating to the core layer respectively, namely D_R and D_G labeled as shown in Fig. 2.2. In other words, the ridge and groove segments of the grating correspond to slab waveguides with different top clad thicknesses, and therefore support different transverse electric field modes with different

effective refractive indices as labeled in the figure. Then, the grating structure is equivalent to layer stack with different effective refractive indices as shown in Chapter 4 of this dissertation. Once the effective refractive indices are solved, the grating in the DFB laser is treated exactly the same as layers in DBR structure.

Grating cross section profile in DFB laser does not have to be square as shown in Fig. 2.2. But a square grating is our choice since it happens to be the most convenient profile to fabricate and offers the highest coupling coefficient. The geometry and dimensional information about grating are labeled in the figure. Ridge and groove width are W_R and W_G. Top clad thickness at the ridge and groove segments of grating are D_R and D_G respectively. So depth of grating groove is $D=D_R-D_G$. The different effective refractive indices, n_{Eff-R} and n_{Eff-G}, are calculated with the slab waveguide model to be presented in the next section.

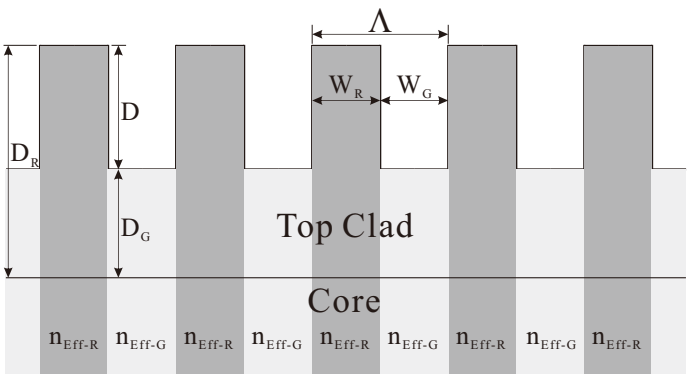

Figure 2.2: Schematic of the cross section profile of in-plane grating, and corresponding effective refractive indices of grating ridge and groove segments

Because all of the above mentioned three constraints involve the guided mode solution to slab waveguide structure of wafer shown in Fig. 2.1 b), slab waveguide's solution will be introduced first. Due to the reason that the top clad of wafer V9-18 slab waveguide is not thick enough to fully contain the decay of the guided mode completely, a 4 layer slab waveguide model with an extra cover layer atop the clad

layer is included for the mode solution. In this case, the cover layer is air, taken as infinitely thick. Besides, DFB laser with the same QW material system and similar slab waveguide dimensions has been shown by previous group member, Liang Xue to support only in TE modes [128]. Accordingly, only the TE mode solution of the slab waveguide will be presented in the dissertation for brevity.

2.3.1 Solution to Four-Layer Slab Waveguide Structure

The slab waveguide model adopted for calculation of TE mode distribution for the 4-layer slab waveguide is from the paper by Yi-Fan Li *et al*. [129], as a special case of multilayer structure. The side-view geometry of this 4-layer slab waveguide is drawn in Fig 2.3, with coordinate system built as shown. Z direction is the epitaxial growth direction and Y direction is the TE mode polarization direction.

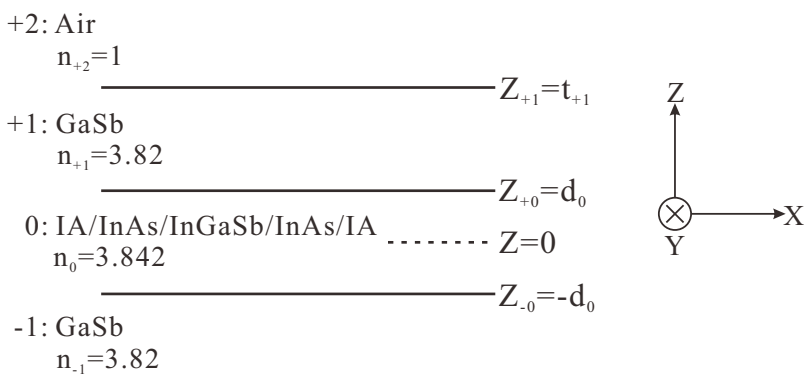

Figure 2.3: Geometry of a 4-layer slab waveguide. d_0 is the half thickness of the core layer.

Only the fundamental TE mode, TE_0 exists in this slab waveguide and the solution of the guided TE_0 mode is given with the following set of equations 2.1, corresponding to the mode profiles in different layers of the waveguide. Subscript integers $+2, +1, 0, -1$ are used as layer indices standing for cover layer, top clad

layer, core layer and substrate layer respectively as labeled in the Fig. 2.3 and the equations. d_0 is the half thickness of the core layer which is 0.75 μm for wafer V9-18. And the top clad thickness $t_{+1} - d_0$ is to be varied to scan across possible ranges of top clad thickness and grating groove depth for different effective refractive indices based on which grating period, coupling coefficient/strength can be calculated. And confinement factor can also be calculated once the guided mode electric field profile given by the following equation set is acquired.

$$E_{Y,+2} = \cos(2k_Z d_0 - \phi_{-0}) \frac{\cosh(p_{+1} d_{+1} - \psi_{+1})}{\cosh \psi_{+1}} EXP[-p_{+2}(Z - Z_{+1})] \quad (2.1a)$$

$$E_{Y,+1} = \cos(2k_Z d_0 - \phi_{-0}) \frac{\cosh[p_{+1}(Z - Z_{+0}) - \psi_{+1}]}{\cosh \psi_{+1}} \quad (2.1b)$$

$$E_{Y,0} = \cos[k_Z(Z - Z_{-0}) - \phi_{-0}] \quad (2.1c)$$

$$E_{Y,-1} = \cos \phi_{-0} EXP[p_{-1}(Z - Z_{-0})] \quad (2.1d)$$

Where propagation constants p_i and k_Z, and phase terms ϕ_i, ψ_i are given in the following equations. k and β are the TE mode propagation constants in vacuum and the slab waveguide. In the calculation, vacuum wavelength is set at 3.06 μm for k to match the PL spectral peak wavelength measured at 80K.

$${k_Z}^2 = k^2 {n_0}^2 - \beta^2 \quad (2.2a)$$

$${p_i}^2 = \beta^2 - k^2 {n_i}^2 \qquad (i = -1, +1, +2) \quad (2.2b)$$

$$\phi_{-0} = tan^{-1}(\frac{p_{-1}}{k_Z}) \quad (2.3a)$$

$$\phi_{+0} = tan^{-1}[\frac{p_{+1}}{k_Z} tanh \psi_{+1}] \quad (2.3b)$$

$$\psi_{+1} = p_{+1}(t_{+1} - d_0) + tanh^{-1}(\frac{p_{+2}}{p_{+1}}) \quad (2.3c)$$

k_Z, which is the Z component of the guided mode propagation constant, is graphically solved from the waveguide eigenvalue equation 2.4, with top clad thickness

of 1.5 μm as an example shown in Fig. 2.4. q in the equation 2.4 as shown is a non-negative integer for different order guided modes if they exist.

$$2k_Z d_0 = \phi_{+0} + \phi_{-0} + q\pi \qquad (q = 0, 1, 2, ...) \tag{2.4}$$

Effective refractive index n_{Eff} is calculated by the following equation.

$$n_{Eff} = \frac{\beta}{k} \tag{2.5}$$

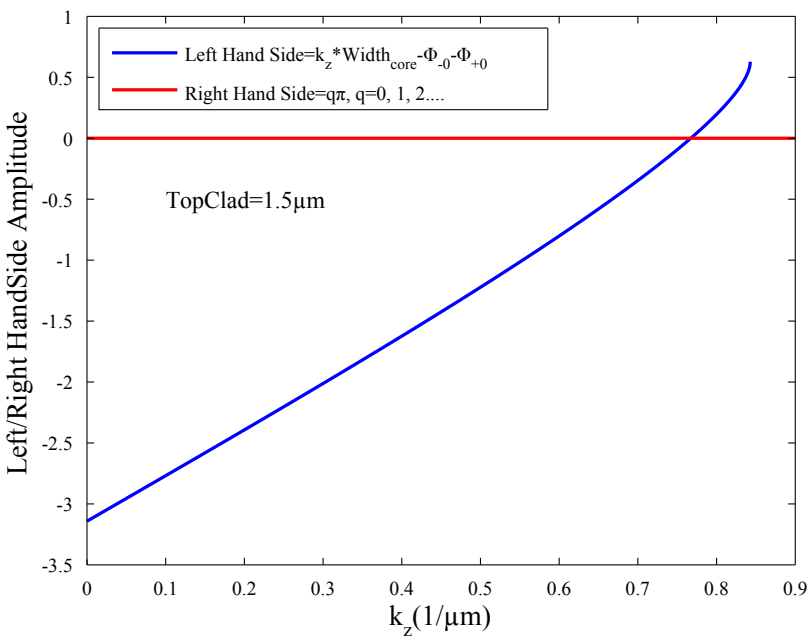

Figure 2.4: Graphic solution of 4-layer slab waveguide eigen function

As examples of slab waveguide solution, the field distributions of the fundamental TE mode, TE_0 are plotted in Fig. 2.5, for three different thicknesses of the top clad GaSb layer 0.5 μm, 1.0 μm and 1.5 μm as shown. Obviously, different top clad thicknesses significantly affect the guided mode electric field profile. Simply speaking, thicker top clad thickness will pull the mode out from the substrate and make the mode decay faster in the clad layers. Matlab code for the solution of TE_0 mode to this 4-layer slab waveguide can be found in Appendix C.1.

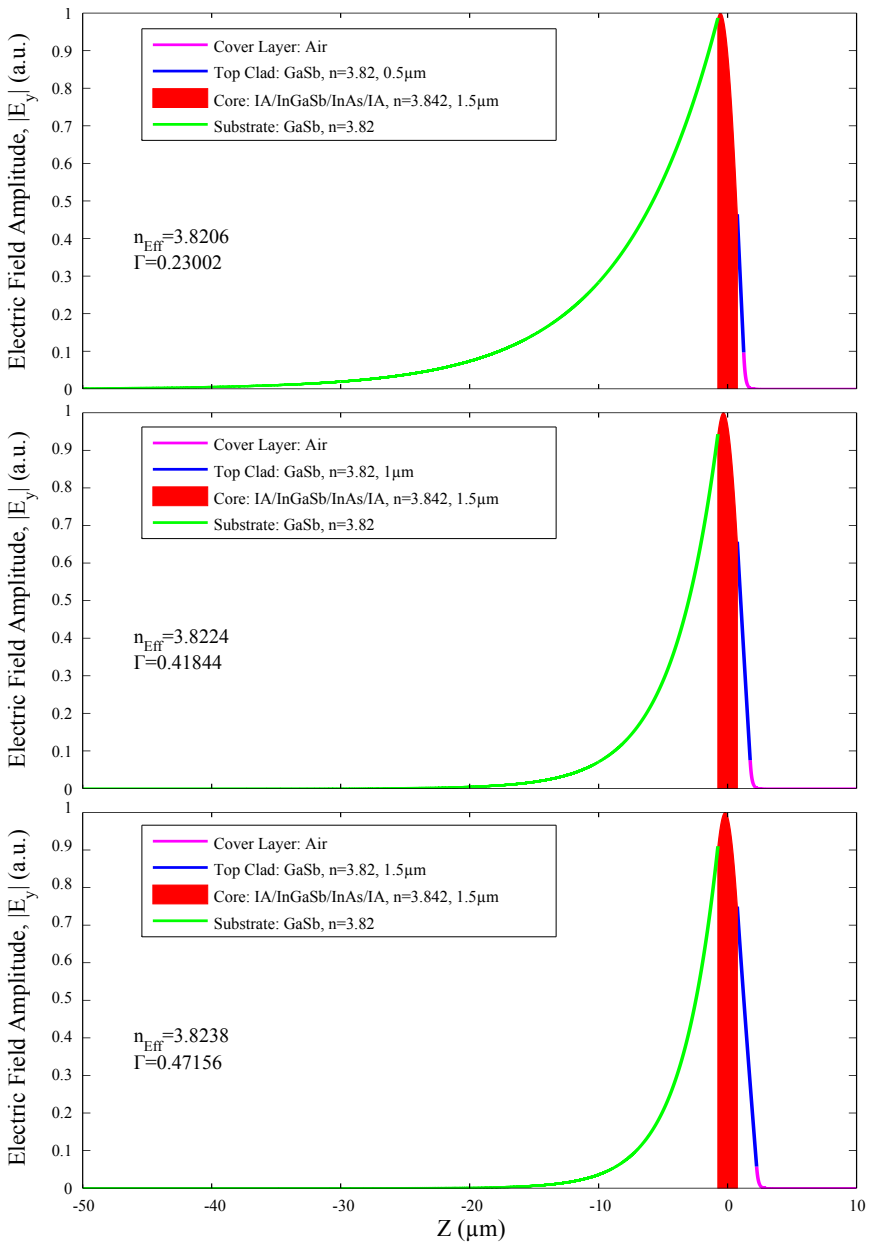

Figure 2.5: Field of TE_0 Mode in slab waveguide with different top clad thicknesses of 0.5 μm, 1.0 μm and 1.5 μm. Mode profile in cover and top clad layers and substrate is plotted in magenta, blue, and green respectively. The red area in the figure corresponds to the mode profile in the core layer. Once converted to intensity, red area relative to the full area under mode profile gives confinement factor, Γ.

2.3.2 Target Bragg Grating Period

For DFB Lasers, the grating used for wavelength selection is often called a Bragg grating. Its period, together with the effective refractive index of laser cavity determine the Bragg wavelength (equal or in the vicinity of lasing wavelength), which should match the gain medium's spectral peak in operation condition as mentioned. The relation between Bragg wavelength, λ_{Bragg} and the grating period, $\Lambda = W_R + W_G$ is given by the following equation.

$$\lambda_{Bragg} = 2(n_{Eff-R}W_R + n_{Eff-G}W_G) = 2\bar{n}_{Eff}\Lambda \tag{2.6}$$

Where n_{Eff-R} and n_{Eff-G} are the effective refractive indices acquired in solving the slab waveguide mode with different top clad thickness of D_R or D_G, corresponding to the ridge or groove segment of the Bragg grating as presented in the previous section. Average effective refractive index, $\bar{n}_{Eff}$ is the average of n_{Eff-R} and n_{Eff-G} when W_R=W_G. In calculation of target grating period, λ_{Bragg} is set to be equal to or in the vicinity of the gain medium's PL spectral peak wavelength at device operation temperature (80K) which is at 3.06 μm for our case as given in the previous section. Then grating period can be calculated with above equations 2.5 and 2.6 once effective refractive indices are determined. Since the period of hyperbolically chirped grating on our device varies at different locations, the target Bragg grating period (with assumption of straight grating or constant grating period) acquired through the above method will be taken as the center grating period of some target grating period range. This target range of the grating period on the actual tunable DFB laser device is determined to fully take advantage of the bandwidth of gain spectrum to achieve the widest wavelength tuning range. In addition, the grating period range also depends on the available lenses for IL setup as to be shown in the following section about chirped grating period calculation.

2.3.3 Coupling Strength

Coupling strength is the product of the coupling coefficient κ and physical grating length L_g, used to characterize the feedback from the Bragg grating of a DFB laser. Assuming that the discontinuity of effective refractive indices in grating ridge and groove segments is small enough, then coupling strength of the Bragg grating can be given as following equation 2.7. Many different equations could be found for κL_g calculation, the reason we chose this is because of its simplicity. It needs to be emphasized that this equation is meant for non-chirp straight grating case. But it should be still applicable for our chirped grating design, considering the grating chirp along the pump stripe is small as shown in the next few sections. Equation 2.7 provides an estimation of the coupling strength for our device design.

$$\kappa L_g = \frac{L_g}{\Lambda} \cdot \frac{\triangle n_{Eff}}{\bar{n}_{Eff}} = \frac{2L_g \triangle n_{Eff}}{\lambda_{laser}} \tag{2.7}$$

Where $\triangle n_{Eff}$ is the effective refractive index difference between the cases with top clad layer as thick as the grating ridge or groove segment. And λ_{laser} in equation stands for the lasing wavelength. For the calculation of coupling strength in our laser device design, λ_{laser} is set to be 3.06 μm , matching the PL spectral peak wavelength at 80K.

2.3.4 Confinement Factor

The confinement factor is the fraction of intensity profile of a guided mode within the active or core region in the waveguide. For our laser device with a slab waveguide structure, it can be given by the following well known equation.

$$\Gamma(Z) = \frac{\int_{ActiveRegion} \vec{E} \cdot \vec{E}^* dZ}{\int_{-\infty}^{+\infty} \vec{E} \cdot \vec{E}^* dZ} = \frac{\int_{-d_0}^{+d_0} E_Y(Z) \cdot E_Y(Z)^* dZ}{\int_{-\infty}^{+\infty} E_Y(Z) \cdot E_Y(Z)^* dZ} \tag{2.8}$$

Where $\vec{E}$ and $\vec{E}^*$ stand for the electric field amplitude and its conjugate value and Z is the epitaxial growth direction, or transverse direction as referred in this dissertation.

Accurately speaking, *ActiveRegion*, the subscript that defines the integral range in the above equation means where electron-hole recombination occurs, namely the InGaSb and InAs QWs inside the core layer of the slab waveguide structure. So the lower and upper limits in the equation numerator integral are not correctly defined. But it is fair to assume that the confinement factor in the core region of the waveguide is proportional to that in the actual active region. So the above expression is used to define confinement factor of our tunable DFB laser device. Once the guided mode electric field profile is calculated as shown in the section 2.3, confinement factor can be easily acquired with above equation 2.8.

After the introduction of the above constraints in generic grating design of a DFB laser and our device as a particular case, the practical parameters need to determine for our device design can be simply summarized as following.

1. How thick should the top clad (distance from grating ridge top to core layer) of the slab waveguide be?

2. How deep do the grating grooves need to be etched into the top clad?

Based on all the known values such as PL spectral peak wavelength, refractive indices of different layers in slab waveguide, core layer thickness, effective refractive index, confinement factor and coupling strength as function of top clad thickness, D_R, and grating groove depth, D, are calculated with the introduced 4-layer slab waveguide model and plotted in Fig.2.6, 2.7 and 2.8.

Because confinement factor with top clad less than 500 nm thick is too low to meet the constraint presented previously, all the three figures are plotted with top clad thickness range from 500 nm to 1500 nm. For the same reason, in Fig 2.7, coupling strength is plotted only for cases with D_G equal or bigger than 500nm. In addition, due to the fact that the ICP recipe used for grating pattern transfer into

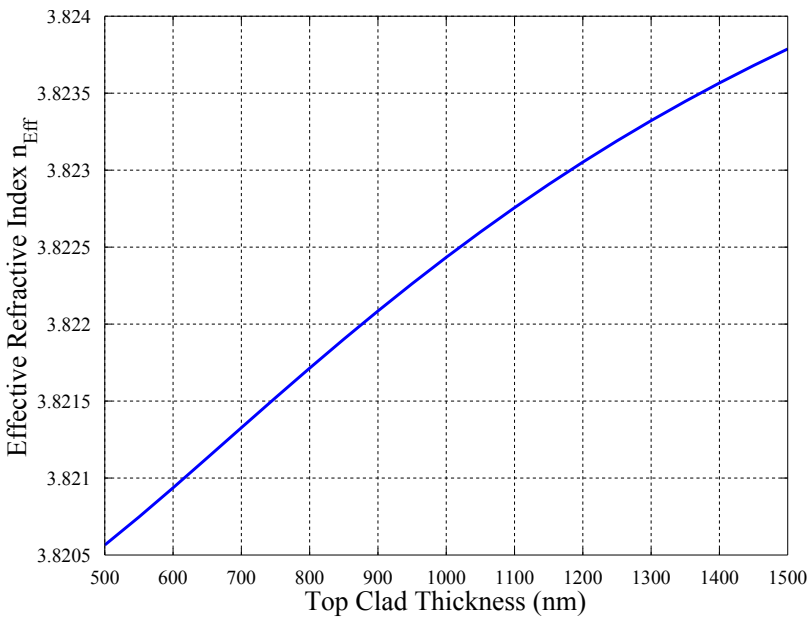

Figure 2.6: Effective refractive index of DFB device as function of top clad thickness of the slab waveguide

waveguide top clad doesn't give good etch profile for groove depth larger than 700 nm, the grating depth range plotted in this figure is from 50 nm to 700 nm with 50 nm increment. Shown in the Fig. 2.6 and 2.8, as thickness of the top clad increases, the effective refractive index of the slab waveguide sub-linearly increases, and the mode confinement increases as well. Coupling strength by equation 2.7 for 2.5 mm long grating as function of different combinations of top clad thickness, D_R and grating groove depth, D, is plotted in the Fig. 2.7. Generally speaking, coupling strength increases as the grating groove depth increases. But for a given grating groove depth, the coupling strength decreases as top clad thickness increases. The decreasing trend of coupling strength with deeper grating groove as top clad thickness increases is more obvious as shown in the figure. Any combinations of top clad thickness and grating groove depth between 1 and 3 as shown in the shaded area in the figure can be chosen for our device.

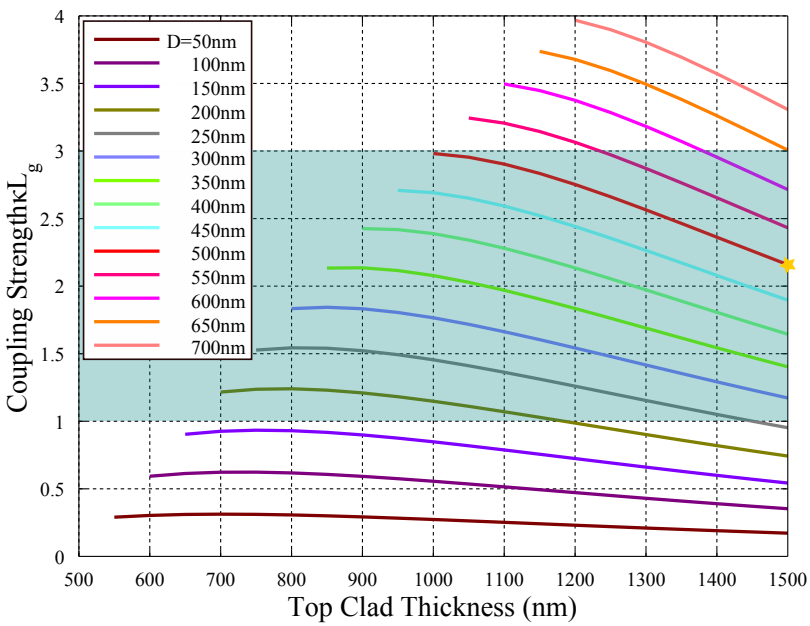

Figure 2.7: DFB laser device coupling strength, κL_g with grating length $L_g = 2.5mm$ as function of top clad thickness of slab waveguide and the grating groove depth D, assuming 50% duty cycle square grating case. Shaded area in the figure gives the target coupling strength range from 1 to 3. And the golden star corresponds to the actual parameters determined for our device fabrication, namely top clad thickness of 1500 nm and grating depth of 500 nm.

With calculation for effective refractive index, coupling strength and confinement factor with different top clad thicknesses and grating depths, we finally decided not to thin the top clad layer on wafer V9-18 and to etch the grating 500 nm deep into the top clad, taking into account the trade-off between the coupling strength and the confinement factor as shown in the Fig. 2.7 and 2.8. Effective refractive indices for top clad thickness of 1.5 μm (grating ridge) and 1.0 μm (grating groove) are 3.8238 and 3.8224 as labeled in the Fig. 2.5. Center Bragg grating period is about 405 nm. And the coupling strength for a 2.5 mm long grating DFB device is about 2.2 as shown by the golden star in the Fig. 2.7. Confinement factor is about 0.42. Effective refractive index acquired in the 4-layer slab waveguide turned out to be a bit larger than the fitted effective index with characterization data, which is about

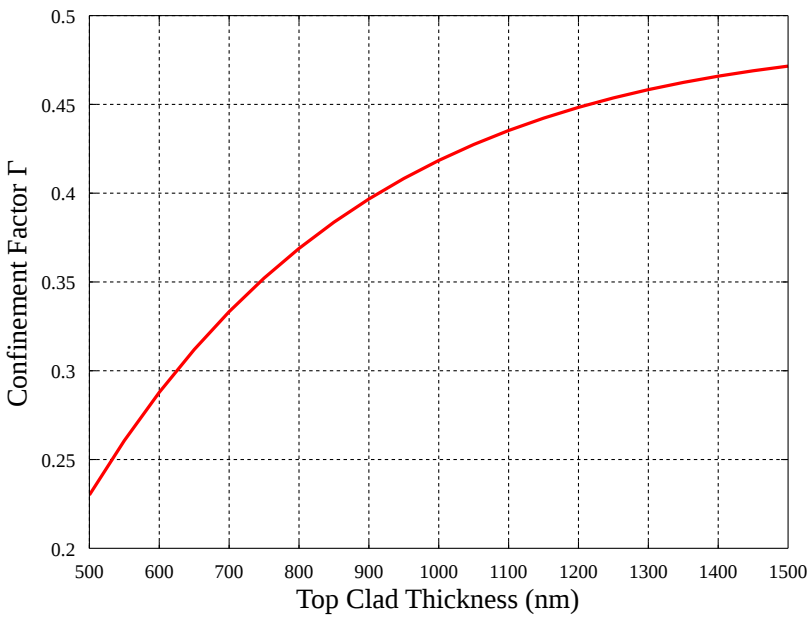

Figure 2.8: Confinement factor, Γ of DFB device as function of top clad thickness of the slab waveguide

3.75 as shown in Chapter 3.

2.4 IL Experimental Setup

As mentioned earlier in this chapter, interference between two spherical wavefronts is utilized to fabricated a chirped grating. With that in mind, we designed this experimental setup for IL as shown in Fig. 2.9. It is basically a Lloyd mirror setup mounted on a rotation stage with an extra spherical lens mounted perpendicular to the mirror, which converts the collimated incident beam into the spherical waves for interference. Coordinate systems (X, Y, Z) and (X', Y') are drawn as shown in the schematic to help better explain how this setup works for our purpose. For the same reason, collimated coherent incident beam coming from the left-hand side is intentionally drawn in two separate circular cross-section portions. One portion of

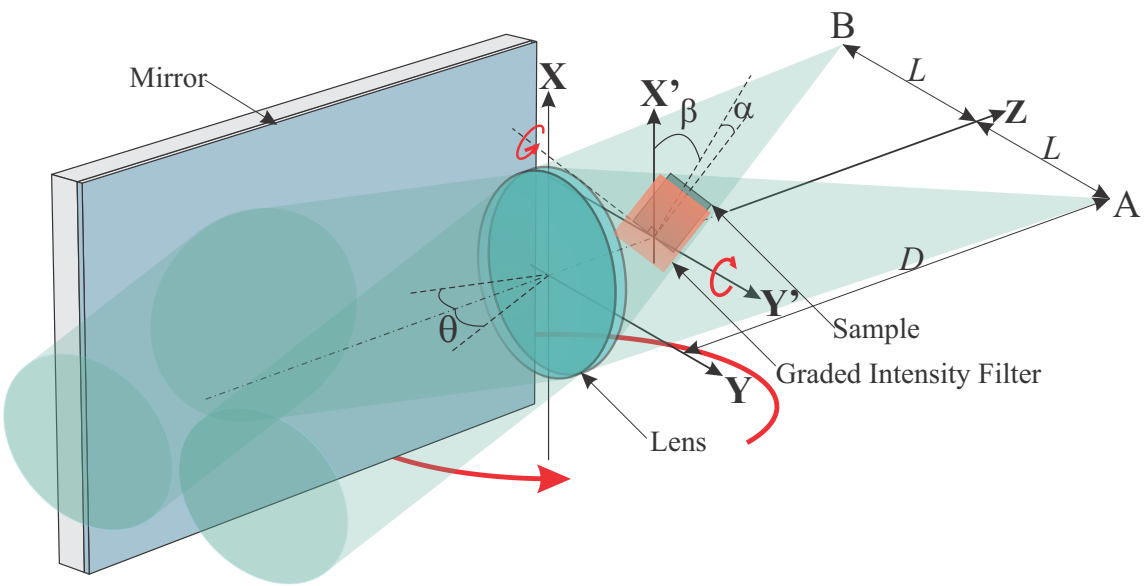

Figure 2.9: Schematic of interferometric lithography experiment setup to pattern chirped grating

incident beam impinges on the spherical lens directly then gets converted to spherical wave by the lens and focused at point **B**. Likewise, the other portion of the incident beam, after being reflected by the mirror, shines onto the lens then gets converted and focused at point **A**. When a photoresist (PR) pre-coated sample (In our case, it's a 10×10 mm die diced from the epitaxial growth wafer. For the rest of this dissertation, it is referred as the die.) is placed in the overlapped region of these two converging spherical waves as shown as the cone-shaped zone behind lens in the schematic, a quadratically chirped grating pattern will be registered in the PR layer.

In theory, any spherical lens could be used to get spherical wavefronts. But we decided to use a plano-convex lens with its curved surface facing the incident beam side because it is convenient to mount sample immediately next to the back surface if necessary. Coordinate system (X, Y, Z) is built with its origin located at the center of the back (flat) surface of the lens. And X, Y axis are parallel and perpendicular to the mirror respectively. Z axis is colinear with the optical axis of the lens and

pointing in the direction the light propagates. Some distance after the X-Y plane on Z axis, coordinate system (X', Y') is used to explain the positioning of the die in the experimental setup. X' and Y' are parallel to the X and Y respectively as shown. The die is tilted with angle β relative to the back surface of the plano-convex lens as labeled in schematic with the middle point of its bottom edge on Z axis. Meanwhile, the die is intentionally azimuthally rotated about it's normal for angle α to tilt the grating line orientation relative to edges of the die to suppress Fabry-Perot (F-P) modes. Die tilt and azimuthal rotation will be presented in detail in the following sections 2.6 and 2.7 .

As shown in the IL setup schematic of Fig. 2.9, incident beam falls into Y-Z plane and has incident angle of θ with respect to the axis Z or the optical axis of plano-convex lens. Due to the particular geometric configuration of the optical elements in the IL experimental setup, foci **A** and **B** are also located in the Y-Z plane and are symmetric with respect to Z axis. L is the half separation of the foci **A** and **B**. Their distance to the back flat surface of lens is labeled as D. L and D are the parameters we need solve first for the calculation of chirped grating period as function of location on the die. They both are lens and beam incident angle θ dependent. Calculation of L and D will be presented in the following section 2.6.

2.5 Lateral and Longitudinal Chirps in Grating

Due to the fact that the grating is acquired from interference of two spherical wavefronts as explained, grating lines are hyperbolic which means grating period varies in two orthogonal directions at the same time. To characterize this hyperbolically chirped grating, two different types of chirp along these two directions are defined in this section.

Before that, it is necessary to introduce two typical pump stripe orientations for

our tunable DFB laser as shown in Fig. 2.10, in which these two orthogonal directions required for chirp definition are also introduced. The rectangles with shaded lines in the figure stand for the DFB laser device cleaved from patterned die. Their left/right laterals correspond to the front/back device facets. And the shade lines titled with respect to the facets stand for the grating line orientation on the device due to the azimuthal rotation of angle α in IL exposure as mentioned in the previous section. Pump stripe, shown as the blue stripe can be applied either normal to the facets or the grating lines as shown in the part a) and b) in the Fig. 2.10. These two different configurations are referred as facet normal configuration (FNC) and grating normal configuration (GNC) respectively. When talking about device or die dimensions, longitudinal direction means the horizontal direction and lateral direction means the vertical direction or along facets as labeled in the part a) of the Fig.2.10. When talking about grating chirps, longitudinal direction is along the pump stripe orientation and lateral direction is the direction perpendicular to longitudinal direction. In short, device dimensional directions coincide with grating chirp directions for FNC, but are different for GNC as shown in the figure. Additionally, optical pump stripe orientation can actually be rotated to an arbitrary angle relative to device facets or grating lines for wavelength tuning purpose [130, 131]. But this technique is out of the scope of this dissertation and will not be presented here.

Although the pump stripe has the flexibility of being applied in these two configurations, only GNC is preferred. Since pump stripe is not normal to the laser device facets, F-P modes from facet feedback are successfully suppressed. Also because of the pump stripe configuration GNC, laser output beam shown in red in the part b) of Fig. 2.10 is not perpendicular to the facets but holds an angle of about 23.5° determined by the Snell's law. All the device characterization results presented in Chapter 3 are done in GNC.

With these two directions explained, longitudinal and lateral chirps are defined

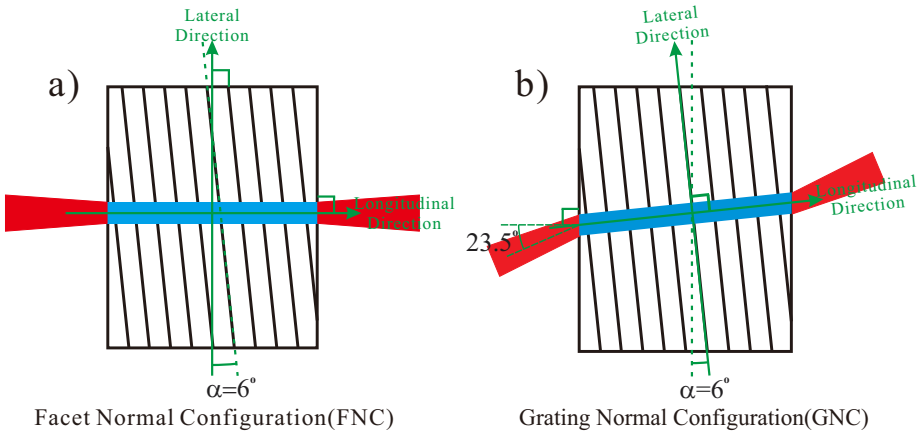

Figure 2.10: Two different pump stripe orientations in laser operation, FNC and GNC.

as follows.

Longitudinal Chirp: Grating period variation along the pump stripe, which is not necessarily perpendicular to the grating line orientation as shown in FNC.

Lateral Chirp: Grating period variation along the direction perpendicular to the pump stripe, in both GNC and FNC.

Things to bear in mind are that lateral chirp is desirable because it is what we use to tune the lasing wavelength. Longitudinal chirp has both positive and negative effects on the performance of DFB laser devices [15,17,132–144]. In this dissertation, we mainly concern its impacts on laser's spectral linewidth so that it needs to be avoided or at least kept under control. To characterize the aforementioned two types of grating chirps, figure of merit (FOM) is defined as the ratio of lateral chirp to longitudinal chirp, as shown in the following equation.

$$FOM = \frac{\Delta\Lambda|_{LateralDirection}}{\Delta\Lambda|_{LongitudinalDirection}}|_{GivenArea} \tag{2.9}$$

The goal for optimization of this quadratically chirped grating is to maximize the value of FOM and control the value of longitudinal chirp at the same time. As dis-

cussed below, the die tilting (rotate sample about Y' axis by angle β as mentioned and shown in the Fig. 2.9) with respect to the back surface of the lens in IL exposure, allows some control of FOM. In section 2.8, FOM and variation of lateral and longitudinal chirp as function of die tilting angle β and some other parameters will be discussed in detail, after calculation of grating period is introduced in the next section.

2.6 Calculation of Quadratically Chirped Grating Period on Die

The derivation of the chirped grating period as function of location on the die surface is to be done in such procedure listed below.

Step 1. Get coordinate transformation between pattern space (X, Y, Z) and sample space (u, v), namely to get the expression of X, Y, Z in terms of u, v respectively. These two spaces will be introduced in sub-section 2.6.1.

Step 2. Write the expression of interference pattern in pattern space, basically the interference fringe pattern as function of coordinates (X, Y, Z) in the pattern space.

Step3. Substitute coordinates (X, Y, Z) with (u, v) according to the relation derived in Step 1. to get the expression of chirped grating period as function of location (u, v) on the die.

2.6.1 Coordinate Systems

For the convenience of explanation, two coordinate systems need to be introduced before we start deriving this hyperbolically chirped grating period expression on the

die. They are shown in the following Fig. 2.11. The first one is a 3-D so-called "pattern" space required to describe the locations of optics in experimental setup, relevant spatial parameters in grating period calculation and interference fringe in space. It is defined with coordinates (X, Y, Z). The second coordinate system is a 2-D "sample" space meant for the die surface on which chirped grating is to be patterned. For clarity in derivation, a 3-D coordinate system defined by (u, v, γ) is temporarily used. But what actually needed is just the u-v plane corresponding to the die top surface that faces in γ direction as shown in the Fig. 2.11 b). To derive the expression for hyperbolically chirped grating patterned by IL on die surface, we will start with the transformations between these two coordinate systems, (X, Y, Z) and (u, v, γ), which will make the whole derivation easy to understand.

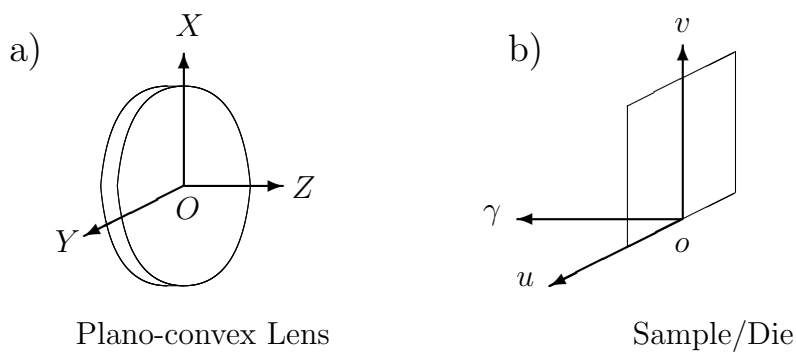

Figure 2.11: Coordinate systems for pattern space and sample space.

In pattern space, coordinate system (X, Y, Z) is built as introduced in section 2.4 and as shown in Fig.2.9 and 2.11 a), with plano-convex lens' back/flat surface sits in X-Y plane and its optical axis colinear with Z axis. the lens curved surface faces in the $-Z$ direction. For the sample space (u, v, γ), coordinate system is constructed as shown in Fig. 2.11 b). The Origin is chosen to be at the middle point of the bottom lateral of the 10×10 mm die. u axis is in the horizontal direction parallel to the top/bottom lateral, and v axis is in the vertical direction. Before die tilt and azimuthal rotation, u and v axes are parallel to the X and Y axes respectively and

γ axis points to $-Z$ direction as shown in Fig. 2.11. Both pattern and sample space coordinate systems are right-handed systems.

2.6.2 Sample Position and Coordinate Transformations

From its reference position, against the back surface of the lens with u, v axes colinear with the X, Y axes respectively, the die can be moved to its actual position in IL exposure with three operations, namely tilt relative to the back surface of the lens with angle β; azimuthal rotation about its own surface normal for angle α; and translation from the origin with offsets C_x, C_Y and C_Z in X, Y, Z directions respectively. To describe the actual positioning of the die in IL patterning, these operations could be mathematically defined as three coordinate transformations represented by different matrices and applied in the following order as shown. Combining them together, the mapping relation between the pattern space coordinates (X, Y, Z) and sample space space coordinates (u, v, γ) can be obtained, which is required to calculated the chirped grating period on the 10×10 mm die. Mathematically, the first two transformations are identical, which is coordinates rotation about one of the three axes in Cartesian coordinate system as defined in appendix A. The third transform is just translation of a Cartesian coordinate system. In the derivation of the mapping relation between pattern space coordinates (X, Y, Z) and sample space coordinates (u, v, γ), another intermediate coordinate system (u', v', γ') is used to better explain the coordinate transformations. The aforementioned three coordinate transformations are listed as followings.

1. "Tilt" of sample relative to the back surface of the plano-convex lens that is equivalent to a rotation of pattern space (X, Y, Z) about Y axis or sample space (u, v, γ) rotate about the u axis for angle β.

2. "Azimuthal rotation" of sample about its surface normal, γ axis for angle α.

3. Translation of the origin of the sample space coordinate system (u, v, γ) in pattern space with offsets of C_X, C_Y, C_Z from origin O. The Origin of sample space coordinate system (u, v, γ) falls in X'-Y' plane on IL experimental setup as shown in Fig. 2.9.

Transformation 1., die tilt relative to the back surface of the plano-convex lens could be defined with matrix A_1 as shown below. Equation 2.10 presents the rotation operation of intermediate coordinates (u', v', γ') about u' axis to get the pattern space coordinates (X, Y, Z).

$$\begin{bmatrix} X \\ Y \\ Z \end{bmatrix} \equiv \begin{bmatrix} 0 & \cos\beta & \sin\beta \\ 1 & 0 & 0 \\ 0 & \sin\beta & -\cos\beta \end{bmatrix} \begin{bmatrix} u' \\ v' \\ \gamma' \end{bmatrix} = A_1 \begin{bmatrix} u' \\ v' \\ \gamma' \end{bmatrix} \tag{2.10}$$

Likewise, transformation 2. which is the azimuthal rotation of sample about its surface normal, axis γ could be defined with A_2 as below. Equation 2.11 shows this operation to get from sample space coordinates (u, v, γ) to the intermediate coordinates (u', v', γ').

$$\begin{bmatrix} u' \\ v' \\ \gamma' \end{bmatrix} \equiv \begin{bmatrix} \cos\alpha & \sin\alpha & 0 \\ -\sin\alpha & \cos\alpha & 0 \\ 0 & 0 & 1 \end{bmatrix} \begin{bmatrix} u \\ v \\ \gamma \end{bmatrix} = A_2 \begin{bmatrix} u \\ v \\ \gamma \end{bmatrix} \tag{2.11}$$

So combining the first two transformations, relation between coordinates in pattern space (X, Y, Z) and those in sample space (u, v, γ) is given by the following equation.

$$\begin{bmatrix} X \\ Y \\ Z \end{bmatrix} = A_1 A_2 \begin{bmatrix} u \\ v \\ \gamma \end{bmatrix} = \begin{bmatrix} 0 & \cos\beta & \sin\beta \\ 1 & 0 & 0 \\ 0 & \sin\beta & -\cos\beta \end{bmatrix} \begin{bmatrix} \cos\alpha & \sin\alpha & 0 \\ -\sin\alpha & \cos\alpha & 0 \\ 0 & 0 & 1 \end{bmatrix} \begin{bmatrix} v \\ u \\ \gamma \end{bmatrix} \tag{2.12}$$

The entire coordinate transformation taking into account all above three transformations including the translational offsets of the sample in coordinate system (X, Y, Z)

with respect to its origin in IL patterning could be written as

$$\begin{bmatrix} X \\ Y \\ Z \end{bmatrix} = A_1 A_2 \begin{bmatrix} u \\ v \\ \gamma \end{bmatrix} + \begin{bmatrix} C_X \\ C_Y \\ C_Z \end{bmatrix}. \tag{2.13}$$

As mentioned before that we only care about the die surface when calculating the grating period as function of the location on its surface. Mathematically, this means to let $\gamma = 0$ in the above expression. Which is,

$$\begin{bmatrix} X \\ Y \\ Z \end{bmatrix} = \begin{bmatrix} -\cos\beta\sin\alpha & \cos\beta\cos\alpha & \sin\beta \\ \cos\alpha & \sin\alpha & 0 \\ -\sin\beta\sin\alpha & \sin\beta\cos\alpha & -\cos\beta \end{bmatrix} \begin{bmatrix} u \\ v \\ 0 \end{bmatrix} + \begin{bmatrix} C_X \\ C_Y \\ C_Z \end{bmatrix}. \tag{2.14}$$

Space coordinates (X, Y, Z) in the above matrices can be rewritten in terms of sample space coordinates (u, v), as shown in the expressions below.

$$X = -u\cos\beta\sin\alpha + v\cos\beta\cos\alpha + C_X \tag{2.15a}$$

$$Y = u\cos\alpha + v\sin\alpha + C_Y \tag{2.15b}$$

$$Z = -u\sin\beta\sin\alpha + v\sin\beta\cos\alpha + C_Z \tag{2.15c}$$

2.6.3 Interference Pattern in Pattern Space

The method to calculate the interference pattern of these two spherical waves is based on the fact described in the following sentence. If at any point in the pattern space, its optical path length to the two source points of the interfering spherical waves is multiple of the wavelength, then at this particular point electric field has constructive interference from the above mentioned waves. Or if a screen is put at this location, a bright spot can be seen on it. Likewise, if the difference of the optical path length

from this particular point to the source points of the spherical waves is odd multiple of half wavelengths, interference between these two waves will be destructive. All the points with these attributes in the pattern space form bright and dark fringes that could be recorded with screen at arbitrary positions. In here, the screen or the medium that we use to record the fringes is the photoresist (PR) pre-coated on the die. These bright or dark fringes are the grating lines we are trying to pattern in PR. Due the attribute that optical rays are reversible, we can take the foci, A and B as shown in Fig. 2.9, formed by the two converging spherical waves after lens in the IL experimental setup in section 2.4 as the source points. Because the geometric configuration of the optics in our IL experimental setup and the construction of the coordinate system as shown in Fig. 2.9, assuming the incident beam is in Y-Z plane, then the foci A and B should be in the same plane and their location coordinates are $(0, L, D)$ and $(0, -L, D)$ respectively, as labeled in figure. With these explained, the expression that defines the difference of optical path length from a arbitrary point (X, Y, Z) in pattern space to these foci to get constructive interference can be written as following.

$$m\lambda_0 = \sqrt{X^2 + (Y+L)^2 + (D-Z)^2} - \sqrt{X^2 + (Y-L)^2 + (D-Z)^2} \quad m \in I \quad (2.16)$$

Where λ_0 is the vacuum wavelength of spherical waves in IL patterning which is 355 nm from a frequency tripled Nd:YAG laser.

In the pattern space, the interference pattern/chirped grating period as function of location then can be written as expression shown below.

$$\Lambda(X, Y, Z) = \frac{\lambda_0}{|\nabla m(X, Y, Z)|} \quad (2.17)$$

Where ∇m is the gradient of integer m in pattern space. Every time m is changed by 1, above equation will give a interference fringe curve in pattern space corresponding to a bright fringe.

2.6.4 Chirped Grating Period on Die

To get the chirped grating period as function of location on the die, we just need to substitute (X, Y, Z) in equation 2.17 with coordinates (u, v) in sample space with their relation given by equation 2.15 to get the following equation for chirped grating period on the die .

$$\Lambda(u,v) = \frac{\lambda_0}{|\nabla m(u,v)|} = \frac{\lambda_0}{\sqrt{(\partial m/\partial u)^2 + (\partial m/\partial v)^2}} \tag{2.18}$$

After some mathematical manipulations, the grating period on the die can be written as following. To make the expressions brief and neat, we still use the pattern space coordinates X, Y and Z in them. In the calculation or plot of grating period, they need to be substituted with sample space coordinates (u, v) as shown in equation 2.15.

$$\Lambda(u,v) = \frac{\lambda_0}{\sqrt{(Term_1 - Term_2)^2 + (Term_3 - Term_4)^2}} \tag{2.19}$$

Where $Term_1$, $Term_2$, $Term_3$ and $Term_4$ are listed in the following expressions respectively.

$$Term_1 = \frac{X\cos\beta\cos\alpha + (Y+L)\sin\alpha - (D-Z)\sin\beta\cos\alpha}{\sqrt{X^2 + (Y+L)^2 + (D-Z)^2}} \tag{2.20a}$$

$$Term_2 = \frac{X\cos\beta\cos\alpha + (Y-L)\sin\alpha - (D-Z)\sin\beta\cos\alpha}{\sqrt{X^2 + (Y-L)^2 + (D-Z)^2}} \tag{2.20b}$$

$$Term_3 = \frac{-X\cos\beta\sin\alpha + (Y+L)\cos\alpha + (D-Z)\sin\beta\sin\alpha}{\sqrt{X^2 + (Y+L)^2 + (D-Z)^2}} \tag{2.20c}$$

$$Term_4 = \frac{-X\cos\beta\sin\alpha + (Y-L)\cos\alpha + (D-Z)\sin\beta\sin\alpha}{\sqrt{X^2 + (Y-L)^2 + (D-Z)^2}} \tag{2.20d}$$

2.6.5 Calculation of Hyperbolically Chirped Grating Period on Real Tunable DFB Laser Device

In this sub-section, chirped grating on the 10×10 mm die from which our tunable DFB laser device characterized in Chapter 3 will be presented as an example of the hyperbolically chirped grating period calculation. To calculate the grating period as function of location on the die, we still need the values of L, D, β and α. Die tilting angle β in IL patterning is set at 45° and azimuthal rotation angle of die, α is 6° which means the die is azimuthally rotated 6° clockwise about γ axis. Translational offsets C_X and C_Y are set to 0 mm. C_Z in the equation 2.19, the Z-offset in pattern space of the origin of sample space coordinate is 2 mm in our calculation. The chosen setting values of β, α, C_X, C_Y and C_Z are mainly for maximum FOM as defined in section 2.5 and the reason why they are set at these values will be explained in detail in section 2.8. L and D for the locations of foci A and B can not be directly set. They have to be calculated before grating period calculation.

As mentioned in the previous section, L and D are plano-convex lens and incident angle dependent. The lens we selected for grating patterning for our DFB laser device is a PLCX-50.8-51.5-UV from CVI Melles Griot whose dimensional information and material refractive index can be found online [145]. Incident angle θ was acquired in a recursive manner that we started with some guessed initial value, then adjust the incident angle according to the patterned grating period measurement results at a series of locations on dummy samples, till we reach the expected range of grating period to match with the gain spectrum in PL measurement of the wafer. The incident angle used in IL exposure of the chirped grating patterning for the die of real DFB laser device characterized in the Chapter 3 is about 21.7°.

Due to the reason that the incident angle is too large to apply paraxial equations for foci location calculation, we decided to analytically and graphically solve for L

and D with ray tracing approach using Snell's law. The calculation of the values of L and D is done in Matlab and plotted in Fig. 2.12. The calculated foci locations match the measurement conducted on IL setup very well. Assuming the collimated incident beam is in the Y-Z plane, then the locations of the foci also should be in the same plane as mentioned in the previous section. Also due to the geometric configuration of the IL setup and construction of pattern space coordinate system, locations of foci A and B are symmetric with respect to Z axis. So only location of either focused point needs to be solved and the location of the other can be easily acquired by mirroring the location of the solved one with respect to Z axis. With the dimensions of the lens, refractive index and the incident angle known, Snell's law is used to get the refraction angles and the positions of each ray at the front and back surfaces of the lens, till they cross each other behind the lens. The ray tracing calculation is shown in the Fig. 2.12. Five equally separated parallel incident rays in green come from the left hand side at angle $\theta = 21.7°$, get refracted on the front and back surface of the lens and finally converge after passing through the lens, with rays in and behind lens drawn in blue and magenta respective as shown in the figure. Due to spherical aberration of the lens, the five rays do not cross each other at single point after the lens. Although the locations of all these cross points are calculated, the final location of the focused point is manually determined as the mass center of the triangle formed by the three middle rays. The values of the L and D acquired by above explained method are 32.98 mm and 76.47 mm respectively. The Matlab code solving for foci locations can be found in Appendix C.2.

With all the parameters in equation 2.19 determined, the quadratically chirped grating period contour on the 10×10 mm die is solved and plotted in Fig. 2.13. Obviously, these quadratically chirped grating lines show hyperbolic patterns and the grating period and angle are both location dependent. Over the entire 10×10 mm die, the grating period varies in the range from about 405 nm to over 440 nm. The 4×2.5 mm actual tunable DFB laser device characterized and presented in Chapter 3

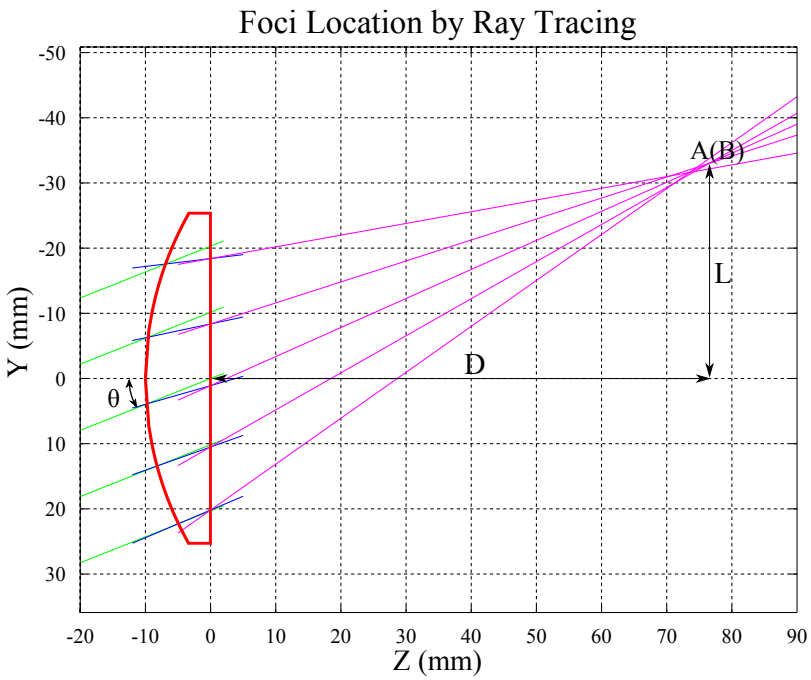

Figure 2.12: Ray tracing solution for the locations of foci A and B. The location of A(B) at (0, ±L, D) corresponds to the focused points of the converging spherical waves. L, D are labeled as shown.

is cleaved from the upper middle section of the die with exactly same chirped grating as shown in the figure. The specific location and dimensions from where device is cleaved from the die will be discussed in the following section 2.8. The Matlab code for the grating contour plot can be found in Appendix C.3.

2.7 Grating Angle

In so-called conventional DFB lasers, gratings are usually fabricated parallel to the laser facets. If the facets are not properly anti-reflection coated, then facet feedback will interfere with the distributed feedback from grating and possibly overtakes its function for wavelength selection especially under high power pump conditions, which

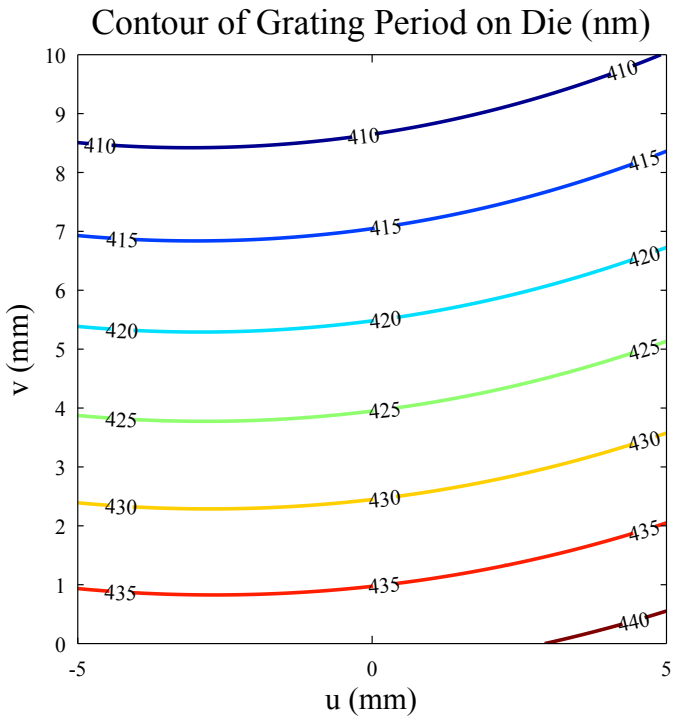

Figure 2.13: Chirped grating period contour on a 10 × 10 mm die, with die titling angle β=45°, azimuthal rotation angle α=6°, offsets $C_X = C_Y = 0$ mm and $C_Z = 2$ mm.

is the reason these lasers only operate as DFB lasers at fairly low output power.

In the design of this tunable DFB laser, we decided not to anti-reflection coat the facets not only because it is not a process very easy to control the coating quality across a wide wavelength range but also because the issue of coating peeling-off due to the different thermal expansion coefficients between the coating layers and the device, as well as nonuniform local heating from pump stripe in operation induces uneven thermal expansion. To suppress the Fabry-Perot (F-P) modes due to the feedback from laser facets, we intentionally apply an azimuthal rotation of the die for angle α about its surface normal as mentioned in the previous section such that the patterned grating line orientation is tilted with respect to the device facets after

it is cleaved from the die. So if the pump stripe is applied perpendicular to the grating line orientation (GNC) in operation, which is not normal to the facets, F-P modes are successfully suppressed in lasing, as presented in Chapter 3.

In this section, the grating line orientation or grating angle on the 10×10 mm die will be presented. For the exactly same chirped grating patterned on the die as shown in the Fig. 2.13, its line orientation or grating angle contour on the die is calculated and plotted in the Fig. 2.14. As seen in the figure, grating angle contour is overlaid on top of the grating period contour. Because of the existing quadratic chirp, grating angle varies by a few degrees over the 10×10 mm die, which means the grating lines along the pump stripe hold different angles at different locations, as shown in the Fig. 2.10. Obviously different from straight grating case for most typical DFB lasers, this angle variation affects the feedback of the grating, lowers the coupling strength, causes extra losses that increase the lasing threshold as well. Fortunately, the laser device cleaved from the die with dimensions of 2.5×4 mm in longitudinal and lateral direction respectively, the angle variation along pump stripe should be roughly a quarter of value shown in the Fig. 2.14. So the grating angle variation along the pump stripe does not affect the laser performance significantly, as discussed in the following sections. In the simulation of the grating feedback and wavelength selection presented in Chapter 4, we take into account both the grating angle and period variation in the construction of the laser cavity transfer matrix as will be presented.

The equation derived for grating angle calculation shown below is based on the gradient of integer m, ∇m as introduced in sub-section 2.6.4. The Matlab code used to calculate the grating angle and plot this figure can be found in Appendix C.4.

$$GratingAngle(u,v) = \pi - tan^{-1}(\frac{\partial m/\partial v}{\partial m/\partial u}) \tag{2.21}$$

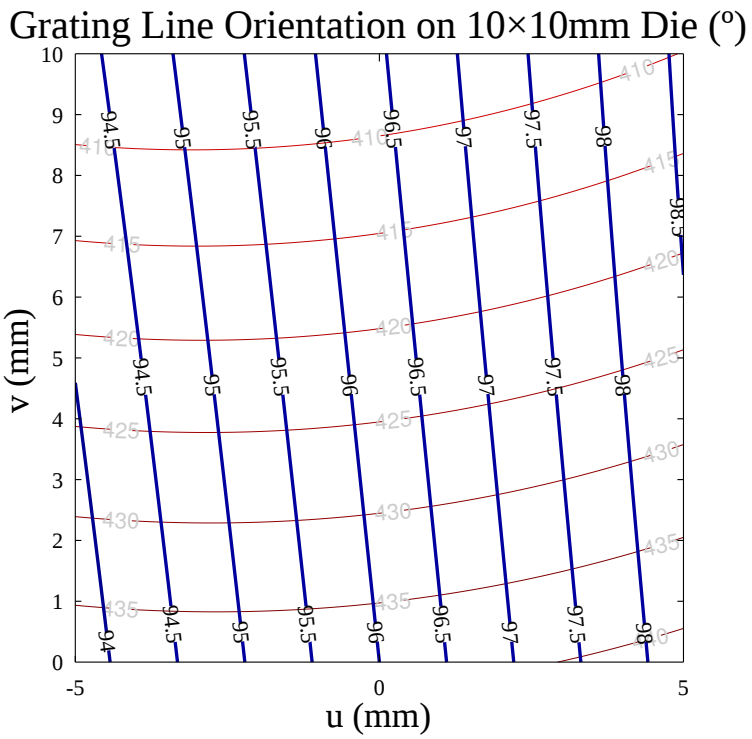

Figure 2.14: Chirped grating line orientation on a 10×10 mm die. Die tilting angle β=45° and azimuthal rotation angle α=6°. translational offsets C_X=C_Y=0 mm and C_Z=2 mm.

2.8 Discussion About The Chirped Grating

In this section, FOM on a 2.5×4 mm device as function of translational offsets C_X and C_Y with die tilting angle β as parameter will be calculated first to prove that to maximize FOM as a goal of the chirped grating optimization, the die positioning parameters set in IL exposure are necessary. After that, the grating tilting angle with respect to pump stripe in GNC as function of C_X, C_Y and β will be discussed. It has to be pointed out that FOM is also function of some other parameters such as α, C_Z or L and D, but they do not impact FOM's value as significantly. So to simplify the discussion, we temporarily take FOM as function of only β, C_X and C_Y. These values were actual numbers used in grating fabrication of real DFB laser device as

well as the calculation of grating period and angle on the 10×10 mm die presented in previous sections. To further simplify the calculation, plots and discussion of FOM and also the grating tilt angle relative to pump stripe, die azimuthal angle α is set to be 0°. This should not change the setting values of β, C_X and C_Y for real device fabrication with α=6°. Neither will the results presented in grating tilt angle change for real device with α=6°, considering the grating normal configuration for pump stripe. After these, α of 6° is taken into account in the calculation of the lateral and longitudinal chirp on real 10×10 mm die. Based on these calculation results, cleaving location of 2.5×4 mm device is determined for fabrication at the end of the section. DFB laser device longitudinal dimension of 2.5 mm is determined for comparison with previously fabricated devices and its lateral dimension of 4 mm is decided to avoid substrate cleavage in operation due to the uneven thermal expansion from local heating by the optical pump stripe.

2.8.1 Determine β, C_X and C_Y to Maximize FOM

As mentioned in section 2.5, the goal of chirped grating optimization is to maximize the FOM. This can be achieved by varying the die tilt angle β and die positioning translational offsets C_X and C_Y. Variation of C_Z will significantly change the chirped grating periods, but not the FOM.

Translational offsets C_X and C_Y define the off-axis (Z axis) shifts of the die in IL exposure corresponding to the translations of die in X'-Y' plane (Please refer to the Fig. 2.9) from its origin as shown in the part a) of Fig. 2.15. The half circle stands for the 2-inch diameter plano-convex lens used in IL and the small gray square behind it stands for the die to be exposed. Since we only care about the upper half space in X-Y plane, only the upper half of the lens is shown in the figure, which also defines the range of translational offset C_X and C_Y. For convenience in FOM

calculation, the ranges of C_X and C_Y are changed to the rectangular area as shown in the part b) of the figure, for which the entire die is exposed.

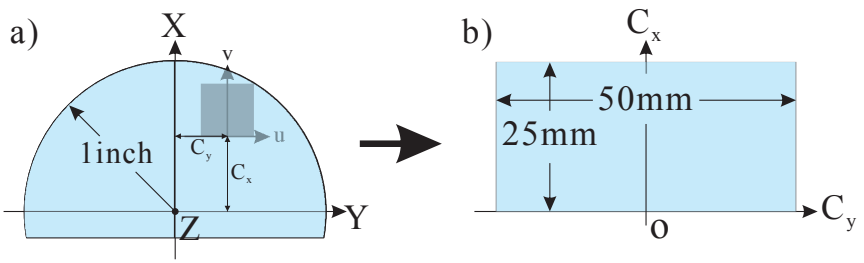

Figure 2.15: C_X and C_Y range definition for FOM calculation/plot

FOM over actual DFB laser device with dimensions of 2.5×4 mm is then calculated with the derived formula of chirped grating period, equation 2.19 presented in section 2.6. In this calculation azimuthal rotation angle α is set at 0° and die translational offset in Z direction, C_Z is 2 mm. FOM is taken as a function of C_X and C_Y with different die tilting angle β as parameter. With α=0°, lateral and longitudinal grating chirps are simplified to grating period variation along directions of v and u axes as indicated in the Fig. 2.15. FOM defined in equation (2.9) is then the ratio between the grating period variation along these two directions over device area. And the result of FOM as function of C_X and C_Y with β as parameter is plotted in Fig. 2.16.

As shown in the Fig. 2.16, FOM as function of translational offsets C_X and C_Y changes significantly with different die tilting angles, β. It gets peak values along line C_Y=0 mm and is symmetric with respect to this line for opposite signs of C_Y's, which is obvious since the interference fringes pattern in pattern space is symmetric relative to X-Z plane with no azimuthal rotation of the die in IL patterning. For the case when the die tilting angle β is 0° as shown in the figure, FOM value increases from small value at C_X=0 mm and gets its maximum value of about 50 at C_X=25 mm which physically corresponds to the top rim of the 2-inch diameter plano-convex

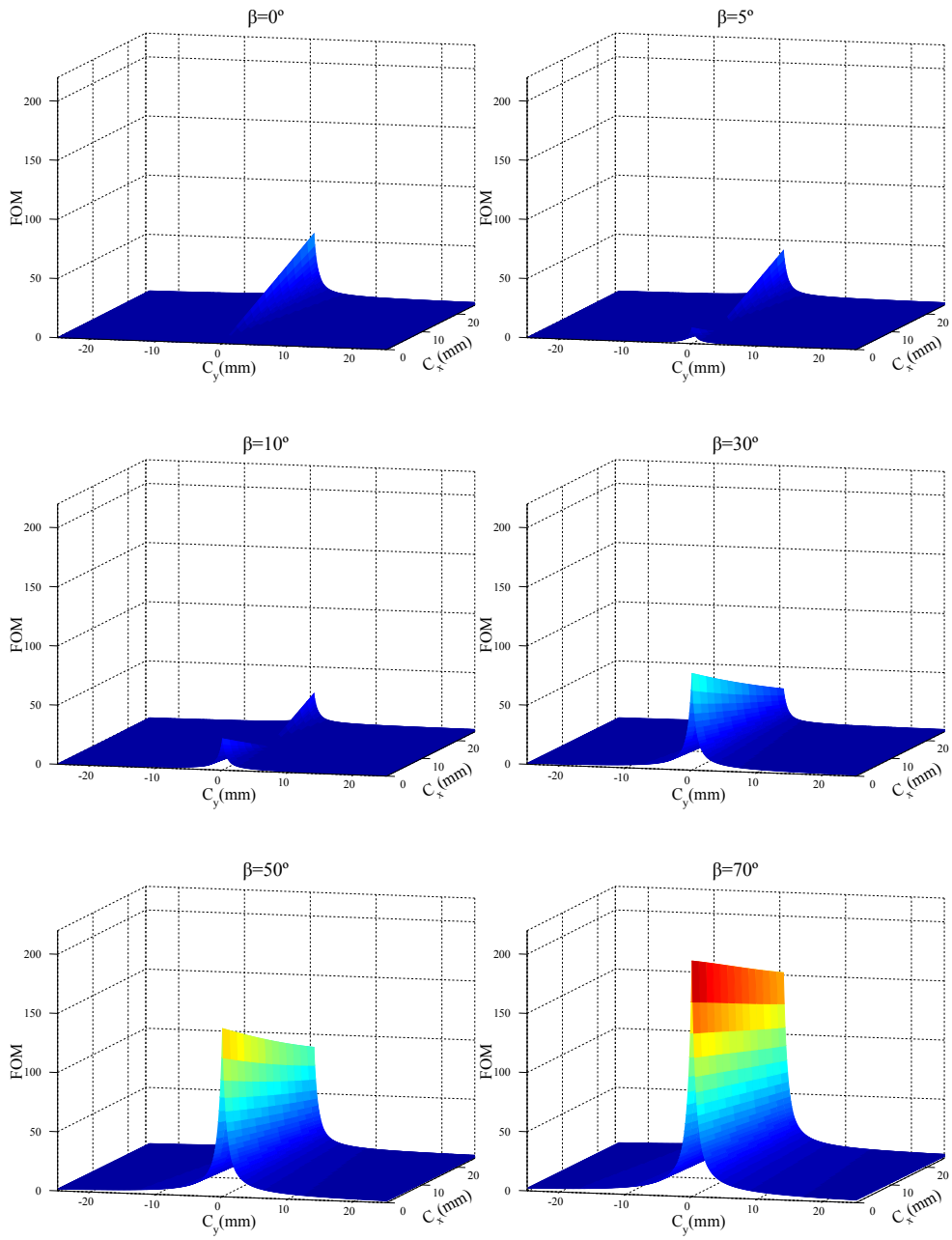

Figure 2.16: FOM as function of translational offsets, C_X and C_Y with die tilting angle β as parameter, azimuthal rotation angle α=0° and C_Z=2 mm.

lens. Taking into account the trend of FOM seen in this case, it should be possible to get a larger value if C_X further increases for a larger lens. As β increases, the

peak value of FOM at C_X=25 mm decreases at the same time another peak of FOM appears at location of C_X=0 mm as shown in the case β=5°. When β increases to 10°, these two peaks of FOM are almost equally high. Then, as β further increases, FOM peak at C_X=0 mm becomes the higher one of the two and gets larger quickly, meanwhile the original peak at C_X=25 mm shifts out of the range of C_X and C_Y defined in the Fig. 2.15. For the case of β=45° which is shown in Fig. 2.22 in a later section, FOM gets its maximum value of about 127 at C_X=C_Y=0 mm and decreases to 75 or so as C_X shifts to 25 mm. Value of FOM along C_Y=0 mm keeps increasing as β increases above 45°. Eventually, FOM will get his maximum value of about 225 at C_X=0 mm when β reaches 90° (not shown in the figure). So considering the FOM variation trend as β increase as shown in the Fig. 2.16, translational offsets C_X and C_Y should be at zero and β needs to be at 90° to maximize the value of FOM. This conclusion should be also applicable for different size and focal length of plano-convex lenses. Unfortunately, our present IL experimental setup can only set maximum die tilting angle of 45°, this is the reason why β was set at 45° and translational offsets C_X and C_Y were set at 0 mm in IL exposure and used in the the calculation of chirped grating period presented previous section. For actual grating patterning with azimuthal angle α is 6°, FOM might reach its peak value at slightly different locations on the die, but the above setting values of β, C_X and C_Y should hold still. C_X and C_Y stay at 0 mm for all the real device grating related calculations with α=6° in the rest of this chapter.

As mentioned earlier, FOM peak value of 127 acquired at β=45° and C_X=C_Y=0 mm can also be reached for the situation when β=0°, but the die has to be placed at the upper rim of a lens as large as 5 inches which is not practical. Besides, it is also impractical for die tilting angle β equal to 90° to maximize FOM because this grazing incident angle of interfering beams makes no light able to penetrate into PR to get it exposed to pattern the grating. This is also the reason why case of β=90° was not plotted in the Fig. 2.16. In addition, there is a trade off between FOM

and coupling of light energy into photoresist as function of die titling angle to get uniform grating pattern on the die. Nonetheless, modification of present IL setup to find a larger but practical die tilting angle is worth investigating.

2.8.2 Grating Tilt Angle Relative to Pump Stripe As Function of C_X, C_Y and β

As mentioned in section 2.5, the pump stripe is oriented perpendicular to the grating lines for all calculations and characterizations presented here. But due to hyperbolic grating pattern, grating lines hold different angle with respect to the optical pump stripe. In other words, not all of the grating lines are perpendicular to the pump stripe even in grating normal configuration. To quantize this angle variation of off 90° for all grating lines along the pump stripe, we calculated the angle between the grating lines and the pump stripe to get the range of this angle variation. To simplify the calculation of grating angle variation along the pump stripe, azimuthal rotation angle α was set zero and device dimension is 2.5×4 mm in longitudinal and lateral direction respectively. As shown in Fig. 2.17, grating tilt angle variation along pump stripe in GNC is plotted as function of translational offsets C_X and C_Y in the same range as defined in the Fig. 2.15, with die tilt angle β as parameter. For the situation when α=6° in real device fabrication, these results stay roughly the same.

As shown in the Fig. 2.17, grating tilt angle relative to the pump stripe is symmetric with respect to the line of C_Y=0 mm. The value of grating tilt angle variation relative to pump stripe stays almost the same along straight lines of C_X as constant which is also the direction of pump stripe in this calculation. At die tilt angle β=0°, value of grating tilt angle variation increases monotonically from 0° to over 0.5° as translational offset C_X gets larger. As β increases in the range from 0° to ∼19°, grating tilt angle variation along pump stripe first decreases from some

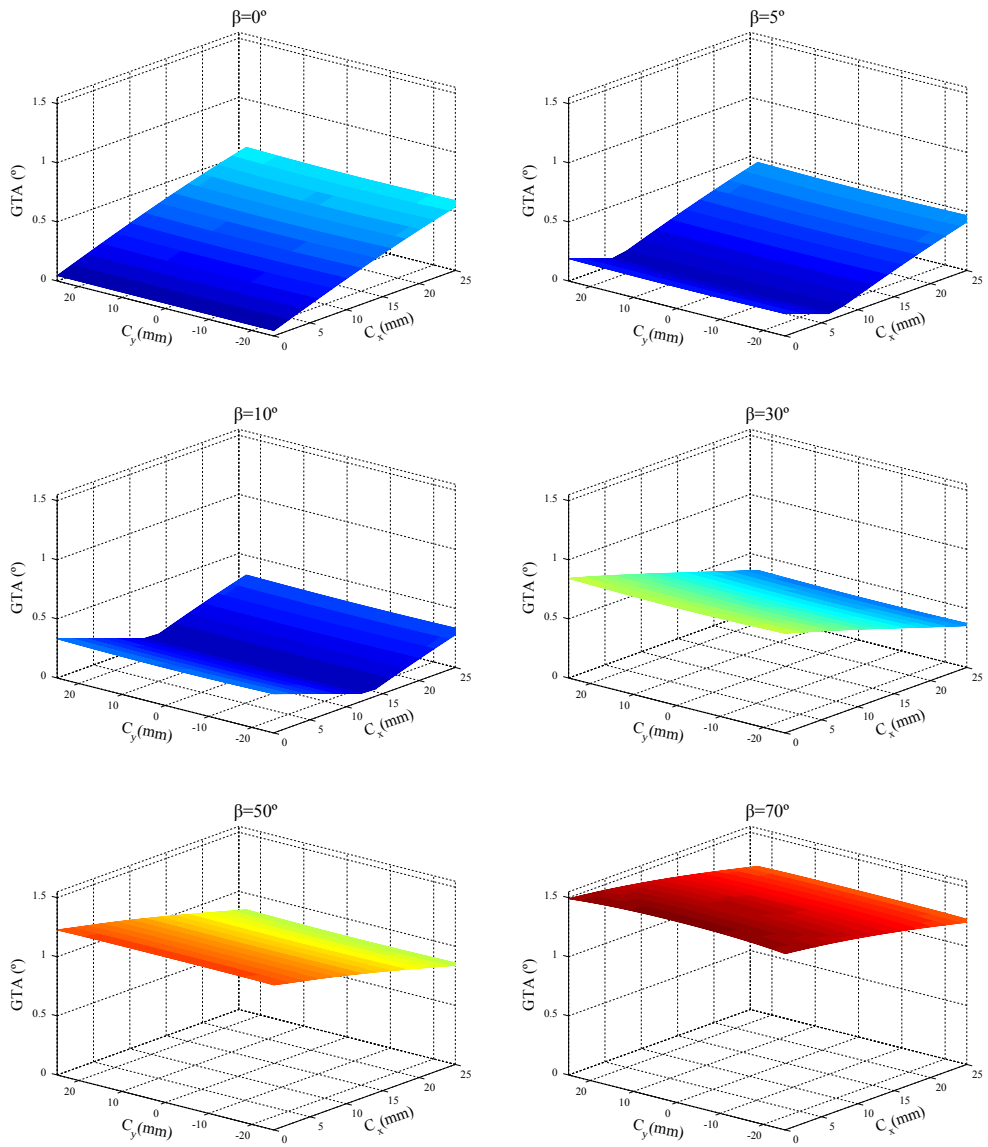

Figure 2.17: Grating tilting angle relative to pump stripe on 2.5×4 mm device as function of C_X, C_Y with β as parameter, α=0° and C_Z=2 mm

value to get its minimum and then increases again as C_X changes from 0 to 25 mm. Cases of β=5°, 10° are taken as examples to show this trend in the figure. Once β is larger than 20°, value of grating tilt angle variation decreases monotonically from its maximum at C_X=0 mm as C_X increases to 25 mm. Different cases with different

β values in the Fig. 2.17 show the changing trend of the grating tilt angle variation along pump stripe on a 2.5×4 mm device as die tilt angle β increase from 0° to 90°. For the extreme but not practical case of die tilt angle β=90°, the maximum grating tilt angle variation is about 1.55° at C_X=0 mm (not shown in the figure). In the case of real device fabrication with C_X=C_Y=0 mm and β=45° also not shown in the figure, the grating tilt angle variation along pump stripe takes value of about 1.14°.

Although the grating lines tilt variation relative to the pump stripe on the order of 1° seems not large, we still take into account actual non-normal angles in the construction of the cavity transfer matrix elements in simulation of our DFB laser device be presented in Chapter 4. But for simplification of the simulation, we neglect the loss or deviation of the counter-propagating electromagnetic waves in the cavity defined by pump stripe due to refraction of lights happening on the interface of grating ridge and groove segments because of oblique incidence as explained in Chapter 4. Due to the loss from this refraction just mentioned and the scattering of grating, our DFB laser's lasing threshold will definitely be higher than those DFBs with straight gratings. Meanwhile, we think the grating line angle variation with respect to the pump stripe also enhances the spectral linewidth of our laser device. Both of these conjectures need to be investigated as future work.

2.8.3 Lateral and Longitudinal Chirps as Function of β

In previous sub-section, the FOM on the 2.5×4 mm device as function of C_X, C_Y and β on 2.5×4 mm device was presented. But FOM as the ratio of lateral chirp to longitudinal chirp for characterization of the chirped grating does not have full information of the quadratically chirped grating. Absolute values of lateral and longitudinal chirps still need to be calculated respectively as function of die tilting angle β in IL exposures, locations on die/device to know better about the hyperbolically

chirped grating for information such as tuning range and required data for simulation as well. In this sub-section, die azimuthal rotation angle α=6° is taken into account for the calculation of lateral/longitudinal chirp. Translational offsets C_X and C_Y are zero for all calculations as mentioned before.

Before lateral and longitudinal chirps of the grating are calculated, it is necessary to calculate and plot contours of the chirped grating period on the 10×10 mm die at several particular die tilting angles β to show the trend how this hyperbolic grating varies as β increases although die tilting angle has been determined to be 45°. The calculation result is plotted in Fig. 2.18. Obviously, grating period range and distribution on the 10×10 mm die experience abrupt changes as β increases, especially in the range of β from 0° to ∼10°. As β further increases, grating period contours tend to follow similar pattern over the die area but grating period and range still change very fast as indicated by the separation between contour curves in the figure.

As defined in section 2.5, lateral chirp can be taken as grating period variation along the grating line orientation. Unfortunately, as an example of this hyperbolic grating patterned on die at β=45°, the grating line orientation changes over the die as shown in Fig. 2.14. To simplify the process of quantifying lateral chirp, grating period variation along the straight line v=tan(96°)u which corresponds to equal optical path length interference fringe of the two spherical waves on die, is taken as reference for lateral chirp (For the coordinate system built for the die, please refer to sub-section 2.6.1.), assuming grating period variation along this straight line determines the lasing wavelengths that provide the information of device tuning range. The equation used to calculate lateral chirp in percentage is given below.

$$LateralChirp[\%] = \frac{\Lambda(u,v)_{Max} - \Lambda(u,v)_{min}}{\Lambda(u,v)_{min}}|_{v=tan(96^\circ)u} \times 100 \tag{2.22}$$

With the above method, the maximum and minimum of grating period along this line v=tan(96°)u on the 10×10 mm die and the corresponding lateral chirp as

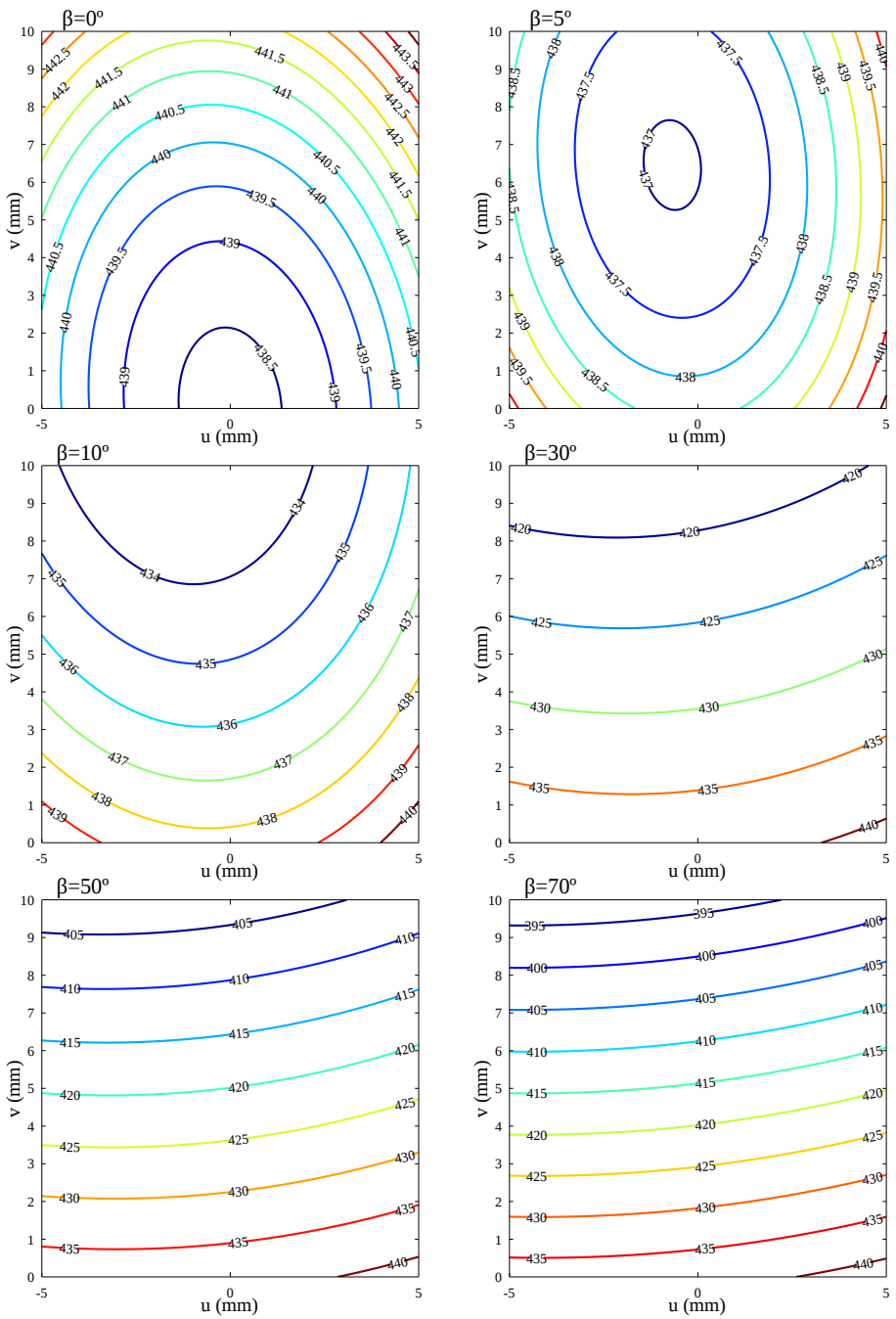

Figure 2.18: Contour of chirped grating period on 10×10 mm die as function of die tilting angle β, with azimuthal rotation angle α=6°, C_X=C_Y=0 mm, and C_Z=2 mm.

function of die tilting angle β are plotted in Fig. 2.19. Maximum grating period is plotted in red and the minimum is in blue. Apparently, lateral chirp plotted in green increases monotonically as the die tilting angle is increased beyond 3.9° (corresponding to the turning point on lateral chirp curve in the figure). Referring to Fig.2.18, when β increases from 0°, minimum grating period location shifts from origin along this straight line to the top end as β increases. And for β larger than 3.9° (not shown in the figure), the grating period along this straight line monotonically decreases from its maximum value, when leaving from origin towards the top end as indicated by Fig. 2.18 and 2.19. For the goal of maximizing lateral chirp to get wide laser tuning range, the die should be tilted with a as large as possible angle β, provided that longitudinal chirp is under control. So we now need to check how longitudinal chirp varies as die tilting angle changes.

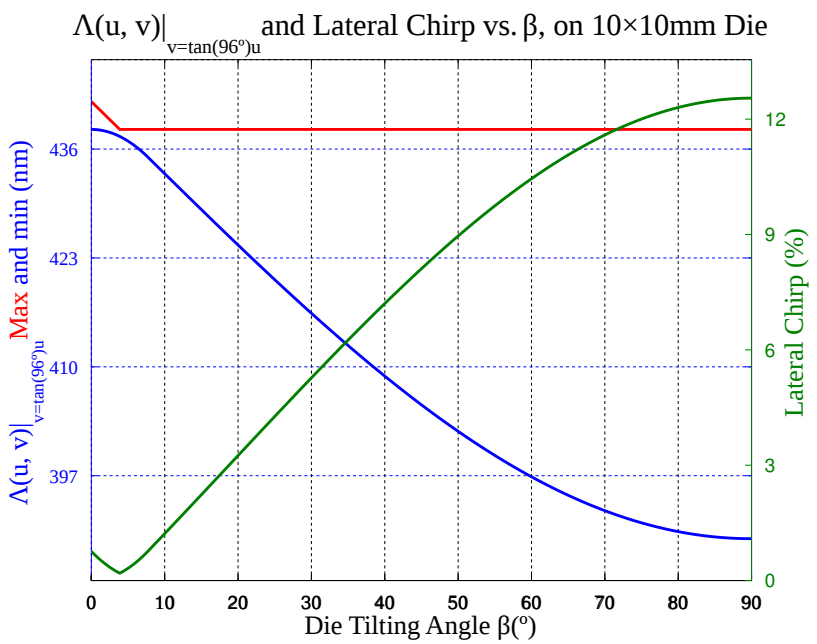

Figure 2.19: Grating period along line: $v = tan(96°)u$ and lateral chirp on 10×10 mm die as function of die tilting angle β, with α=6° and C_X=C_Y=0 mm, C_Z=2 mm.

Longitudinal chirp is calculated with the exactly same equation 2.22, except grat-

ing periods in the equation need to be replaced by their values along the pump stripe. Its calculation is more complicated because longitudinal chirp depends on multiple parameters, including die tilting angle β in IL patterning, pump stripe angle and lateral position on the die/device. In addition, longitudinal chirp also depends on the longitudinal dimension of the laser device and location of the device from where it is cleaved from the 10×10 mm die as well. All these different dependence will be presented in this sub-section. As for the pump stripe angle, only grating normal configuration (GNC) is presented in this dissertation, due to its advantage for F-P modes suppression. It is also the only configuration applied in device characterization presented in Chapter 3. To simplify the quantification of longitudinal chirp, pump stripe orientation and location is defined by straight line equation v=tan(6°)u+$v_{intercept}$ as shown in Fig. 2.20. Where $v_{intercept}$ is the intercept of this line on axis v which is necessary to account for different pump stripe lateral positions on the die/device as to be presented. This set of straight lines are perpendicular or approximately perpendicular to the grating line orientation (due to quadratical grating chirp) on die/device due to the azimuthal rotation in IL exposure.

With these introduced, longitudinal chirp along aforementioned straight lines on 10×10 mm die as function of die tilting angle is calculated and plotted in the Fig. 2.20. Five different $v_{intercept}$ values, 1, 3, 5, 7 and 9 mm, are plotted corresponding to 5 different pump stripe lateral positions as shown in lower right corner of the figure. In GNC, pump stripe represented by blue ribbon is tilted 6° with respect to u axis or the normal of the left/right facets of the die. In the Fig. 2.20, red curves stand for the maximum grating period along the pump stripe and blue curves are for the minimum grating period. Longitudinal chirp defined by equation 2.22 is plotted in green. At different $v_{intercept}$ values, longitudinal chirp shows sinusoidal-like pattern as die tilting angle β increases from 0° to 90° and monotonically decreases for die tilting angle β larger than 20° as shown in the figure. Value of longitudinal chirp increases with larger $v_{intercept}$ on the die (as pump stripe gets closer to the top edge

of the die). Over the entire 10×10 mm die and across the whole range of die tilting angle, longitudinal chirps stay below 0.7%, which is reasonably low. This conclusion is based on assumption that longitudinal chirp varies gradually as β and $v_{intercept}$ change and could be represented by these 5 different pump positions shown in the figure. The longitudinal chirp value for real DFB laser device with longitudinal dimension of 2.5 mm will be even less.

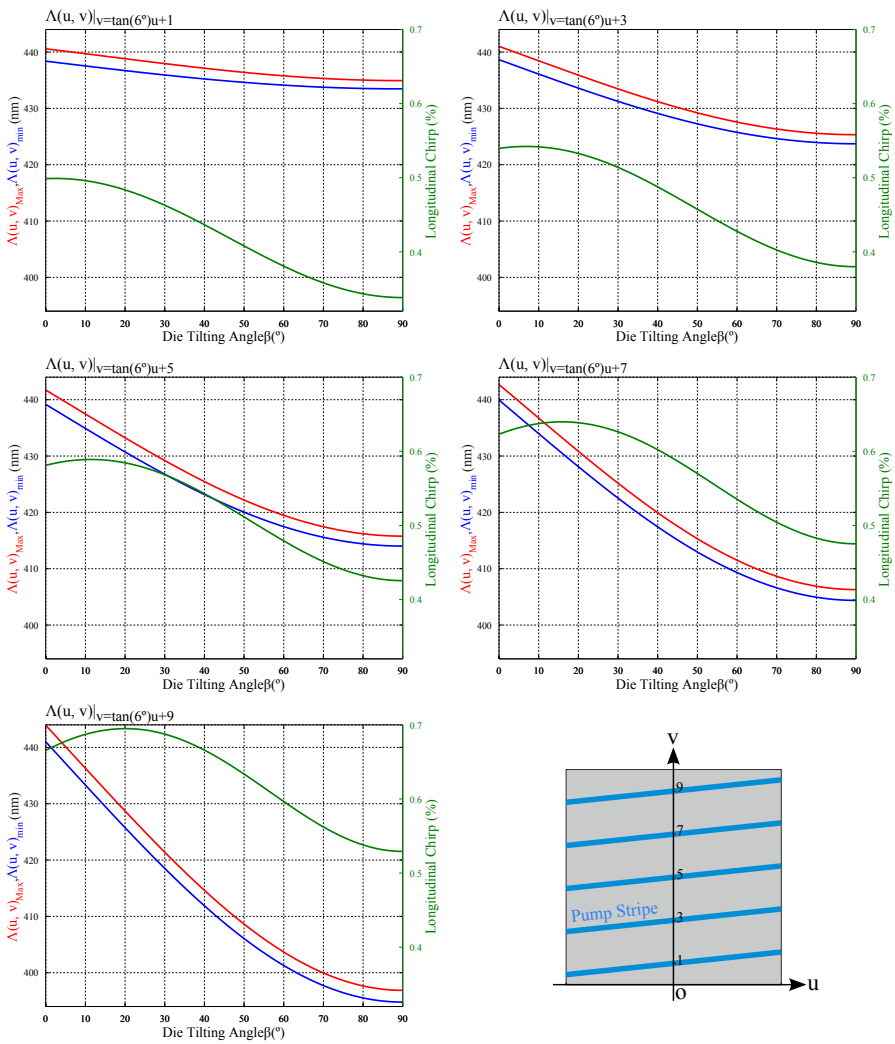

Figure 2.20: Longitudinal chirp along pump stripe in GNC as function of die tilting angle β, at different lateral positions given by $v_{intercept}$=1, 3, 5, 7, 9 mm, α=6°, C_X=C_Y=0 mm, and C_Z=2 mm.

Obviously, in the whole range of die tilting angle β, longitudinal chirp stays at reasonably low level, which again supports the conclusion that die should be tilted with an as large as possible angle β in IL to get large lateral chirp (by Fig. 2.19) to achieve large lateral chirp for wider tuning range on the DFB laser device. Practically, IL experimental setup is set at its maximum die tilting angle β=45° at present to maximize the device wavelength tuning range.

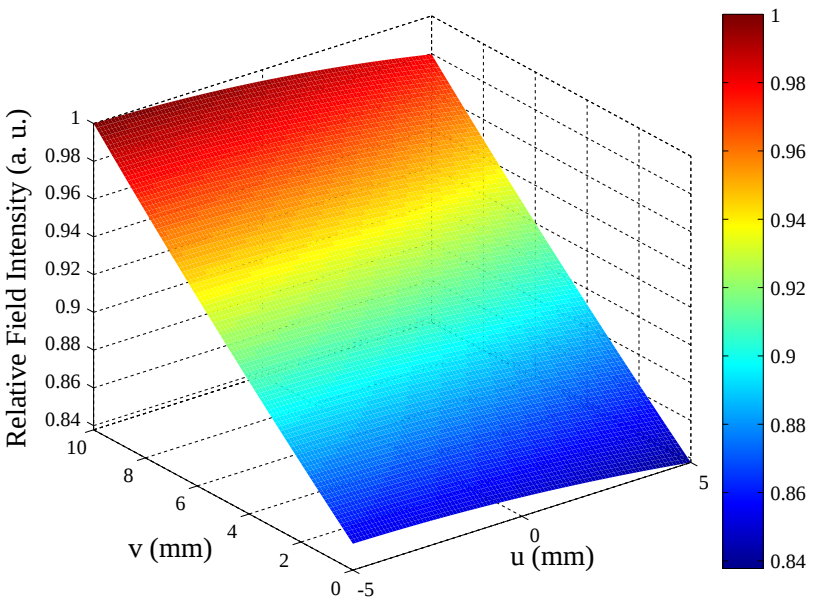

Figure 2.21: Relative Field Intensity on 10×10 mm die in IL patterning, with β=45°, α=6°, C_X=C_Y=0 mm and C_Z=2 mm

Another practical issue that needs to be considered is the nonuniform electric field intensity distribution in IL patterning from the bottom to the top of the die with large die titling angle, β in exposures. Large die tilting angle induces undesirable different grating duty cycles at different heights on die due to different exposure dose. That's the reason why in the IL experimental setup schematic Fig. 2.9, there is a so-called graded intensity filter, as represented by the orange rectangle placed in front of die. We don't have such a graded intensity filter at present. Fortunately, the relative electric field intensity difference over the 10×10 mm die is calculated to

be about 15% for die tilting angle β=45°, as shown Fig. 2.21. A dummy sample of about the same size of die was exposed on the IL experimental setup and then cleaved at different lateral positions for cross section view duty cycle exam under SEM to confirm that 45° tilting in IL without graded intensity filter is feasible.

Lateral/longitudinal chirp calculation with azimuthal rotation angle α=6° and field intensity distribution on 10×10 mm die presented above all support the conclusion reached before that the die tilting angle β in IL exposure should be set at 45°, maximum value at present. Together with FOM calculation results presented in previous sub-section, translational offset C_X and C_Y should be set at 0 mm.

2.8.4 Determine Device Cleaving Location on Die

Based on the criterion of maximizing FOM meanwhile keeping longitudinal chirp of grating low, optimized die positioning in IL exposure for real device fabrication has been determined to be as such, die tilting angle β=45° and translational offsets C_X=C_Y=0 mm. Another practical issue in the design and fabrication of our tunable DFB laser device is to find where the 2.5×4 mm device should be cleaved from the 10×10 mm die. Again, FOM is used to find the cleaving location of device from 10×10 mm die patterned with above positioning parameters in IL. FOM on a 2.5×4 mm device as function of device center location (u, v) over the 10×10 mm die is calculated for peak value of FOM, with the corresponding location gives the optimized device cleaving location. In this calculation, azimuthal rotation angle α is set to 0° to for simplicity, but the situation of actual grating with azimuthal angle of 6° should be similar. Calculation result of FOM is plotted in Fig. 2.22.

As shown in the Fig. 2.22, FOM gets its peak values along u-axis and is symmetric with respect to u-axis with α=0°. FOM maximum value of 127 is reached at v=0 mm and decreases to about 102 at v=10 mm. Obviously, the 2.5×4 mm device should be

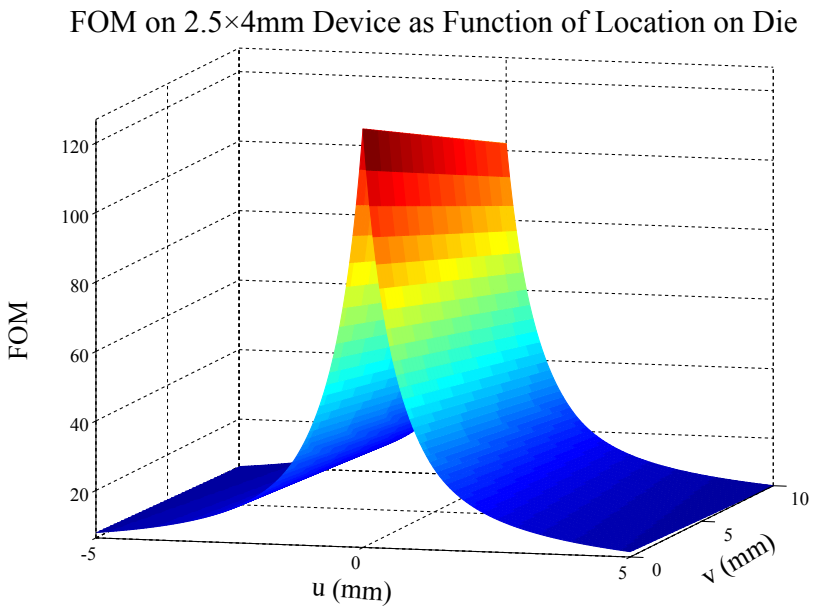

Figure 2.22: FOM on 2.5×4mm device as function of location on 10×10 mm die, with β=45°, α=0°, C_X=C_Y=0 mm, C_Z=2 mm.

cleaved from the bottom center or locations along and symmetric relative to v-axis on the die for high FOM. In actual chirped grating patterning on die with α=6° and azimuthal rotation center at origin in u-v plane, the above conclusion is still valid although FOM's distribution will be slight rotated.

In Fig. 2.23, the middle rectangular section on the die as potential cleaving section of 2.5×4 mm device is shown in part a). In this region, FOM of device stays in the range of [∼102, ∼127] as mentioned. Grating period along the straight line $v = tan(96°)u$ as function of v or lateral pump positions is shown in part b), which we used for prediction of the lasing wavelength of device as presented in Chapter 3. In part c), grating line angle in this potential region is shown, the grating tilting angle variation along the pump stripe with respect to it in GNC is in the range from ∼1.09° to ∼1.14°. Part d) gives the longitudinal chirp along the pump stripe in GNC on a 2.5 mm long (in longitudinal direction) device at different lateral pump

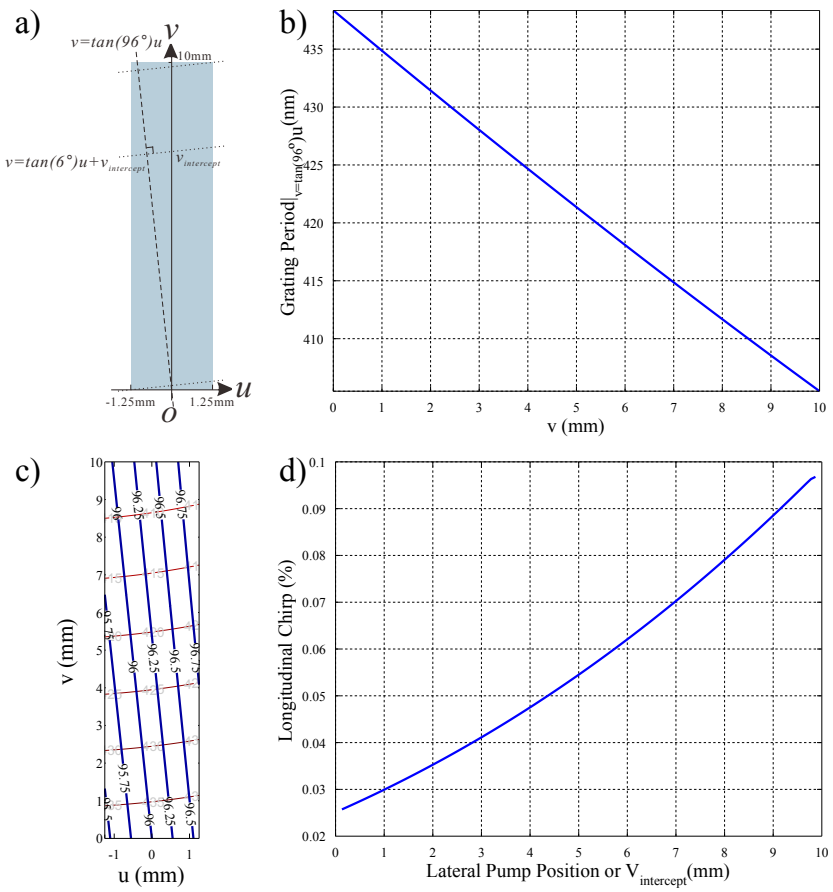

Figure 2.23: a)Diagram of potential region on die that 2.5×4 mm device could be cleaved from, b)Grating period along straight line $v = tan(96°)u$, c)Grating line angles in the region, d)Longitudinal chirp along pump stripe in GNC (along straight line, $v = tan(6°)u + v_{intercept}$) at different lateral pump positions.

positions. Longitudinal chirp stays below 0.1% at different pump positions as shown.

2.9 Device Fabrication

The fabrication of this tunable DFB laser device follows very standard procedures and include three major steps.

1. **Chirped Grating Patterning with IL** Using Interferometric lithography, hyperbolically chirped grating is patterned into the pre-coated photoresist (PR) layer on top of the 10×10 mm die.

2. **Grating Pattern Transfer with Dry Etch** Using inductively coupled plasma (ICP), chirped grating pattern is transferred into the to the top clad of the previously presented slab waveguide structure on the die.

3. **Laser Device Packaging** This step includes, die lapping, device cleaving and indium bonding to the heat-sink mount.

Each of these steps and the detailed process flow are presented in this section.

2.9.1 Process Flow

In this sub-section, the whole procedure of tunable DFB laser device fabrication is explained in detail, step by step. At the end, a schematic of the process flow, together with SEM photos of important processing steps will be also presented.

Step1. Die Clean The samples we get from AFRL is pre-diced into 10×10 mm dies. The very first step for processing a die is to clean it. Die is sequentially rinsed with acetone, methanol, and isopropanol for 10 to 15 seconds, then followed by a DI water rinse for about 10 seconds. Immediately afterwards, die is blow dry with N_2 gas. Then die is baked in contact mode, at 200 °C on hot plate for about 5 minutes for dehydration. After that, die is cooled down to room temperature for spin coating.

Step2. ARC Coating Anti-reflection coat (ARC) is required to avoid standing-wave pattern on the side walls of the grating patterned in photoresist (PR) and it helps PR adhesion as well. ARC has complex refractive index so is

absorptive at the IL wavelength. The mechanism that ARC works is based on processes of light absorption in it and also the destructive interference between the light reflected from the PR/ARC interface and the light transmitted back into PR layer through that interface from ARC layer after reflected by the substrate surface. With given substrate and PR and ARC, the thickness of the ARC layer needs to be correct for particular IL incident angles, which is controlled in the spin coating process. With well controlled ARC thickness, only IL incident light beams interfere and make patterns, without standing wave pattern showing on the side wall of PR pattern. The target thickness of ARC is calculated with our MathCAD program to be ∼70 nm, then spin coat RPM is looked up from the spin coat speed curve in the ARC data sheet, as shown in the following table. ARC spin coat recipe is shown in table 2.1.

ARC Model	iCON-7
Spin Coating Speed (rpm)	3500
Soft Bake Temperature (°C)	205
Soft Bake Mode	Vacuum
Soft Bake Time (Sec)	60
ARC Thickness (nm)	∼70

Table 2.1: Recipe for anti-reflection coat (ARC) spin coating

Step3. PR Coating Spin coat of PR is very similar to that for ARC and is done right after ARC coating. To determine the thickness of the PR layer, the etch rate in the following pattern transfer step and its etch selectivity vs. the substrate material need to be taken into account, because PR layer functions as dry etch mask in the fabrication of our tunable DFB laser device. Other than that, target grating period also needs to be considered because the aspect ratio (ratio between PR line height and width of patterned grating in PR) should not be too high to cause PR pattern collapse which will affect the pattern transfer into substrate. Based on the above considerations, SPR-505 from Shipley Inc.

is chosen for the IL grating pattern process which gives target thickness of ∼500 nm at speed of 3500 rpm in spin coat. PR spin coat recipe is shown in table 2.2.

Photoresist Model	SPR-505
Spin Coating Speed (rpm)	3500
Soft Bake Temperature (°C)	95
Soft Bake Mode	Vacuum
Soft Bake Time (Sec)	60
Target PR Thickness (nm)	∼500

Table 2.2: Recipe for photoresist spin coating

Step4. IL Patterning This step is actually combination of IL exposure, post exposure bake and development. IL experimental setup needs to be aligned before exposures, including the perpendicularity of the plano-convex lens to the Lloyd mirror, position relative to the lens of the vacuum chuck on which the die sits during exposure.

Dummy samples need to be exposed before real die, for incident angle adjustment, exposure dose and field uniformity examination. Initially, incident angle θ, die tilting angle β and die azimuthal rotation angle α are set with values as presented in section 2.6. But incident angle still needs to be finely adjusted according to the grating period measurement carried out at different positions on dummy samples on another experimental setup especially for grating period measurement, with He-Ne laser as light source. The whole angle adjustment process is recursive, till the target grating period range is reached as mentioned in section 2.6. Dummy samples are also checked under scanning SEM for exposure field uniformity and exposure dose to get target grating duty cycle of 40% in PR. 40% of PR duty cycle is determined according to the etch profile of grating pattern transfer process (introduced in the next step) to get 50% grating duty cycle in the top clad of the slab waveguide on the die. Exposure

dose is controlled by varying the exposure time for a given pulse energy and repetition rate. IL Patterning Recipe is shown in table 2.3.

The Laser used for the IL patterning in the fabrication of our DFB laser device is an Infinity 40-100 frequency tripled Nd:YAG laser from Coherent Inc. It is a Q-switched laser with output pulse duration of 3.0 ns, repetition rate adjustable in the range of 0.1 to 100 Hz. This laser has wavelength at 355 nm and maximum output power of about 16 W. Actual output power is controlled by setting the pulse energy and repetition rate. With a beam expander, laser raw beam is expanded to about 6 inches in diameter for large IL exposure area.

Laser	Infinity 40-100
Laser Wavelength (nm)	355
UV Pulse Energy (mJ)	100
UV Pulse Energy Density (mJ/cm^2)	∼3
Laser Pulse Repetition Rate (Hz)	60
Exposure Time (Sec)	3.5
Post Exposure Bake (PEB) Temperature (°C)	110
PEB Mode of Hot Plate	Contact
PEB Time (Sec)	60
Developer	MF-702 or MF-321
Develop Time (Sec)	60
Deionized (DI) Water Rinse Time (Sec)	∼10
Nitrogen (N_2) Blow Dry Time (Sec)	∼10
Photoresist (PR) Duty Cycle (%)	40

Table 2.3: Recipe for chirped grating IL patterning

Step5. Grating Pattern Transfer Chirped grating patterned in the last step is transferred through ARC layer then ∼500 nm into the top clad of the slab waveguide structure on the die, as mentioned in the previous section. Inductively coupled plasma etcher(ICP) from Plasma-Therm Inc. is used for this pattern transfer. Before real die is etched, GaSb dummy samples with same

chirped grating are etched for different durations, and then measured under SEM for the grating depth to get the information of clad etch rate, etch profile and time to etch through ARC layer. Etch time of 500 nm deep grating on real device is then calculated based on the etch rate acquired through linear fitting of the etch data got in GaSb dummy samples. Recipe for grating pattern transfer with ICP is shown in table 2.4.

ICP Recipe	Sandia1
Reactive Gas	BCl_3
Reactive Gas Flow (sccm)	32
He Flow for Cooling (sccm)	5.5
Pressure (mTorr)	3.5
ICP Power (W)	240
RF Power (W)	23
DC Bias (V)	115
Temperature (°C)	25
Etch Time (min)	8.5

Table 2.4: Recipe for grating pattern transfer

Step6. Residual PR/ARC Removal Once grating pattern has been transferred into the die or top clad of the slab waveguide structure, residual PR and ARC are removed with reactive ion etcher (RIE), PlasmaLab RIE-80 from Oxford Instrument Inc.. PR and ARC tend to be harder to remove after the grating pattern transfer process in ICP, so RIE etch time in the removal process is intentionally set to be long for a thorough removal with oxygen plasma, considering the etch gas O_2 etches PR and ARC but not GaSb top clad. Recipe for residual PR and ARC removal is shown in table 2.5.

Step7. Die Lapping In this step, substrate side die is thinned from ∼500 μm down to ∼150 μm for better heat dissipation in operation. Die is wax mounted on a stainless cylinder-shaped adapter on polisher jig with substrate side facing

Etch Gas Mixture	O_2
Gas Flow (sccm)	15
Etch Pressure (mTorr)	10
RF Power (% of 250W)	15
DC Bias Reading (V)	190
Etch Time (min)	15

Table 2.5: Recipe for residual PR and ARC removal

down for lapping. In the whole lapping process, lapping sheets with finer grit size need to be used to lower lapping speed and better surface smoothness as approaching the target thickness of 150 μm. Polisher used in this process is Ecomet-3 from Buehler Inc. Once lapping is finished, adapter with wax mounted die is soaked in acetone for about 12 hours to dissolve the wax for die liff-off.

Step8. Device Cleaving DFB laser device of 2.5×4 mm, in longitudinal and lateral directions respectively is cleaved from the middle region on die, as shown in Fig. 2.24. The reason we did not cleave the device from bottom center of the die is because grating pattern there seems not good enough. Wafer scriber, Karl Suss RA120M was used for device cleaving.

Before cleaving, protective tape is applied on grating side of the die. Then the die is scribed about 75 μm deep from the back side (substrate side), at pre-set locations. Once scribing is done, slight force is applied from a sharp stainless roller tip to the grating side of die, but behind the tape at the exact location of scribes to break the die along the crystal orientation to get flat facet. In this manner, device of aforementioned dimensions is cleaved from the die. Tape is then removed after cleaving is finished.

Step9. Device Bonding The final step for device fabrication is to indium bond the device onto a gold coated H-shaped heat sink mount. Practically, H-shaped

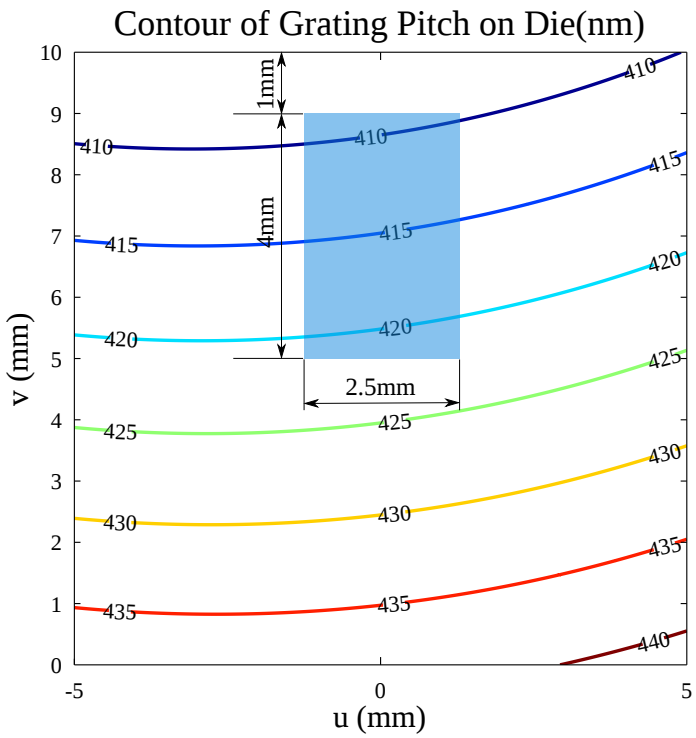

Figure 2.24: Dimensions and Location of DFB Device Cleaving

heat sink mount is first put on hot plate to heat up to a bit over 160°C, indium's melting point. Then a small piece of indium foil is laid along the right edge of the mount to melt. Once indium foil is melted, razor blade is used to spread out indium to form a thin film along the edge of mount. After that, DFB device is placed with epi-up on top of melted indium film along the mount edge, with front facet parallel but protruding a little bit from the mount edge. Slight pressure is applied on top of the device so shift it laterally slightly that device breaks the indium oxide layer formed in melting process and makes very good contact with indium. Finally, hot plate temperature is lowered to let indium solidify to finish bonding process. Special attention need to be paid not to let indium get onto the facets, especially the front facet of laser device.

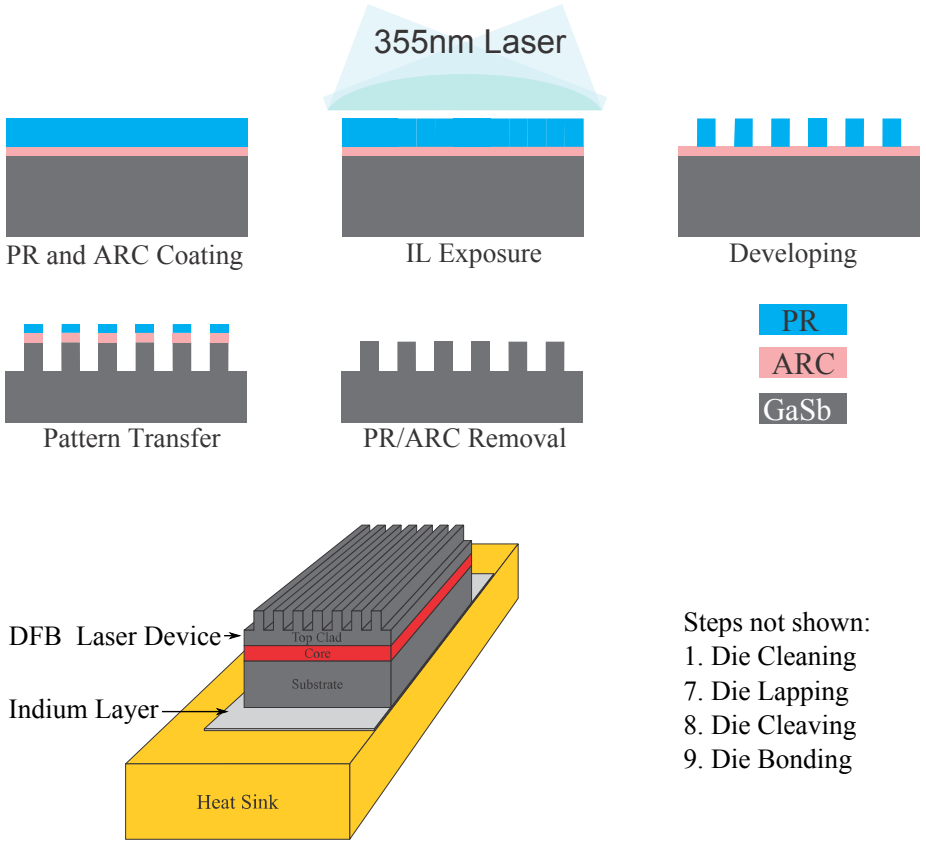

Figure 2.25: Processing flow chart of tunable DFB laser device

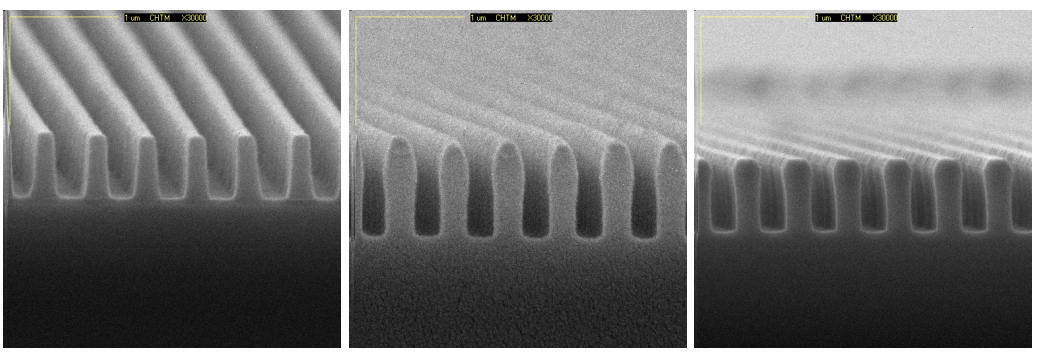

Figure 2.26: SEM pictures of dummy samples in cross-section view, (a) Grating in PR after development, (b) Grating pattern transfer into GaSb top clad after ICP etch, (c) Residual PR/ARC removal after RIE etch

The whole processing flow chart is shown in Fig. 2.25, in which most of the important processing steps are showed. Together with this picture, SEM pictures of three major process steps on dummy samples, namely PR grating patterns after development, grating pattern transfer into the top clad on the die and the residual PR and ARC removal are also shown in Fig. 2.26.

Steps 7 through **9** were done by Joe Sanchez at AFRL.

2.9.2 Device Specification

Although quite a number of devices have been fabricated, but most of them more or less have some defects that do not allow tuning across the whole lateral length of the device. The device that has the best performance is V9-18-9, from the No. 9 die of wafer V9-18. And its specifications are listed in the table below.

Device Number	V9-18-9
Lateral Dimension (mm)	4.0
Longitudinal Dimension (mm)	2.5
Device Thickness (μm)	$\sim$150
Grating Period Range (nm)	[408, 422]
Lateral Chirp (%)	$\sim$3.4
Longitudinal Chirp (%)	$\leq$0.85
Grating Duty Cycle (%)	$\sim$50
Grating Depth (nm)	$\sim$500
Mounting Direction	Epi-Up
Coupling Strength κL_g	2.2
Mode Confinement	0.42

Table 2.6: Tunable DFB laser device specification

2.10 Summary

In this chapter, our wavelength tuning approach to implement tunable DFB laser was first introduced, followed by design considerations, introduction of IL experimental setup, calculation of hyperbolic grating as function of location on the die, and finally the fabrication procedure. Discussion of the lateral and longitudinal chirps together with definition of FOM used to characterize this hyperbolic grating were applied to determine the die tilting angle, translational offsets and the location from where a 2.5×4 mm device should be cleaved from the 10×10 mm die.

As mentioned in the previous sections, the yield for good performance devices with wide tunable range is unacceptably low for some unknown reasons. I think the biggest issue is reflected and scattered light from different surfaces such as the lens back surface and the vacuum chuck surface which ruin the IL patterning. Although I have tried different methods including covering the exposed area on the vacuum chuck what holds 10×10 mm die in IL with rough surface absorbing tapes, none of them worked very well. In addition, using PR as etch mask to transfer pattern into top clad layer of die is also not ideal. Because the PR layer does not have high enough etch resistance and does not hold its rectangular profile during the whole etch time (turns to rectangular shape towards the end of etch process) which makes the etch profile of grating teeth not rectangular as expected, as shown in Fig. 2.26. This is solvable by using another harder etch mask such as a metal layer. Besides, experimental setup should also be modified to have larger die tilting angles to further increase the lateral chirp for wider tuning range.

In next chapter, the characterization of the fabricated device will be presented in detail.

Chapter 3

Device Characterization

In this chapter, the device characterization experimental setup will be first introduced. Then the best performance device, V9-18-9, characterization results will be presented. All characterizations, including output power, wavelength tunability tests and spectral measurements as well as spectroscopy demonstrations were all conducted at 80K in a liquid nitrogen Dewar, with pump stripe oriented in grating normal configuration (GNC). In the spectral linewidth measurement, both monochromator and Fabry-Perot interferometer were used for comparison reasons. The Fabry-Perot interferometer in fixed cavity length mode was used for spectroscopic demonstration of this tunable DFB laser device in the laboratory.

3.1 Characterization Experimental Setup

A schematic of the device characterization experimental setup is shown in Fig. 3.1. Different sections of the experimental setup will be presented separately.

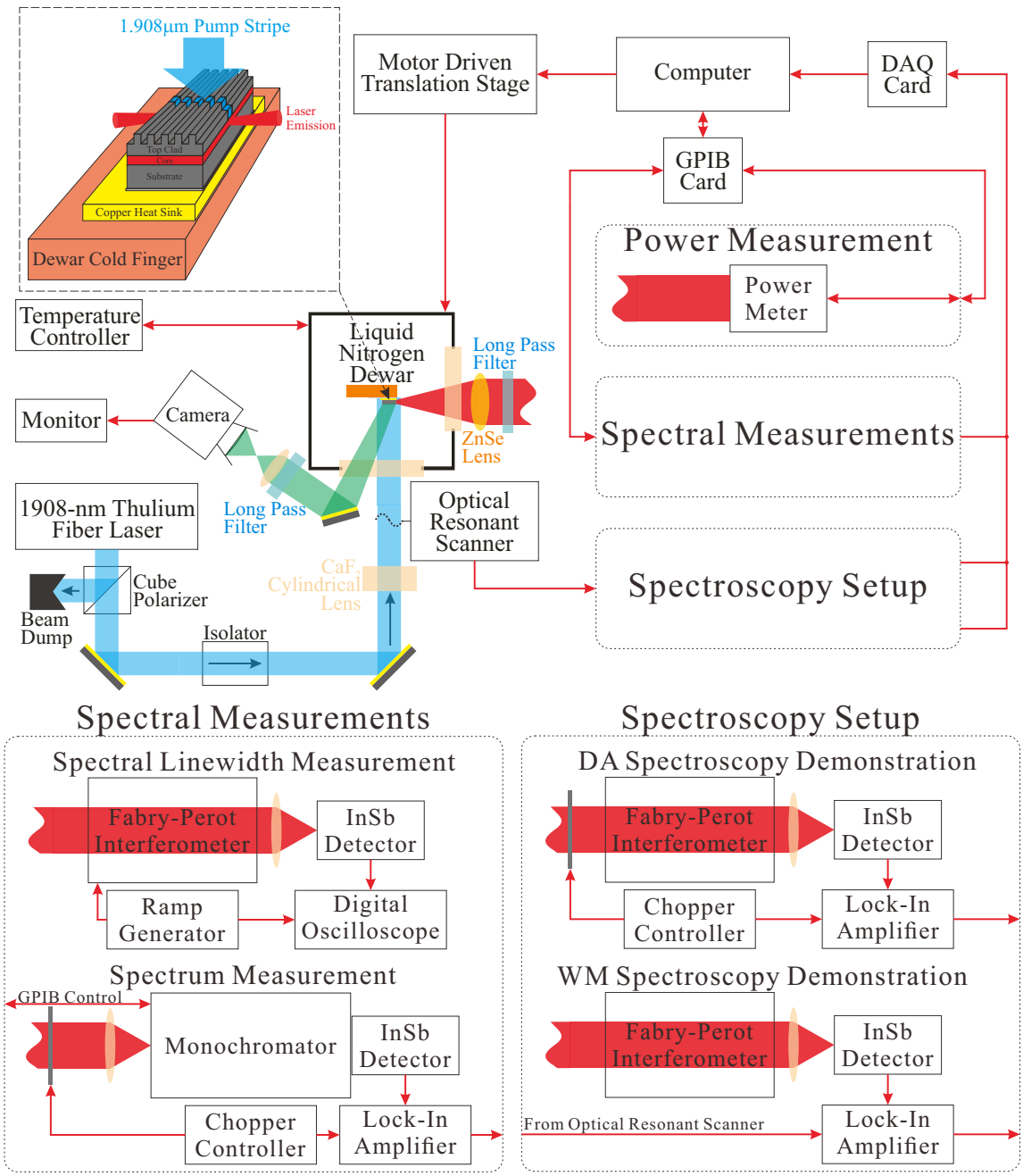

Figure 3.1: Schematics of tunable DFB laser characterization experimental setup

3.1.1 Optical Pump Section

As shown in the characterization experimental setup, the optical path of pump section is drawn in blue. The pump laser is a thulium fiber laser from IPG Photonics,

with specification shown in table 3.1. 1.908 μm light is coupled out through a fiber to the optics table. A polarizing beam splitter (labeled as Cube Polarizer in schematics) is mounted in front of pump laser fiber output, functioning as attenuator which can be rotated to let a fraction of pump the power through. The rest of pump power is bypassed by the splitter and goes to a beam dump. The transmitted pump beam is formed into a pump stripe with a cylindrical lens and projected normally onto the tunable DFB laser device mounted on the cold finger of liquid nitrogen (LN_2) Dewar through its front CaF_2 window as shown in the Fig. 3.1. All the optical surfaces except the the Dewar window in the pump beam path are AR coated for 1.908 μm light. To avoid damage to the pump laser output fiber from retro-reflection from the CaF_2 window and other optical surfaces as well as backward scattering from the laser device surface (Because its location is close to focus of pump stripe beam.), an isolator is placed in between the polarizing beam splitter and cylindrical lens as shown.

Laser Manufacturer	IPG Photonics
Model	TLR-20-1908-L
Operation Mode	CW
Maximum Output Power (W)	20
Output Wavlength (nm)	1908
Spectral Linewidth (nm)	1
Output Fiber Termination	Collimated
Beam Profile	Circular Gaussian
Beam Cross-section Diameter[$1/e^2$] (mm)	4.5
Beam Quality Factor M^2	$\sim$1.1

Table 3.1: Specification of pump laser in characterization

The aforementioned cylindrical lens to form the pump stripe is mounted on a rotation mount whose rotational axis is colinear with the pump beam so that the orientation of the pump stripe relative to the DFB laser device facets can be conveniently adjusted by rotating the mount. Although we have the flexibility of varying

the pump stripe angle, grating normal configuration (GNC) is the only configuration used in the device characterization due to its advantage of F-P mode suppression. Meanwhile, this rotation mount is placed on top of a translation stage moving along the pump beam direction so that distance between the cylindrical lens and device is adjustable. In this manner, pump stripe can be focused at different depths on the device from top clad through to somewhere into the substrate to investigate if the pump stripe beams waist location contributes to laser performance. The minimum pump stripe width can be evaluated by the following equation 3.1 [146].

$$\omega_{min} = \frac{\lambda f M^2}{\pi \omega_L} \tag{3.1}$$

Where λ is the pump laser wavelength; f is the focal lens of the lens; ω_L is the collimated pump beam radius at lens; and M^2 is the beam quality factor of pump laser. The cylindrical lens chosen for this setup is SCX-25.4-30.5. Actual pump stripe width is measured to be in the range of 70 to 100 μm. In the wavelength modulation spectroscopy demonstration to be presented later in this chapter, original cylindrical lens was substituted with one with longer focal length so that an optical resonant scanner could be placed in between the Dewar front window and the cylindrical lens to modulate the pump stripe position on device. Because the cylindrical lens for this purpose is not as powerful as the original one to focus the pump stripe as tight, a Galilean telescope beam expander (not shown in the schematic) was inserted in front of cylindrical lens that expands the pump beam diameter for $\sim$2X so as to get as tight pump stripe with this less powerful cylindrical lens.

Throughout the entire process of device characterization, the pump laser was operated at a fixed output power value for stability considerations. Pump power is adjusted by rotating the polarizing beam splitter at different angles relative to the pump laser polarization direction. The transmitted pump power through the polarizing beam splitter is given by following equation.

$$P_{out} = P_{in} \times \cos^2 \phi \tag{3.2}$$

Where P_{out} and P_{in} are the transmitted and input power (pump laser output power) respectively and ϕ is the angle between the polarization directions of polarizing beam splitter and pump laser. In calibration of actual pump power on the laser device, pump power was measured first behind the cylindrical lens with a power meter as a function of the polarizing beam splitter angle at a given laser output power. Then, reflection from the CaF_2 Dewar window as well as the ratio between device longitudinal dimension (2.5 mm) vs. full pump stripe length need to be taken into account to calculate the actual pump power applied on the laser device. The reflection from the CaF_2 is calculated to be about 0.9 and factor for the effective pump stripe length is about 0.5.

3.1.2 Temperature Control Section

This section consists of a liquid nitrogen Dewar, its thermostat and vacuum pump station. The Dewar is model DET-2154-SLN manufactured by Cryo Industries, Inc. And the thermostat is Cryo Con 32B Temperature Controller. The pump station used in the characterization is made by Alcatel Inc.. The temperature control system can adjust operation temperature from 77 K to higher temperature for investigation about the thermal effect on the device's performance although all the characterization results presented in this chapter was acquired at about 80 K.

3.1.3 Monitoring Section

The monitoring system includes an infra-red (IR) camera with specification listed in table 3.2, lenses and mirrors required to image the spontaneous emission excited by pump stripe, from the laser device surface onto the camera sensor. It's very helpful to display the real time pump stripe orientation relative to the device facets and pump stripe width (due to focusing) as well, meanwhile the image can also be

used to tell the pump stripe lateral position on the device when it is close to the upper/lower edge of the device. The optical path of the monitoring section is drawn in green in the Fig. 3.1. A long pass filter with cut-off wavelength of 3 μm could be used to block the scattered pump laser light in case it damage the IR camera sensor. Considering the germanium lens with the camera has coating of 3-14 μm, use of this long pass filter is optional.

Image acquired by the IR camera can be displayed either on a TV monitor or on computer screen with an image acquisition card installed. Most of time in this research work, TV monitor was used to display the relative pump stripe angle and positions.

Specification of the IR camera used in this experimental setup is shown in table 3.2.

Manufacturer	Electro Physics
Model	PV32L2Z
Sensor Type	Uncooled BST
Resolution (Pixels)	320×240
Pixel Dimension (μm)	30
Pixel Pitch (μm)	148.5
Spectral Response (μm)	0.6-20
Lens	35mm/F1.0 Germanium Lens
Lens Coating Range (μm)	3-14
Video Output Protocol	30Hz NTSC

Table 3.2: Specification of infra-red camera in device characterization

3.1.4 Dewar Translation Stage Section

This section is required for laser wavelength tuning purpose, represented by the box Step Motor Driven Translation Stage as shown in Fig. 3.1. As mentioned in Chapter

2, pump stripe needs to be translated laterally to different positions on the device for the chirped grating to select different lasing wavelengths. Inside the Dewar the DFB laser device is mounted vertically on the cold finger, with its facets or the lateral direction perpendicular to the optics table. In wavelength tuning characterization, the Dewar instead of pump stripe was shifted up or down (with the pump stripe kept fixed) which is equivalent to shifting the pump stripe down or up at different positions on the device. In this manner, the emission collection optics of the laser device do not need to be readjusted since pump stripe is kept fixed. With that explained, the platform on which LN_2 Dewar sits is bracket mounted on a vertically mounted translation stage able to be shifted up or down to scan across the whole lateral dimension (4mm) of the laser device. The original manual translation stage was converted to be driven by a step motor with a transmission box for fine scan step and heavy load considerations. The step motor is controlled using a National Instrument (NI) data acquisition (DAQ) card with Labview program running on computer so that the Dewar/device shifting can be synchronized to data acquisition for wavelength tuning test and spectroscopy demonstration. Gear ratio setting of the transmission box is 1:50 for all the different characterizations.

3.1.5 Emission Section

The tunable DFB laser emission section includes mainly the emission collection lens, power meter, monochromator, Fabry-Perot (F-P) interferometer and mirrors/lenses required to steer the output beam and couple it into the above mentioned apparatuses. The optical patch of DFB laser emission is drawn in red as shown in Fig. 3.1.

Emission of the DFB laser device goes through the CaF_2 side window of the Dewar and then is collected and collimated with a ZnSe lens, before it is coupled

to apparatuses for all different types of measurements. ZnSe instead of CaF_2 lens was chosen mainly because ZnSe has higher refractive index and can be made into more powerful lens to achieve higher F numbers/numerical aperture for higher solid angle coverage that efficiently collects highly divergent laser emission from the device. Since GNC is the only pump stripe orientation applied in device characterizations, the laser emission is not normal to the device facets. Actual exit angle for laser emission in our characterization setup is about 23.5° relative to the facet normal, tilting up as shown in the Fig. 2.10. Accordingly, ZnSe collection lens needs to be tilted normal to the laser emission and is put on a translation stage traveling in line with the laser emission direction to conveniently adjust its distance to the emission spot on facet for collimation. This whole assembly is then mounted on X-Y-Z translation stage to align the collection lens in line with device emission.

Because a lock-in amplifier is used to increase the signal-noise ratio (SNR) in device characterizations, chopper needs to be placed in either pump or laser emission beam. To avoid the alternatively turning on/off induced thermal instability of the DFB laser device, chopper is placed in the laser emission beam and the chopper controller generates the reference frequency signal for lock-in amplifier and the external trigger signal for oscilloscope.

A long pass filter with 3 μm cut-off wavelength is placed in the laser emission beam to filter out the scattering and the leaked pump laser light through facets.

In output power measurement, laser emission is steered to Labmaster power meter with a thermal-pile sensor head LM-10, manufactured and calibrated by Coherent Inc.. The same sensor was used for both the pump power and tunable DFB laser device output power measurements. Analog value of power is digitized on the meter and read out to the computer through GPIB port with Labview program.

For spectrum acquisition, laser emission is coupled into a monochromator with a

F number matched CaF_2 lens. Monochromator (specification shown in table 3.3) is programmable through GPIB port for different settings, including grating selection, slit width, scan range and scan step size, etc.. Most of time, grating No.2 with 150 grooves/mm was used in laser device spectral acquisition. An InSb detector IS-040 manufactured by Electro-Optics Inc. is placed behind monochromator exit slit to detect the output light. Detector signal, through its pre-amplifier, is then sent to lock-in amplifier SRS510 by Stanford Research Inc. for measurements. Meanwhile, detector signal is also displayed on oscilloscope for help in optics alignment to maximize the signal. Considering this model of lock-in amplifier is fairly old that has built-in ADC with only 8 digits resolution, analog signal was read out and digitized with a NI DAQ card USB-6259 and upload to computer. Labview programs were written for spectral acquisition.

Manufacturer	Spectral Products		
Model	DK480 1/2 Meter		
In/Out Slit Width Range (μm)	10-3000		
Controlling Interface	GPIB		
Grating Dimension (mm^2)	68×68		
Grating Density (Grooves/mm)	300	150	75
Peak Wavelength (μm)	2.5	4	8
Spectral Coverage (μm)	1.5-6	2.5-9	5-15
Wavelength Accuracy (nm)	1.2	2.4	4.8
Resolution[10μm Slit] (nm)	0.24	0.48	1
Minimum Scan Step (nm)	0.04	0.08	0.16

Table 3.3: Specification of the monochromator in characterization

For comparison, a F-P interferometer is also used for spectral linewidth measurement. This sub-system consists of F-P interferometer(with specification shown in table 3.4) and its ramp generator, RC-44 from Burleigh, a InSb detector J10D-M204-R01M-60 from Judson Technologies and a digital oscilloscope. Due to the reason that we could not synchronize between the F-P interferometer scanning and lock-in ampli-

fier, digital oscilloscope was used to display and record the waveforms from detector placed behind F-P interferometer for transmitted signal, which was later analyzed and processed on computer. Together with the laser output wavelength acquired with monochromator, spectral linewidth in wavelength can be calculated once F-P transmission signal waveforms from detector is acquired.

In addition, the interferometer in a fixed-cavity-length mode was also used as spectral filter (to simulate a molecule or target gas) in the spectroscopy demonstrations to be presented in this chapter. In spectroscopy demonstration, the InSb detector placed behind F-P interferometer records the transmittance signal as the Tunable DFB laser device is tuned. The detector signal is sent to the lock-in amplifier. And the analog output signal from lock-in amplifier is then digitized by DAQ card and uploaded to computer with particular Labview programs for display and processing.

Laser Manufacturer	Burleigh
Model	RC-110
Max Mirror Separation (mm)	150
Mirror Diameter (inch)	2
Mirror Coating Range (μm)	3-5
Mirror Reflectivity [3$\sim$ 5μm Range] (%)	$\geq$ 98.5
Set Cavity Length in This Experiment (μm)	$\sim$364
Free Spectral Range [FSR] (GHz)	$\sim$412
Finesse	$\sim$208
Minimal Resolution (GHz)	FSR/Finesse$\approx$1.9808
Piezo Scanning Range (μm)	$\sim$1.5

Table 3.4: Specification of the Fabry-Perot interferometer and the mirror set in characterization

3.1.6 Electronics System

This section mainly includes instruments such as pre-amplifiers for detectors, lock-in amplifier, USB-GPIB data acquisition (DAQ) card , PCI-GPIB interface conversion cards as well as the computer to run the Labview programs.

3.2 Output Power

Single facet output power of device V9-18-9s as function of pump power was measured at different pump positions and three of those are selected to represent the whole DFB laser device. This device is 4 mm long in the lateral direction as introduced earlier, so pump stripe position y=0.2 mm, 1.8mm and 3.7 mm, correspond bottom end, near the middle and top end of the device respectively. Single facet output power at above three different pump positions are plotted in Fig. 3.2. The pump stripe focusing and emission collections were optimized particularly for these three different positions to compensate the situation that the tunable DFB laser device might not have been mounted perfectly vertical or Dewar does not shift perfectly vertically. Both pump and emission power results are corrected by taking account factors such as effective pump stripe length and reflections from different optics surfaces such as windows and lenses.

As shown in the Fig. 3.2, typical threshold for this device is in the range from 0.5 to 1 W and its output power increases linearly as pump power increases. Slope efficiency of single facet efficiency is about 14%, similar to previous device fabricated by former group member, Liang Xue. (Fig. 2.16 [128]). At all the three different positions, output power does not show signs of roll-over indicating output power measurement result is limited by the available pump power. Particularly at pump position y=1.8 mm, this device has a single facet output power of about 830 mW as

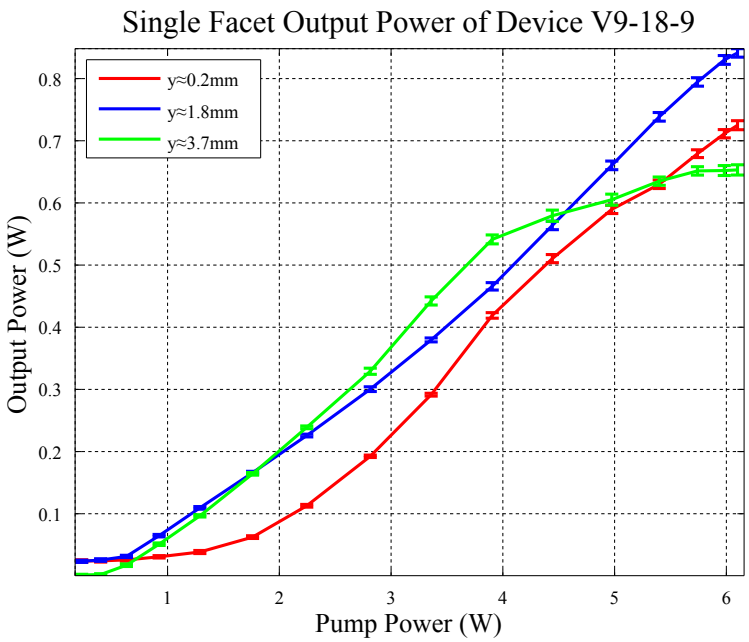

Figure 3.2: Single facet output power of device v9-18-9, at three different pump stripe position on the device

shown in the blue curve in the figure. At the same time, this figure also shows some problems of the device such as, device has very soft turn on at pump position y=0.2 mm, and output power at y=3.7 mm does not strictly follow a linear pattern. We believe all these are due to fabrication non-uniformity issues and partially because these two pump positions are close to the lateral ends of the device.

At all the three pump positions across the whole range of pump power, device lases in single longitudinal mode. As an instance of device emission spectra, the spectra at about 3.5×threshold pump level at these three pump positions are shown in Fig. 3.3, color coded with the output power curves shown in Fig. 3.2 for different pump positions. At this particular pump power, the side mode suppression ratio (SMSR) at all three different pump positions on the device is over 30 dB.

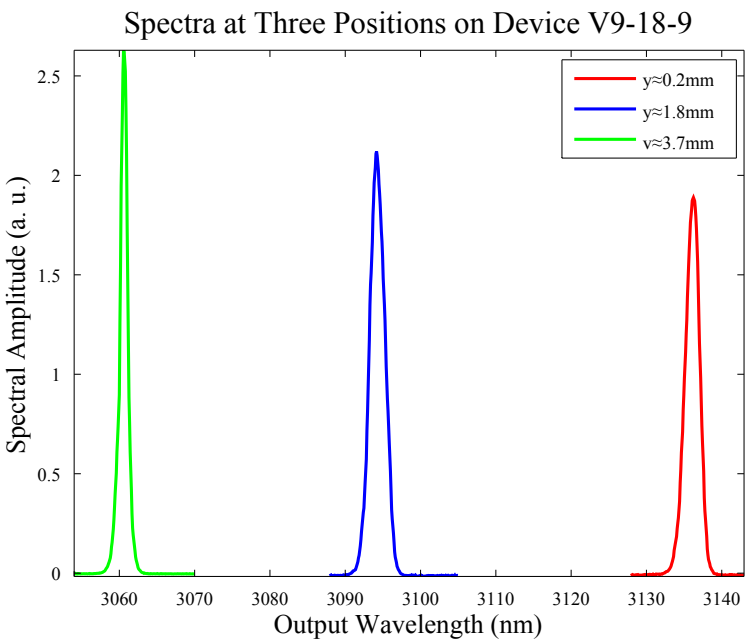

Figure 3.3: Spectra of the three different pump stripe positions where single facet output power measurement was conducted, at ∼3.5×threshold

3.3 Wavelength Tuning

In device wavelength tuning test, LN_2 Dewar was shifted up or down so that pump stripe was equivalently translated laterally at different positions on the tunable laser device to select different emission wavelengths. The spectrum at each position was acquired with monochromator, InSb detector and lock-in amplifier as shown in the schematic of the characterization experimental setup, Fig. 3.1. Once scanning across the whole lateral dimension of device was complete, all spectral data digitized and saved in the computer were processed together. At present, we don't have capability to compensate the non-vertical device mounting or Dewar translation in this characterization experimental setup. As a temporary solution to guarantee that pump stripe is properly focused at least for most parts on the device during this wavelength tuning scanning, some arbitrary pump position at about middle of the

device was picked for pump stripe focusing and emission collection optimization before the device tunability test was conducted. This approach turned out to be fine, although spectral linewidth data at some pump positions might become wider due to non-optimized pump stripe focusing. Spectral linewidth as function of pump stripe focusing will be presented later in this chapter.

During this test, pump power was set at about 2.5×threshold of the device V9-18-9. Because spectrum acquisition using monochromator and lock-amplifier across the whole wavelength range with high resolution is a relatively slow process, only 55 equally separated different pump positions are measured across the whole lateral length of this device to assure stable operation considering the LN_2 fill time, in case LN_2 evaporates completely that the operation temperature control is lost. The monochromator setting for the spectrum acquisition in this test includes, in/out slit width at 10 μm, scanning range 90 nm from 3050 nm to 3140 nm, and scan step at 0.3 nm. The time constant for lock-in amplifier is set at 300 ms, and integration time is 1 s at each particular wavelength selected by monochromator. Step motor rotates 1100 steps in between two neighboring pump positions, corresponding to about 685 μm shift of pump stripe and wavelength tuning step of about 1.46 nm. The total lateral travel to scan across the 2.5×4 mm device in GNC is 4-2.5×tan6° ≈3.74 mm.

The spectra at these 55 different pump positions on device at about 2.5×threshold pump level is plotted in Fig. 3.4.

In order to plot the wavelength tuning curve of device V9-18-9, spectral peak wavelengths at all pump positions were extracted from these 55 raw spectra and plotted in blue curve in Fig. 3.5. As shown in the figure, this device V9-18-9 has tunable range of about 80 nm from 3056 to 3136 nm. Quadratic fitting of the device emission is also plotted overlaid on top of the raw data in red. The fitted curve agrees very well with measurement except in the part close to the lower-end of the device at y≈0.35 mm, where there is a slight jump of ∼2.4 nm between

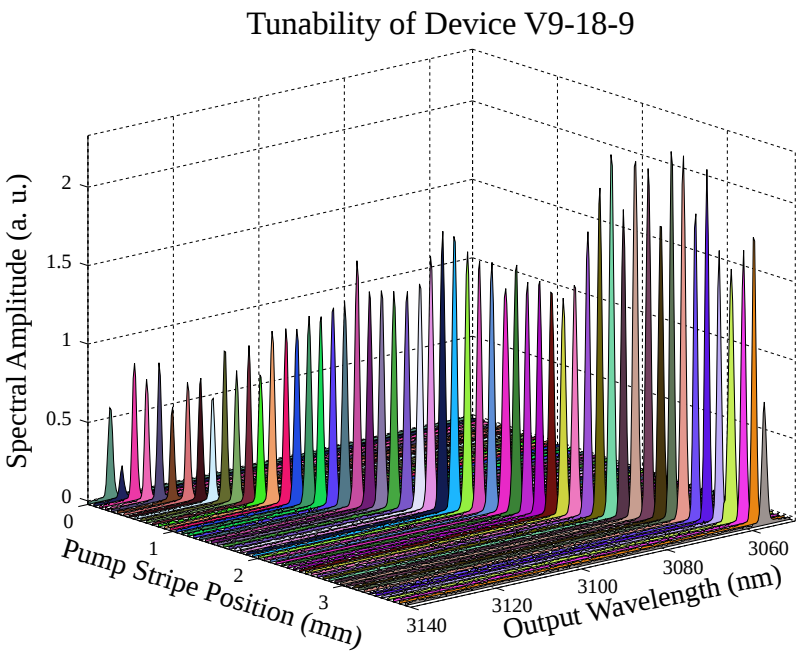

Figure 3.4: Emission spectra of device V9-18-9, at different pump positions on the device, at ∼2.5×threshold

the neighboring spectral peaks. Similar wavelength tuning scan has been repeated several times trying to reproduce the jump because we doubt if it's from degenerated DFB modes [10, 142] since our device is an index-coupled type. But we could not reproduce it, which indicates that this device does not have DFB mode degeneracy issue and can be tuned continuously.

In Chapter 2, grating period range along straight line $v = \tan(96°)u$ on the 10×10 mm die has been used to predict the tuning range of the DFB device. To check if this approach is valid, grating period on the die along this line and the corresponding Bragg wavelength given by $\lambda_{Bragg} = 2n_{Eff}\Lambda|_{v=\tan(96°)u}$ are plotted in Fig. 3.6. The blue rectangle in the figure gives the range of grating period on the device V9-18-9 cleaved from location shown in the Fig. 2.24. With n_{Eff}=3.73, Bragg wavelength calculated gives very close value of tuning range that matches the actual laser output wavelength measured shown in red dots very well. Although, effective refractive index

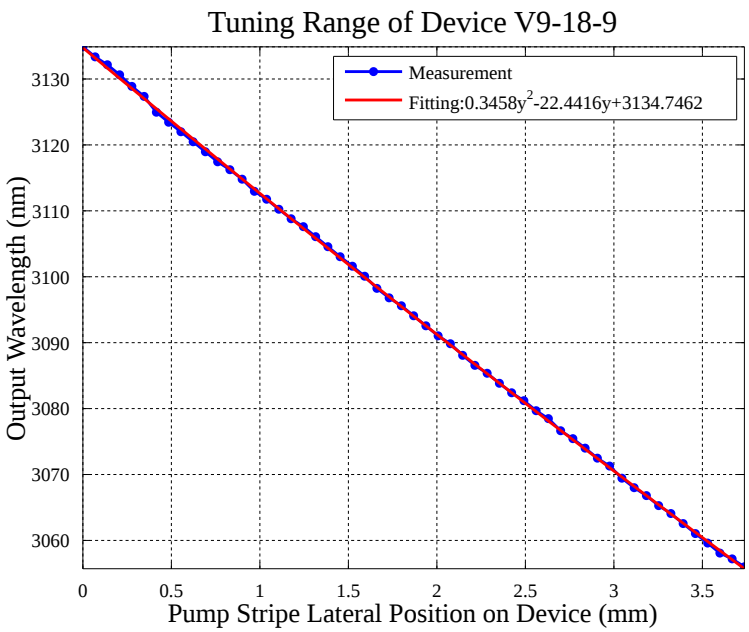

Figure 3.5: Wavelength tuning range of device V9-18-9, at ∼2.5×threshold

is relatively smaller than the calculation result in slab waveguide modeling, it's fair to conclude that the grating period along straight line $v = \tan(96°)u$ can be used to predict the tuning range of the DFB laser device.

3.3.1 Wavelength Fine Tuning

In order to demonstrate that the device V9-18-9 can be tuned continuously, instead of hopping from one F-P mode to another or between degenerate DFB modes, fine wavelength tuning test was conducted on a small sections on this device. Basically, it's same as the full device tunability test just presented, but with a finer tuning step. Interval between neighboring pump stripe positions in this test was about 93.4 μm, with step motor rotating 150 steps. By wavelength tuning fitting curve shown in the Fig. 3.5, this pump stripe position shift corresponds to wavelength tuning step of approximately 0.2 nm. This wavelength tuning step was determined by the

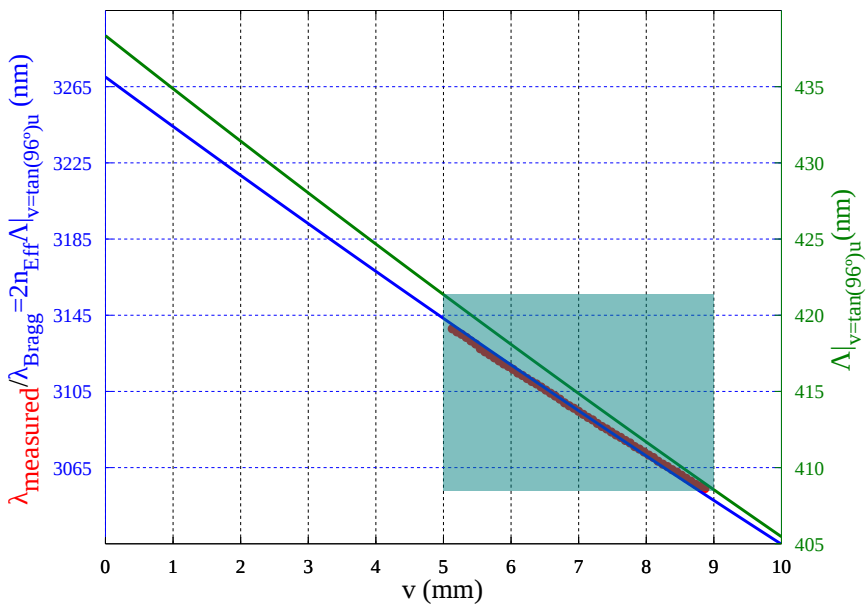

Figure 3.6: Grating period along straight line $v = tan(96°)u$ on the 10×10 mm die, V9-18-9 and DFB laser device grating period range (within the blue rectangle) as well as expected Bragg wavelength with n_{Eff}=3.73. The measured lasing wavelength on the device is shown in red dots as well.

monochromator's highest resolution of 0.24 nm, with the 300 grooves/mm grating and 10 μm slit width set in this measurement. If the device was still affected by facet feedback from the facets, then the free spectral range (FSR) of F-P modes given by equation FSR=$\lambda^2/2n_gL$ is in the range of 0.49 to 0.51 nm across the wavelength tuning range of device V9-18-9, considering n_g is about 3.825 and L, as cavity length is 2.5/cos6° mm for grating normal configuration. So if there are no wavelength jumps on the order of F-P FSR in the wavelength tuning curve, it is safe to conclude that the device is not affected by F-P modes. Other than F-P modes, degenerate DFB modes common for index-coupled type of DFB laser also may affect the single longitudinal lasing and continuous tuning of laser that need to be tested.

The wavelength fine tuning measurement results are plotted in Fig. 3.7. Total tuning range of about 10 nm was achieved in 51 steps, and the laser output wave-

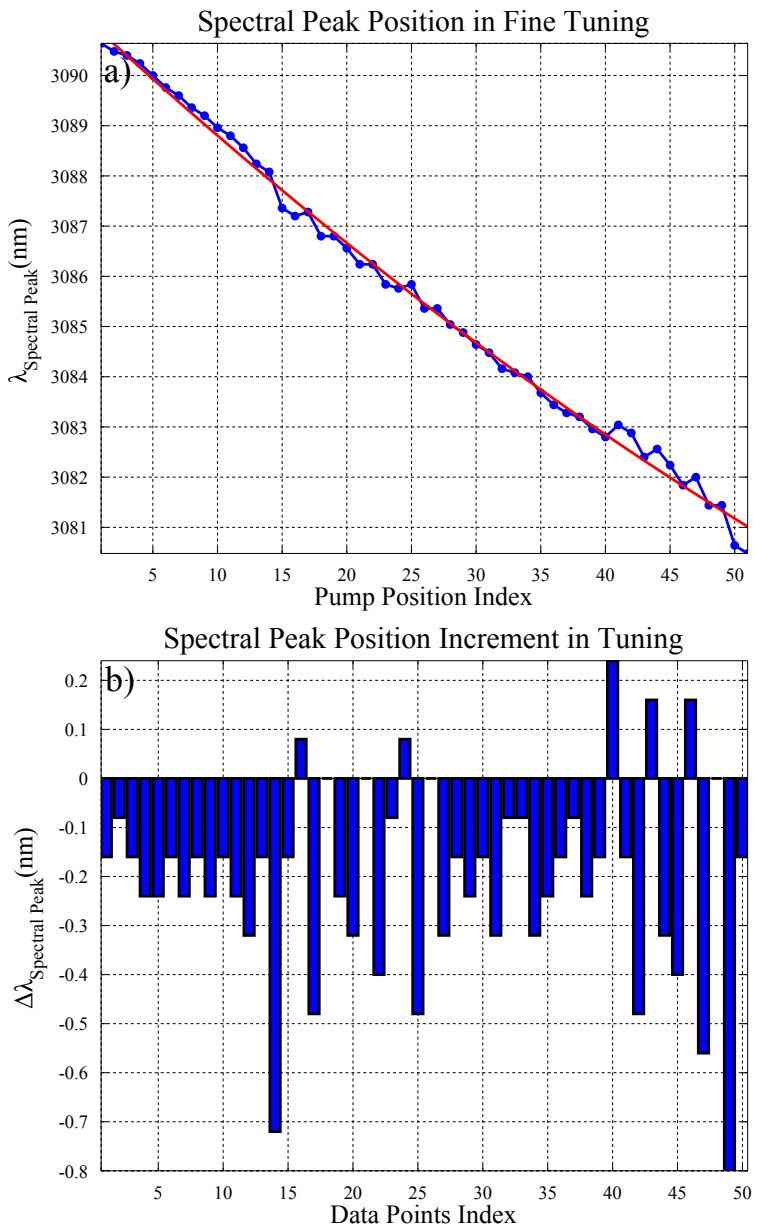

Figure 3.7: Fine wavelength tuning test of device V9-18-9, at arbitrary section on the device. a) Device output wavelength measurement results in blue curve overlaid with quadratic curve fitting plotted in red. b) Device output wavelength increment in the fine tuning test.

length extracted from spectra acquired with monochromator at all different pump positions are plotted in blue in part a). Quadratic fitting curve is also shown as well

in red. To quantify wavelength tuning step, the increment of laser output wavelength in this fine tuning is plotted in part b). Unfortunately, there are still few places that output wavelength increment in tuning is larger or on the order of F-P mode FSR given above. But it's still not conclusive to say that device V9-18-9 is affected by F-P modes, considering that the algorithm of simply taking maximum amplitude in spectrum as output wavelength without accounting for the signal amplitude fluctuation induced by unstable laser output power as well as actual monochromator wavelength scan step of 0.08 and 0.12 nm alternatively. We did not observe any spectrum with two degenerated spectral peaks appearing at the same time. The largest wavelength increment in this fine tuning test is 0.8nm. If it corresponds to stop band width $\Delta\lambda$, then by equation 3.3 [12, 147], the coupling strength of device V9-18-9 is only $\sim$0.662 which is far from our calculated value. It's more likely that these steps are the results of lateral modes.

$$\Delta\lambda = \frac{\kappa\lambda^2}{\pi} \tag{3.3}$$

So we can probably rule out the existence of degenerate DFB modes, at least in this fine tuning test range. The most convincing method to prove whether laser device is continuously tunable is to tune the device's emission wavelength to scan across some well known absorption spectrum of a target gas. If there are stair-like steps or random jumps showing in the absorption spectrum amplitude as seen in methane absorption spectroscopy demonstration conducted by previous group member, Liang Xue [128], then laser is not tuning continuously. Because we could not find gas with absorption spectral lines in the device wavelength tuning range, F-P Interferometer in fix cavity length mode was used as an artificial gas or spectral filter to demonstrate this device V9-18-9 is continuously tunable, as to be presented in section 3.5.

3.4 Spectral Linewidth

When the device wavelength tunability test was conducted, full width half maximum (FWHM) or spectral linewidth of the spectra acquired at all pump positions was extracted and is plotted in Fig. 3.8. The blue curve in the figure is raw data and the red one is for FWHM value of Gaussian lineshape fitting of all the spectra at different pump positions. The discrepancy between them is mainly because the wavelength increment of monochromator was not small enough that the original spectral lineshape turned into form of folded lines and caused error in FWHM. Finer spectral scan was not possible because it is too time consuming and LN_2 would evaporate completely before full scan across device is finished. Generally speaking, device V9-18-9 has a typical spectral linewidth of about 1.2 nm reflected by raw data. If a pump stripe focusing control mechanism to optimize pump stripe focusing at each pump position on the device while wavelength tuning was implemented, we should be able to get narrower spectral linewidth. This value of spectral linewidth is quite broad for a DFB laser device. The wide spectral linewidth result could be attributed to following reasons. First, pump stripe width on the order of 70-100 μm makes the this DFB laser a broad area laser which commonly suffers from multi-lateral mode issues [148]. Second, as calculated with assumption that pump stripe is about 100 μm width, longitudinal chirp along the pump stripe as well as lateral chirp across the pump stripe on the order of 0.05% to 0.09% on device both contribute to the broadening of the laser spectral linewidth. Third, as mentioned in the previous reason, the longitudinal chirp makes only partial length of grating along the pump stripe contribute to the selection of lasing wavelength which leads to an effectively shorter cavity length with smaller coupling strength, κL that results in broader device spectral linewidth compared with straight grating case. Fourth, due to wide pump stripe width and especially under high pump power condition, lateral spatial hole burning (LSHB) and filamentation related to linewidth enhancement

factor (LEF) tend to appear in broad area lasers to broaden the spectral linewidth [121, 125, 149–151]. Fifth, linewidth enhancement factor (LEF) itself in type-II lasers with values from 0.7 to 5 also directly contributes to the lasing spectrum broadening [119, 152–154].

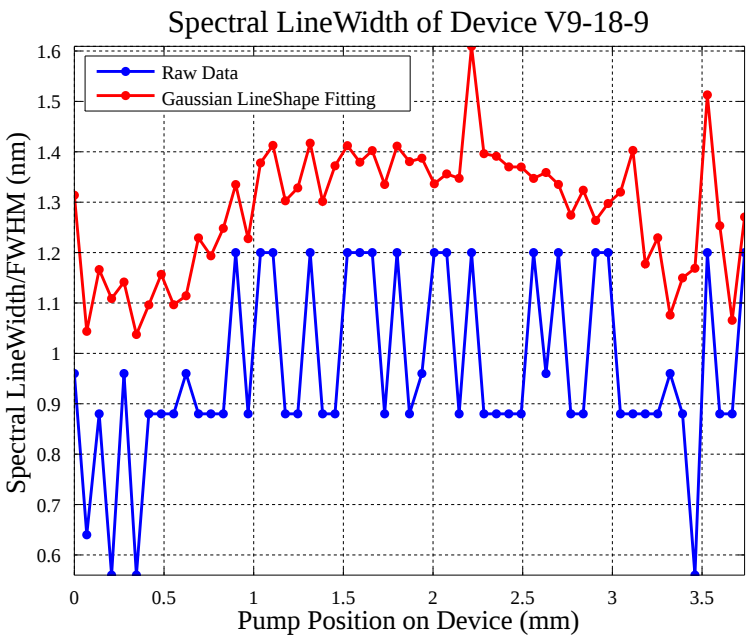

Figure 3.8: Spectral linewith of device v9-18-9, at ∼2.5×threshold

For this research work, modeling of the longitudinal and lateral chirps' effect on device characteristic such as spectral linewidth is one of the future works that should be carried out.

3.4.1 Spectral Linewidth vs. Pump Stripe Focusing

Spectral linewidth of device V9-18-9 as function of pump stripe focusing was also investigated due to lack of compensation for any non-verticality in the mounting of device or Dewar translation on the stage in experimental setup as mentioned earlier.

At different arbitrary pump positions on the device, spectra of device emission were measured with different pump stripe focusing knob settings. The spectral linewidth was extracted together with signal amplitude from these acquired spectra. The reason both were extracted is in hope that possible correlation between them could offer some guidance for pump stripe focusing adjustments in characterization. Result at one of these pump positions that gives output wavelength at about 3069 nm is plotted in Fig. 3.10.

In this measurement, both monochromator and F-P interferometer were used for cross check reasons. When measuring the spectral linewidth with F-P interferometer, its cavity length has to be measured first to get FSR which later is required to calculate the device V9-18-9's spectral linewidth. To calculate spectral linewidth in wavelength domain with F-P interferometer for comparison with monochromator results, spectral peak wavelength is also required. In the spectral linewidth as function of pump stripe focusing investigation, spectral peak wavelength was measured by monochromator.

To measure the cavity length of F-P interferometer, device V9-18-9's emission wavelength was first tuned to acquire the transmittance spectrum of F-P interferometer in fixed cavity mode (ramp generator off), as shown in Fig.3.11 presented in the next section. Then pump stripe positions corresponding to these transmittance peaks were re-visited by reversing the step motor driven stage accordingly so the transmittance peaks' wavelengths could be measured with monochromator. Once all the F-P interferometer transmittance peaks' wavelengths were acquired, F-P interferometer's cavity length L_{FP} was calculated and fitted with following equation.

$$L_{FP} = (m+i)\frac{\lambda_i}{2} \quad m, i \in I \tag{3.4}$$

Where λ_i is the wavelength of the ith transmittance spectral peak. m is solved using different transmittance peak wavelengths and through curve fitting. For present F-P interferometer cavity length, only 5 complete transmittance peaks were acquired

for full device wavelength tunable range, as shown in the Fig. 3.11. With above method, the cavity length is calculated to be about 364 μm, corresponding FSR of about 4.12×10^{11} Hz. There are some system errors and uncertainties in the peaks' wavelengths due to reasons such as translation stage back lash that the F-P interferometer cavity length determination might not be very accurate. But it is the best we could get and spectral linewidth in wavelength calculated with F-P interferometer transmittance data agrees well with the FWHM measured by monochromator as shown in the Fig. 3.10.

After the F-P interferometer cavity length was determined, it was switched to scanning mode (ramp generator on) for transmittance measurement to acquire spectral linewidth of DFB laser device emission. The DFB laser emission, after passing through F-P interferometer, was registered by InSb detector placed behind it. This transmittance signal was also displayed and saved on digital oscilloscope for processing later. A typical F-P interferometer transmittance signal waveform displayed on oscilloscope for a given DFB device emission wavelength (In this case, it is 3069 nm.) is shown in Fig. 3.9. The two wider peaks in the middle are transmittance signal when F-P interferometer's cavity length equal to multiple of emission wavelength in the scanning and the two narrow ones on the sides are from retracing. Limited by maximum travel of the piezoelectric transducer actuators in F-P interferometer, only two transmittance peaks could be resolved. This waveform on oscilloscope is basically a linear spatial-temporal mapping between the F-P interferometer cavity length (with light frequency information embedded) and transmittance signal that the light spectral linewidth information can be derived by measuring the signals' temporal width. L_1 is the temporal FWHM of the transmittance peak signal and L_2 is the temporal distance between the neighboring transmittance peaks, which correspond respectively to the frequency spectral linewidth of device V9-18-9 output at this particular wavelength and the FSR of F-P interferometer. Assuming F-P interferometer scans linearly, then ratio of L_1/L_2 gives the spectral linewidth of the

device in term of F-P interferometer FSR in frequency domain. With known wavelength λ by monochromator, the spectral linewidth in wavelength domain can be easily calculated with following equation.

$$\Delta\lambda = \frac{\lambda^2}{2nL_{FP}}\frac{L_1}{L_2} \tag{3.5}$$

n is the group refractive index of the medium in the F-P interferometer cavity, which is 1 for air in our case.

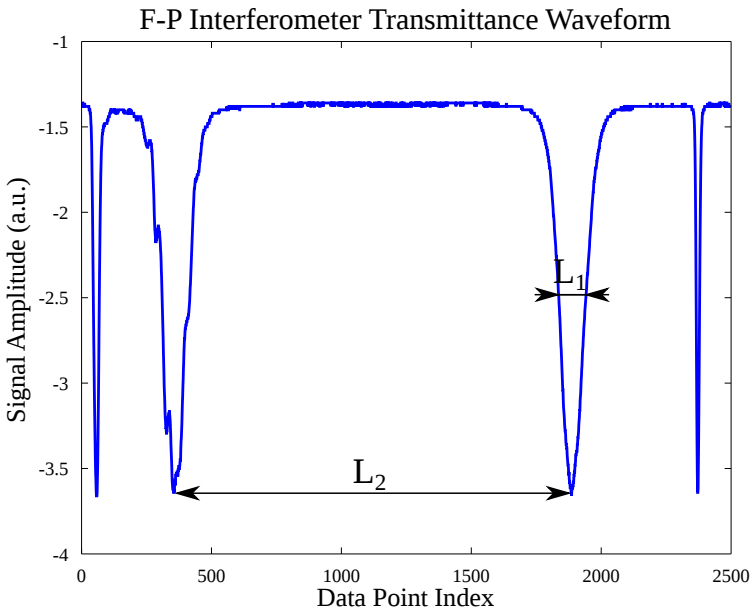

Figure 3.9: F-P interferometer transmittance signal waveform on oscilloscope for device V9-18-9 spectral linewidth measurement

Back to the measurement of DFB laser device spectral linewidth as function of pump stripe beam focusing, the result is plotted in the Fig. 3.10. The top plot is the spectral amplitude of the measured at emission wavelength 3069 nm as function of pump stripe focusing. The bottom plot is the FWHM/spectral linewidth results as function of pump stripe focusing from both monochromator (red) and F-P interferometer (blue). Obviously, there is correlation between signal amplitude and spectral linewidth as pump stripe focusing varies as shown. To the left of the valley

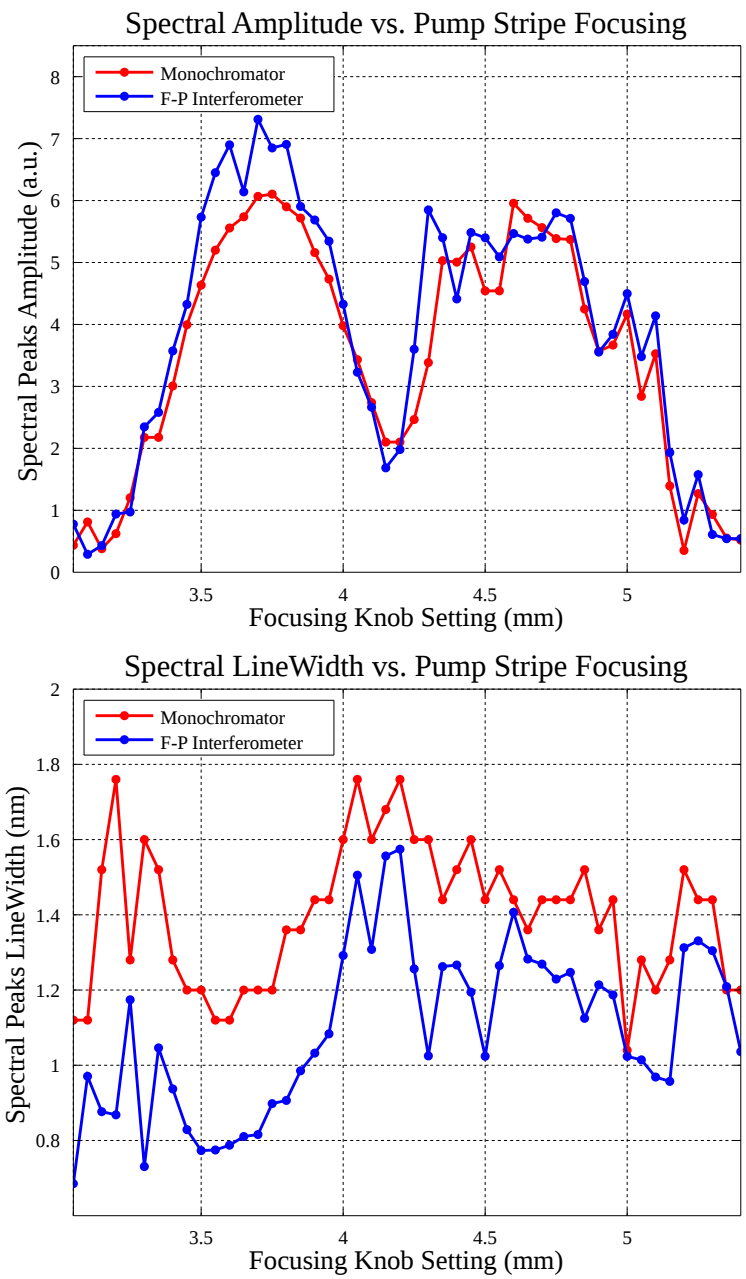

Figure 3.10: Device V9-18-9 spectral linewidth vs. pump stripe focusing, at arbitrary pump position

in the signal amplitude plot on top, corresponding to focusing deeper into the device, signal amplitude changes gradually and smoothly as pump stripe focusing varies. On

the contrary, signal amplitude fluctuates strongly as focusing changes on the other side of the valley, corresponding to the cases pump stripe is focused shallower on the device. On both sides of the valley, signal amplitude has comparable amplitude. Referring to the spectral linewidth plot at the bottom, aligned with pump focusing setting where the signal amplitude valley locates, device has the widest spectral linewidth. When focusing is deep into the device, the spectral linewidth is much narrower than for the shallow focus case. In addition, the spectral linewidth also fluctuates strongly as amplitude does for the case focusing is shallow. The valley in the signal amplitude probably corresponds to the situation when the beam waist of pump stripe is exactly in the core layer of the slab waveguide. At the moment, we conjecture that the reason device V9-18-9 behaves as such might be due to the mode matching between the modes excitation by pump and waveguide eigen mode (Slab waveguide was design to support fundamental mode only.).We speculate that this behavior should be dependent on pump stripe focusing tightness and the cylindrical lens focal length as well. But no experiments were conducted for investigation to prove this.

Due to the above results, without pump stripe focusing optimization mechanism to compensate for the non-orthogonal translation and focusing adjustment, pump stripe focusing was adjusted to maximize the signal amplitude and on the stable side of focusing to acquire a narrower spectral linewidth in all the different characterization tests. As part of future work, a pump stripe focusing optimization mechanism should be developed.

3.5 Spectroscopy Demonstration

Spectroscopy demonstration with device V9-18-9 was conducted by measuring the F-P interferometer transmittance spectrum while tuning the device across its full

tunable range, with F-P interferometer in fixed cavity length mode functioning as artificial target gas because no proper target gas could be found for our laser device. In addition, wavelength modulation spectroscopy was also demonstrated with an optical resonance scanner which modulates the device V9-18-9's emission wavelength simultaneously when its wavelength was being tuned. Strictly speaking, F-P interferometer might not be appropriate to function as artificial target gas because the transmittance signal measured in this manner is the convolution of the laser device emission spectrum and the eigen transmission function of F-P interferometer, but not uniquely from gas absorption. F-P interferometer with ideal cavity mirrors has eigen transmission function looks like unit height delta-function comb in frequency or wavelength domain which is nonlinear. With not high enough reflectivity cavity mirrors, these delta-function like transmission peaks drop amplitude and get broad. For the wavelength slightly off the eigen transmission peaks of F-P interferometer, only small portion of the laser device emission can pass though the interferometer and gets detected by detector placed behind it due to nonlinear transmission attenuation from F-P interferometer. For wavelengths far from eigen transmittance peaks, they are completely blocked by F-P interferometer. If the whole wavelength tuning range needs to be tested, F-P interferometer cavity length has to be set at a series of different values (Not done in this research work) consequently to let its eigen transmission peaks cover all different emission wavelengths from the tunable laser device. As mentioned above, the transmitted light power also gets modulated by the nonlinear F-P interferometer transmission function that might be suppressed at some wavelengths that makes some originally obvious amplitude differences not as obvious. Nonetheless, F-P interferometer could be used to demonstrate tunable laser device's potential application in spectroscopy.

3.5.1 Direct Absorption Spectroscopy Demonstration with F-P Interferometer

In this demonstration, device V9-18-9 pumped at about 2.5×threshold was tuned across its full tunable range with tuning step of ∼0.067 nm by pump stripe position shift of ∼31.13 μm, corresponding to step-motor rotating 50 steps. Transmitted laser light is recorded by InSb detector placed behind F-P interferometer, then amplified with lock-in amplifier, finally digitized with DAQ card and uploaded to computer. F-P interferometer transmittance spectrum acquired is shown in Fig. 3.11. Mathematically, it is the convolution product from device emission spectra in tuning and the eigen transmission function of F-P interferometer as mentioned earlier. The FWHM of these transmittance peaks are wider than expected probably due to the non-optimized pump stripe focusing explained before. Peak 6 is incomplete because pump stripe in tuning was at the very end of device.

Considering the mirror reflectance of F-P interferometer is ≥98.5% in 3 to 5 μm range, the finesse given by equation 3.6 is ∼208.

$$F \approx \frac{\pi\sqrt{4R/(1-R)^2}}{2} = \frac{\pi R^{1/2}}{1-R} \tag{3.6}$$

And the spectral resolution in wavelength domain is about 0.063 to 0.065 nm across the whole device tuning range, given by equation 3.7.

$$\Delta\lambda = \frac{\lambda(1-R)}{m\pi\sqrt{R}} \tag{3.7}$$

Where λ is the laser emission wavelength and m is the order of interference which is in the range of [233, 237] corresponding to the first 5 spectral peaks in the Fig. 3.11, calculated when F-P interferometer cavity length was solved. The wavelength tuning step and the resolution of F-P interferometer is about the same which means all the peaks in transmittance from actual wavelength tuning should be resolvable by F-P interferometer. In other words, any mode hopping or wavelength change

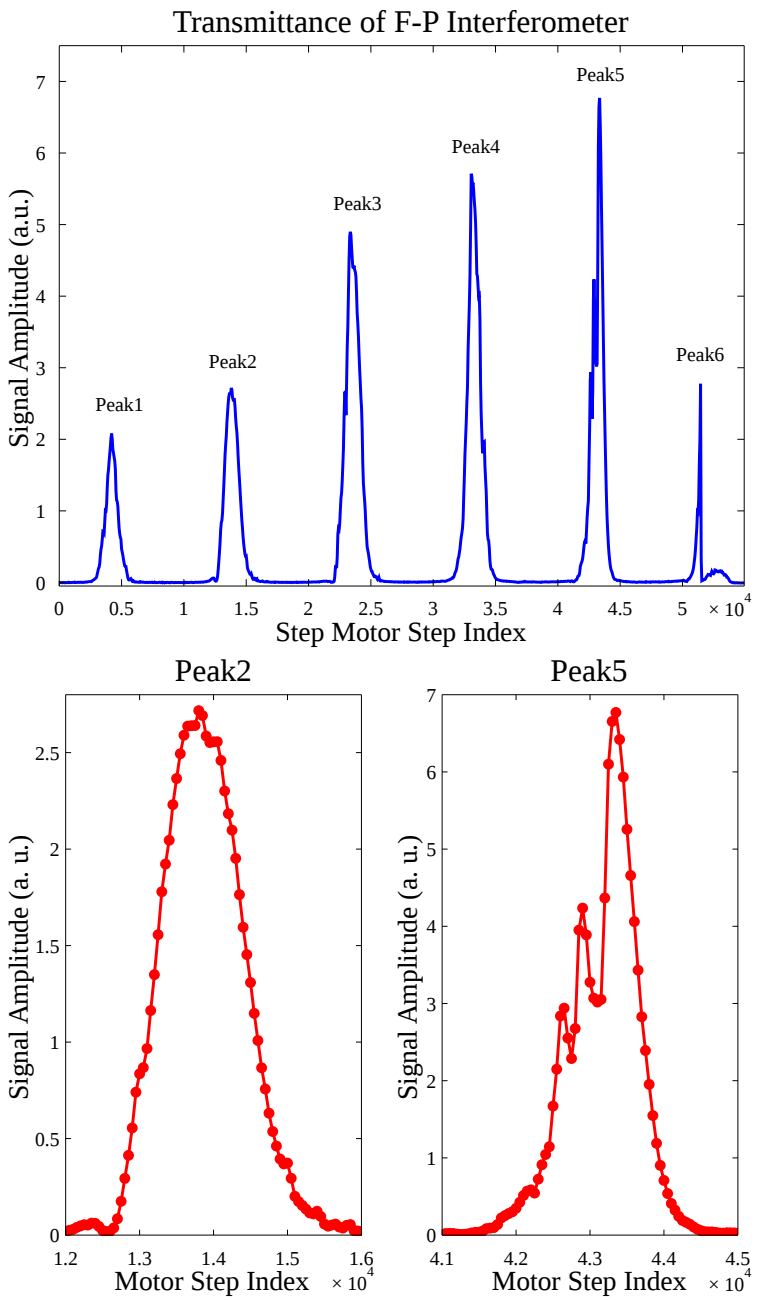

Figure 3.11: F-P interferometer transmittance in wavelength tuning range test of device V9-18-9

greater than F-P interferometer spectral resolution or amplitude fluctuations in the laser device emission should be detectable in the F-P interferometer transmittance

measurement. Due to the nonlinear transmission function of F-P interferometer, some of the transmittance signal variation may be not as prominent as they originally are. As examples of transmission discontinuity corresponding to the possible mode variation or hopping, two different cases are shown in subplots for peak2 and peak5 at the bottom of the Fig. 3.11. First one is the small hump at the left foot of peak2 and the second one is the the sub-peaks on the left shoulder of Peak5. We can exclude the probability of F-P mode hopping in these two cases. Considering the typical spectral linewidth of 1.2 nm for the device V9-18-9 measured by monochromator at this pump level as shown in the Fig. 3.8, and F-P mode spacing on the order of 0.5 nm should cause more pronounced transmission fluctuation on the shoulder of transmission peaks. Especially for the narrow sub-peaks on shoulder of transmittance peak5, whose width correspond to 3 or 4 tuning steps in this test (corresponding to 0.2 to 0.25 nm wavelength tuning), they to some extent indirectly confirm that the laser spectral linewidth should not be very wide. We can also almost exclude the existence of degenerate DFB modes. Assuming the coupling strength of device V9-18-9 is 1, half of the calculated value introduced in Chapter 2, then DFB stop band width by equation 3.3 at wavelength 3070 nm is about 1.2 nm. And if that's the case, the transmittance signal fluctuation would be larger than what is shown in plot of transmittance peak5. Other fluctuations or roughness in the transmittance spectrum of F-P interferometer are more likely due to the device emission amplitude fluctuations or lateral modes considering the pump stripe is as wide as 70 to 100 μm which is tens of order of lasing wavelength. Another reason might cause sub-peaks to appear on the should of peak5 could be fabrication defects.

We conclude that multi-longitudinal mode lasing is not shown on this device V9-18-9. The sub-peaks showing on the shoulder in peak5 and peak3, 4 are real and are likely due to the existing lateral modes in laser, fabrication defects or probably unstable device output power. Device output power fluctuation issue could be solved with a beam split to get reference output portion not passing through F-P interfer-

ometer to be detected with another detector then cancel out the fluctuation in data processing.

3.5.2 Wavelength Modulation Spectroscopy Demonstration

3.5.2.1 Wavelength and Frequency Modulation Spectroscopy

Wavelength/frequency modulation spectroscopy (WMS/FMS) has been implemented since 1970's due to its two main advantages over direct absorption (DA). Firstly, instead of measuring the signal amplitude directly due to absorption, WMS measures the difference of signals which is proportional to the target species concentration. Secondly, it shifts measured signal to a relatively higher frequency with improved noise characteristics to achieve improved signal-to-noise ratio and thus higher sensitivity.

In practice, this technique is divided into two categories, namely WMS and FMS. WMS is referred to the cases when the modulation frequency is much lower than absorption linewidth or spectral feature with detection carried out at the fundamental modulation frequency (1f) or higher harmonic frequencies (2f etc.). Typical modulation frequency is usually in the range of a few KHz to a few MHz. For FMS, modulation frequency is usually comparable or even higher than target spectral features.

For electrically pumped laser, particularly semiconductor laser such as QCLs [155, 156], through current modulation to implement WMS technique is widely used in the whole IR range for trace gas detection. Besides current modulation, external cavity modulation could be applied to other types of lasers or light sources such as optical parametric oscillator (OPO) [157, 158] to achieve WMS. Our demonstration of WMS also falls in this category, because we used an optical resonant scanner

outside the laser cavity to modulate the device output wavelength as shown in the next sub-section.

More detailed knowledge about modulation/frequency modulation spectroscopy is beyond the scope of this research work. If interested, please refer to the these publications. [24, 159–168].

3.5.2.2 Wavelength Modulation Demonstration

Same as direct absorption spectroscopy demonstration, WMS with device V9-18-9 was demonstrated using F-P interferometer of fixed cavity length as artificial target gas. To implement wavelength modulation, a fused silica parallel plate mounted on an optical resonant scanner was placed in the pump stripe after cylindrical lens, which wobbles to shift the pump stripe position up and down on the device V9-19-9 as shown in Fig. 3.12, thus selecting different lasing wavelengths. In the figure, pump stripe is in the direction perpendicular to the page. This wavelength modulation was superimposed on top of the wavelength tuning exactly as introduced in the previous section in the demonstration of WMS.

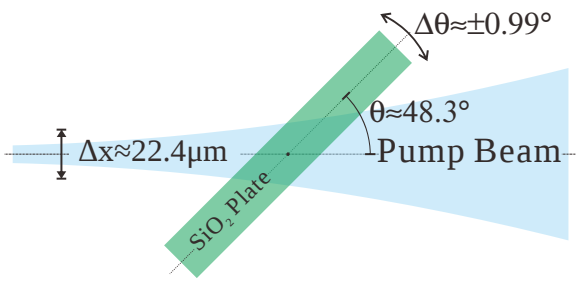

Figure 3.12: Optical resonant scanner with fused silica plate functioning as wavelength modulator on the device V9-18-9

The fused silica plate is 10×6 mm in the directions along and perpendicular to the pump stripe respectively, so not to truncate the pump stripe formed after

cylindrical lens in the pump beam. And the plate thickness is 1 mm for enough pump stripe shift Δx for the laser device wavelength modulation. Plate is AR coated for 1.908 μm at 45$\pm$5°. Determined by the inertia of the this fused silica plate, the resonant/modulation frequency is $\sim$4.35 KHz which is far below the laser spectral linewidth and F-P linewidth so we are in the wavelength modulation regime rather than in a frequency modulation regime when the modulation frequency is large or on the same order compared to the spectral linewidth. The still angle for this plate with respect to the pump beam is measured to be about 48.3° and the oscillation angle $\Delta\theta$ is 0.99° which shifts the pump stripe $\sim$22.4 μm up and down, corresponding to output wavelength difference of $\sim$0.048 nm. This value is much smaller compared to device's typical spectral linewidth of $\sim$1.2 nm, which means our modulation is in derivative modulation regime as shown in Fig. 3.13.

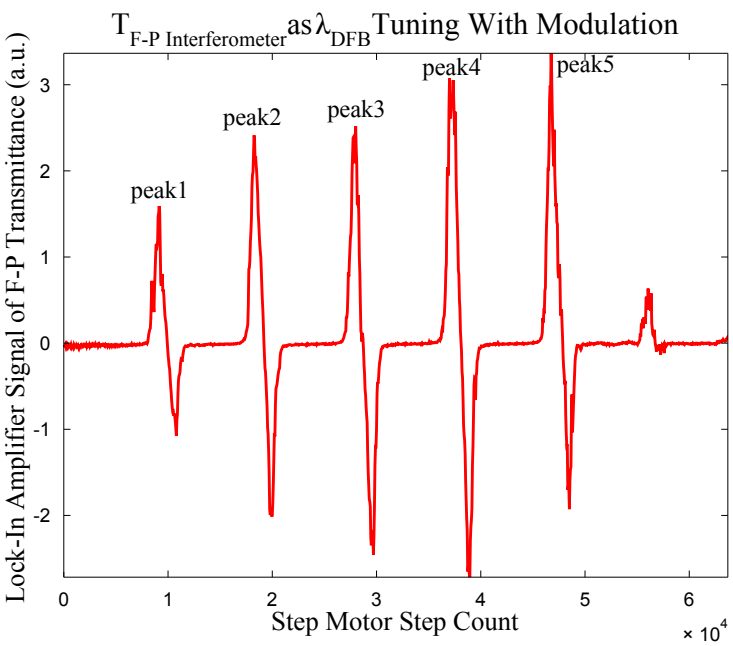

Figure 3.13: Lock-in amplifier signal of F-P interferometer transmittance when λ_{DFB} is modulated with optical resonant scanner in wavelength tuning

In WMS demonstration, the tunable laser device was tuned exactly as the case in

direct absorption spectroscopy as described in the previous sub-section, but without using chopper in data acquisition. The optical scanner's synchronization signal was used as the reference for the lock-in amplifier for the F-P interferometer transmittance measurement. Lock-in amplifier's time constant was still 300 ms and integration time was kept at 1 s as before. The transmittance of F-P interferometer with modulation acquired is shown in Fig. 3.13. It basically corresponds to the derivative signal of the transmittance of F-P interferometer without wavelength modulation as shown the Fig. 3.11.

Because the stage translation starting point and travel in this demonstration were not exactly same as those in the demonstration without modulation introduced in the previous sub-section, so the spectrum peaks shown in this figure is not well aligned with those in the Fig. 3.11. Last peak is incomplete because pump stripe was at the very end of the device. These oscillating peaks are not strictly symmetric with respect to zero amplitude baseline mainly because the device output beam is not perfectly perpendicular to the F-P interferometer cavity mirrors. Assuming the peaks in this figure correspond to roughly the same pump positions to get the transmittance peaks without wavelength modulation as shown in the Fig. 3.11, peak5 looks cleaner than the peak5 which indicates continuous wavelength tuning of the device V9-18-9.

Because we did not have an actual absorbing gas in the wavelength tuning range of our device, we did not investigate the signal enhancement with different modulation strength. So not enough information about SNR could be easily acquired in comparison to the transmittance spectrum acquired without modulation. In the wavelength tuning ranges of F-P interferometer eigen transmittance spectral peaks with present configuration, transmittance signal is generally smooth which indirectly proves that device V9-18-9 tunes continuously.

3.6 Summary

Device V9-18-9 lases in single longitudinal DFB mode at all different pump positions across the whole pump power range, with SMSR of over 30 dB, and achieves maximum single facet output power of about 830 mW without showing signs of thermal roll-over. In other words, the output power is limited by the available pump. This device achieved wavelength tuning range of ∼80nm, from 3056 to 3136 nm at ∼2.5×threshold, typical spectral linewith of ∼1.2 nm. We are very confident that continuous wavelength tuning is demonstrated. Although the spectral linewidth of this device is fairly wide, but it should still be suitable for atmospheric pressure gas remote sensing application. Also the idea of fabricating tunable DFB laser with chirped grating is proved to be feasible. Direct absorption and wavelength modulation spectroscopy were both demonstrated in the lab on this device V9-18-9 with F-P interferometer.

The undesirable issues revealed by this device includes wide spectral linewidth of device emission and the appearance of lateral modes which need to be investigated in the future. Together with experimental investigation for wide spectral linewidth, modeling of lateral/longitudinal chirps' impacts on device spectral linewidth as well as other performance are very necessary and important as part of future work. Narrower pump stripe width with a powerful cylindrical lens should also be investigated.

Besides, due to the present configuration of mounting LN_2 Dewar on the translation stage which is not designed for vertical usage, vibration issue with the translation stage directly affects the laser emission stability which partially caused emission wavelength instability issue and the output power fluctuations through the monochromator. This vertically mounted translation stage should be replaced with a stabler motorized lift stage in future. Furthermore, we also noticed the issue of pump power and device emission power fluctuation issues with water vapor absorption and

turbulence due to air flow in the lab, so a nitrogen purged box covering both the pump beam and laser device emission would be necessary to for more stable operation as well as lowering device output power fluctuations.

Chapter 4

Preliminary Simulation for Tunable DFB Laser Device

In principal, the simulation of the spectral properties of a DFB laser device needs to take into account spontaneous emission or noise. Mathematically demonstrated by other research groups, a Green's function is required together with transfer matrix method to predict the lasing wavelength, spectral linewidth, side mode suppression ratio and other performances in operation [169–176]. About our device, our simulation was particularly focused on calculating emission wavelength of the laser device but not for characteristics such as spectral linewidth, so we did not introduce Green's function in the the simulation of our DFB laser device although it is definitely necessary and should be one of the future works to be carried out. As just mentioned, the main goal of our simulation is to determine the lasing wavelength of the DFB laser device at a given pump position on the device which defines a specific laser cavity with chirped grating as well as pump condition known, and to investigate the impact of both the lateral and longitudinal grating chirps. Based on that, continuous wavelength tuning as pump stripe is translated to different lateral pump positions on the device was also proved with small pump stripe position shift. Transfer matrix

method (TMM) with effective refractive index was utilized in the simulation of our DFB laser device. This simulation work was mainly carried out by Dr. Steve Benoit and implemented using programing language Java, with help and discussion with author.

With the consideration of constructing a model that is flexible and can be adapted to other devices with different designs and fabrication parameters in future, the system modeling is broken down into many sub-modules as shown in diagram Fig. 4.1. The first two rows of sub-modules are meant for the calculation of effective refractive indices and grating period as a function of location on device which have been presented in the previous chapters. The procedure to determine the lasing wavelength of device at particular pump position can be summarized as below. Based on the aforementioned grating period calculation and the the pump stripe geometry, grating periods along an particular pump stripe on the device will be calculated first and then with the 1D slab waveguide model introduced in Chapter 2, effective refractive indices of the grating ridge and groove segments are calculated to construct the transfer matrices of these different segments. The product of this whole set of transfer matrices mathematically describe a particular DFB laser cavity on device defined by the pump stripe. Finally, based on the oscillation condition introduced in this chapter, lasing emission wavelength corresponding to this particular cavity on the device is determined. Basically, the sub-modules enclosed with red dashed-line box shown in the third row of the diagram will be presented in this chapter.

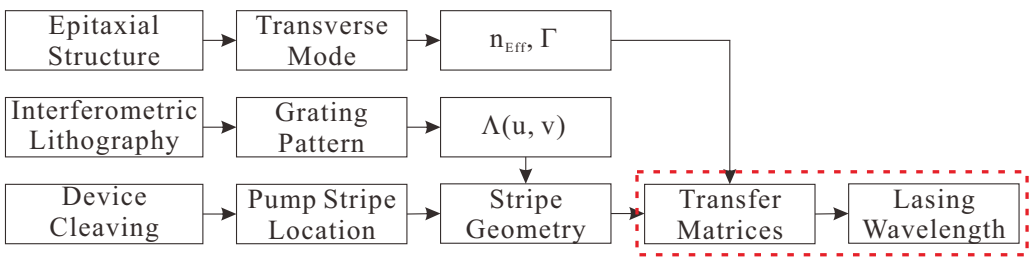

Figure 4.1: Partitioning of system modeling into sub-models

In this chapter, transfer matrix method is first introduced. After that, its application to our hyperbolically chirped grating DFB laser device will be presented in detail, including solving the grating periods along the given pump stripe on the device, the construction of the transfer matrices of chirped grating with pre-calculated grating period and refractive indices and determination of the lasing wavelength.

4.1 Introduction to Transfer Matrix Method

For simulation of DFB lasers, transfer matrix method (TMM) [3,8,169,170,177–184] is a popular approach adopted by many different researchers. It was developed after the extensively used approach of coupled mode theory (CMT) [3, 8, 180, 185] first proposed by Kogelnik and Shank [12] which has limitation of applicability to only shallow corrugations because the theory is based on a perturbation method. It also lacks accuracy in coupling coefficient calculation especially for TM modes on devices [182]. In comparison, TMM has advantages over CMT in aspects such as accuracy for both TE and TM modes in the device simulation, without restriction to shallow corrugations cases, flexibility for chirped grating/layer stack or aperiodic structures and it can also handle some intentional phase shifts at arbitrary locations in the device cavities as well. The detailed introduction to the advantages or features of TMM is out of the scope of this dissertation. Please read the references for more information [3, 8].

TMM is based on a transmission matrix that is defined mathematically for a two bi-direction ports networks module to model either an homogeneous medium in which light propagates or the interface between two different media on which reflection and transmission happen. The transmission matrices for these two different cases are shown respectively by equations 4.1 and 4.2. Usually transmission matrix is a 2×2 matrix, but could have higher dimensions such as 4×4 if additional

parameters need to be considered. The different elements in the matrix embed the physical relationships between the different inputs and/or outputs of the module ports. These two types of unit transmission matrices work as the building blocks for modeling complicated multi-section systems. In modeling of structures such as corrugated waveguide or stack of different material layers, the transmission matrices corresponding to different sections of the system can be conveniently cascaded together through matrix multiplication for the mathematical definition of the whole system.

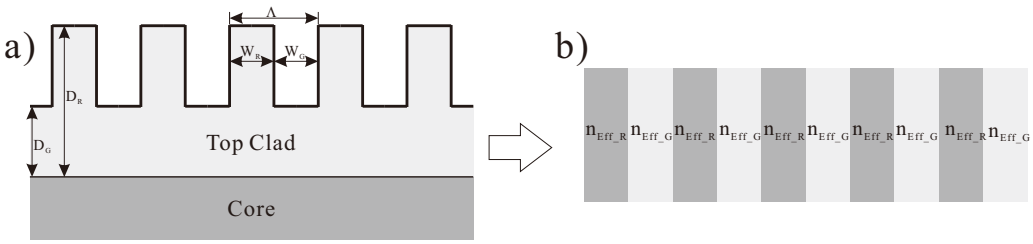

Figure 4.2: Grating is equivalent to layer stack structure with effective refractive index approach

For simulation of our DFB laser, the grating patterned in the top clad as shown in the Fig. 4.2 a) was first converted into the layer stack structure shown in part b) of the figure, through the effective index approach [186, 187] introduced in Chapter 2. The effective refractive indices of these layers corresponding to the grating ridge and groove segments, n_{Eff-R} and n_{Eff-G} assigned are calculated using the 1D slab waveguide mode solver with different top clad thicknesses D_R and D_G as introduced in Chapter 2. And the thicknesses of these layers in the stack structure are exactly same as the width of the corresponding grating ridges and grooves, W_R and W_G as labeled in the figure. After this conversion is done, the unit translation and interface transmission matrices for TMM to define the whole cavity can be defined as shown below. For the ridge or groove segment of the grating, the translation matrix is

written as,

$$\mathcal{T}_i = \begin{bmatrix} e^{-j\phi_i} & 0 \\ 0 & e^{j\phi_i} \end{bmatrix} \quad i = Ridge, Groove. \tag{4.1}$$

Where $\mathcal{T}$ stands for translation and $e^{-j\phi} = e^{-j\tilde{\beta}d} = e^{-j\tilde{n}_i k_0 d}$ represents the phase shift when light wave propagates from one end of the layer to the other. $\tilde{n}_i$ stands for the complex effective refractive index of the layer. Any material gain/loss is embedded in the imaginary part of the effective index. d is the optical path length inside the layer. For the case of normal incidence, it is same as the layer thickness.

Likewise, the coupling matrix for the reflection and transmission on an interface between the ridge and groove segments of the grating or the equivalent layers in the stack could be written as,

$$\mathcal{I}_{ij} = \frac{1}{t_{ij}} \begin{bmatrix} 1 & -r_{ji} \\ r_{ij} & t_{ij}t_{ji} - r_{ij}r_{ji} \end{bmatrix} \quad i, j = Ridge, Groove. \tag{4.2}$$

Where $\mathcal{I}$ stands for interface and subscript ij stands for the location of interface between layers i and j and the light propagates from layer i to j where layer j locates on the right of layer i. r_{ij} and t_{ij} are the field reflection and transmission coefficients calculated with Fresnel relationship, using complex effective refractive indices n_{Eff-R} and n_{Eff-G} of the neighboring layers solved with the 1D slab waveguide mode solver. There are two different cases, namely light propagates through the interface from groove to ridge segment or vice versa. In the simulation of our tunable DFB laser, we only need reflection and transmission coefficients of TE fundamental mode because it has been proved to be the only existing mode of our laser by previous group member, Liang.

With these two unit transmission or transfer matrices and effective refractive index method introduced above, the two-dimensional grating structure shown in the Fig. 4.2 a) can be simplified to the one-dimensional layer stack structure as

shown in part b). The transfer matrix relating the counter-propagating light waves representing the electric fields in laser cavity can be defined as

$$\begin{bmatrix} a_{m+1} \\ b_{m+1} \end{bmatrix} = \begin{bmatrix} T_{11}^{(m)} & T_{12}^{(m)} \\ T_{21}^{(m)} & T_{22}^{(m)} \end{bmatrix} \begin{bmatrix} a_m \\ b_m \end{bmatrix} = \mathbf{T^{(m)}} \begin{bmatrix} a_m \\ b_m \end{bmatrix}. \tag{4.3}$$

Where section m+1 locates to the right of section m, a_i and b_i stand for the light waves propagating in the right bound and left bound directions respectively as mentioned above and $\mathbf{T^{(m)}}$ represents the transfer matrix for $\mathbf{m}th$ section of the whole cavity. By $\mathbf{m}th$ section, we mean $\mathbf{m}th$ layer and the interface on the-left hand side boundary of this layer as shown in the Fig. 4.2 b). So depends on the layer correspondence to either grating ridge or groove, the section transfer matrix can be expressed as

$$T_{R-Section}^{(m)} = \mathcal{T}_R^{(m)} \mathcal{I}_{GR}^{(m)} \tag{4.4a}$$

$$T_{G-Section}^{(m)} = \mathcal{T}_G^{(m)} \mathcal{I}_{RG}^{(m)}. \tag{4.4b}$$

Then the transfer matrix for a single period consists of ridge and groove sections, the $\mathbf{m}th$ period can be written as following if the period started with grating ridge section.

$$T_P^{(m)} = T_{G-Section}^{(m)} T_{R-Section}^{(m)} \tag{4.5}$$

With transfer matrix for a single period of grating, the transfer matrix $\mathbf{M}$ for the whole cavity or the whole complicate structure then can be constructed and written as

$$\mathbf{M} = T_P^{(\mathcal{L})} T_P^{(\mathcal{L}-1)} T_P^{(\mathcal{L}-2)} ... T_P^{(1)} = \prod_{i=1}^{\mathcal{L}} T_P^{(i)} \tag{4.6}$$

Where $\mathcal{L}$ is the total number of grating periods. And the matrix multiplication shown in above equation is right multiplication, which means the matrices standing for different components of the whole cavity appear in multiplication in the reverse

order of what they do in the actual cavity from left to right facet. This is very important especially for our DFB laser device because of the existing grating chirp or asymmetric variation of grating periods relative to the center of the cavity defined by the pump stripe on device, as shown in Fig. 4.3 in section 4.3 of this chapter.

4.2 Presumptions to Simplify TMM Simulation

To simplify the device simulation, the following assumptions were made.

- The grating cross-section profile is assumed to be perfectly rectangular, and we neglect all kinds scattering and other types of loss from the actual grating profile as shown in the Fig. 2.26.

- Although the actual non-normal grating line angle with respect to the pump stripe in grating normal configuration (GNC) as shown in Chapter 2 is taken into account for the calculation of the amplitude of the elements in transfer matrices, we neglect the loss from the reflection, refraction and scattering on the interfaces of equivalent grating ridge/groove layers and also assume that the counter-propagating light does not deviate in the lateral directions from the laser cavity axis defined by the pump stripe. The actual case is that some of the light in cavity will leak from the side of the cavity (determined by the width of pump stripe) after propagating for certain distance due to the reflection, refraction and scattering on these grating ridge/groove interfaces at oblique incident angles because grating lines are not perfectly perpendicular to the pump stripe. Of course, the gain guiding mechanism in the lateral direction pulls some of the these deviating lights back to the cavity.

- In the simulation, the real part and the imaginary part of the effective refractive index are assumed to be independent, although they are correlated by Kramers-

Kronig relationship. The real part of effective refractive index stays fixed in our simulation, when its imaginary part is increased to determine the lasing wavelength with our approach introduced in section 4.5 of this chapter. The increase of the imaginary part of effective refractive index corresponds to the increased carrier density and effective material gain. From the imaginary part of effective refractive index, the threshold condition calculation of the laser device can be conducted and this is a common approach.

- Across the full tuning range of our DFB laser device or the gain spectrum in the vicinity of 3.06 μm, material gain was assumed to be constant.

- In the pump region or cavity defined by given pump stripe on the device, the intensity of field is assumed to be uniform although in directions along and across the pump stripe beam the intensity follows Gaussian distribution. Based on above assumption, the effective refractive index along the whole length of the pump stripe is same. And we also don't take the width of pump stripe into account in the simulation.

- Facet reflections are neglected due to grating normal configuration (GNC) as presented in section 4.3.

4.3 Cavity Transfer Matrix Construction

As shown in the Fig. 4.1, the transfer matrix required to simulate the DFB laser cavity defined by optical pump stripe is constructed with information of the grating period along this particular pump stripe at given position on the device and the effective refractive indices corresponding to the ridge and groove segments of the grating. The effective refractive index calculation has been presented in section 2.3. In this section, we will concentrate on how to calculate the dimensions of the grating

ridge and groove segments along the pump stripe and their locations required to define the unit transfer matrices which are later multiplied together to construct the total transfer matrix of the laser cavity. Duty cycle of grating which is defined as the percentage of ridge width to the whole period is set at 50% in all the calculations in this section for simplicity, which was also the target value in fabrication as shown in the Fig. 2.26.

As introduced in the previous chapters, period of the chirped grating patterned on our DFB laser device is location dependent. In other words, even along a given pump stripe at arbitrary pump position on the device, the grating period varies from one end of the stripe to the other. To get the dimension of the ridge and groove segments as well as their location within each grating period, the grating periods along the pump stripe have to be calculated first. With chirped grating period calculation method introduced in section 2.6, grating periods along any pump stripe on the device in GNC can be easily calculated with location coordinates on the pump stripe, or coordinates on a straight line that defines the pump stripe. Basically, use the coordinates of the pump stripe, (u, v) defined by the straight line function in the grating period calculation equation 2.18 to get the values of grating periods along pump stripe on the device. As an example of the calculation, grating periods along pump stripe defined by straight line equation $v = tan(6°)u + v_{intercept}$ with $v_{intercept}$=5.5 mm is shown as the red curve in Fig. 4.3. The relative pump position on device can be derived from device dimension and cleaving location as shown in the Fig. 2.24.

With grating periods along the pump stripe known, determining the particular location and dimension of grating ridge within each period also matters in TMM simulation because these parameters affect the calculation of light propagation phase in the cavity. The approach we took for this problem is to solve first for the starting/ending points or boundaries of individual grating periods along the pump stripe.

Then, depending on the tone of PR in IL patterning as well as known grating duty cycle, the location and dimension of grating ridge within every single period can be calculated as presented below.

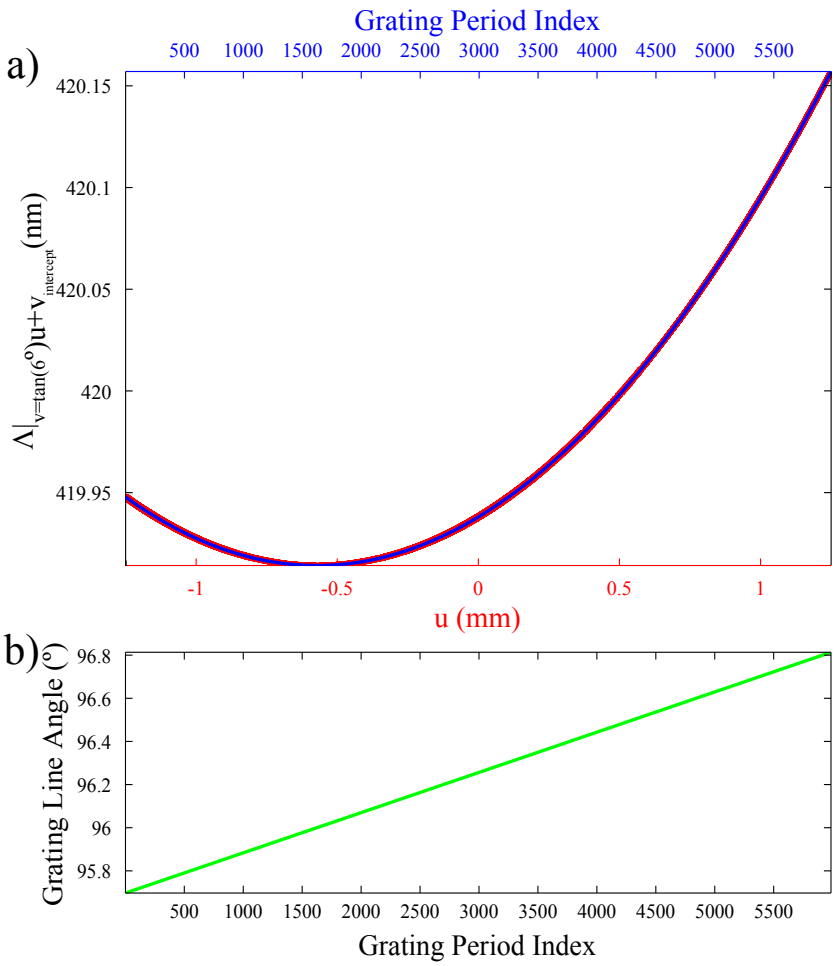

Figure 4.3: a) Grating periods along a given pump stripe defined by straight line, $v = tan(6^\circ)u + v_{intercept}$ with $v_{intercept}$=5.5 mm for the cavity transfer matrix construction. Red curve is the grating period along the pump stripe calculated with grating period equation 2.18, and the blue curve stands for reconstructed grating period as function of location in the cavity referred by grating period index. b) Grating line angle with respect to the pump stripe in GNC at different location of cavity referred by grating period index.

Specifically, the location of the minimum grating period for a given pump stripe needs to be solved first. Due to the optics configuration in IL patterning and cleaving position of our DFB laser device from the 10×10 mm die, locations of minimum grating period along pump stripe at different positions in GNC correspond to the intersections of the pump stripes and the zero optical path difference interference fringe on the device surface from the two spherical waves (given by straight line equation, $v = tan(96°)u$ as seen in the Fig. 2.23 a). Once the location of this minimum grating period on the pump stripe is determined, the grating period Λ_0 (also the minimum grating period) centered at this location can be used to find its boundary (u_{0-}, v_{0-}) and (u_{0+}, v_{0+}) on the pump stripe. This period is referred as the center grating period. With boundary of the center period solved, grating periods at (u_{0-}, v_{0-}) and (u_{0+}, v_{0+}) are calculated as the first grating periods Λ_{-1} and Λ_1 on the left and right sides of the center period. The boundary coordinates of the center period, (u_{0-}, v_{0-}) and (u_{0+}, v_{0+}) are used as the starting points of these two first grating periods to the left and right side respectively. This is different from minimum grating point as the center of the center grating period, but the error due to this is very small considering the grating period variation (longitudinal chirp) along the pump stripe on the device is on the order of 0.1% as shown in the Fig. 2.23. Then the ending points of these two first grating periods, (u_{1-}, v_{1-}) and (u_{1+}, v_{1+}) are calculated and used for the calculation of the second grating periods, Λ_{-2} and Λ_2 on both sides with (u_{1-}, v_{1-}) and (u_{1+}, v_{1+}) taken as starting points of the periods. In this manner, boundaries of all grating cycles can be solved sequentially till the left/right edges of the cavity (or pump stripe) are reached. This process is illustrated in Fig. 4.4. If we call this recalculation of grating period along the pump stripe, we can get the grating period as function of its location on given pump stripe or in the cavity defined by the pump stripe. After renumbering the grating period index, starting from 1 at the left facet of device and increasing as moving to the right hand side in the cavity (or along the pump stripe), the recalculated grating

period as function of period location referred by grating period index is also plotted in blue curve shown in part a) of the Fig. 4.3. Obviously, it agrees very well with the overlaid grating periods calculated with derived formula shown in the red curve.

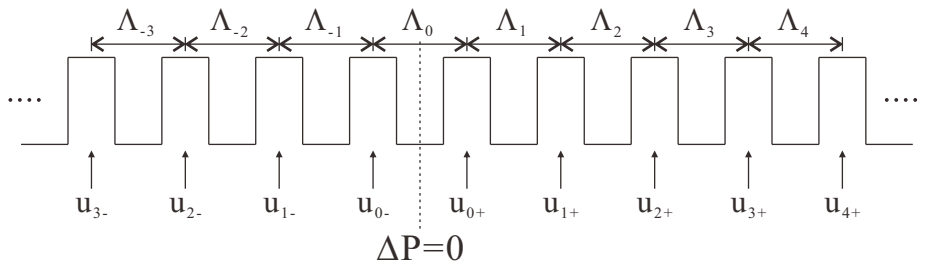

Figure 4.4: Schematic of grating profile along arbitrary pump stripe. Point $\Delta P = 0$ corresponds to the intersection of zero optical path difference interference fringe on device and pump stripe. Λ_i and u_i are the grating periods and their boundaries' horizontal coordinates along the pump stripe. The subscript of Λ is later renumbered starting from 1 from the left facets of cavity in rising order as moving to right hand side till right facet, not shown in the figure.

After the grating periods along the pump stripe were solved as presented above, the location of grating ridge within a period can be determined with tone of the PR used in IL and assumed duty cycle. Since we used positive PR (SPR-505) in IL patterning for this chirped grating, along the zero optical path length difference interference fringe on the device as mentioned above, a groove in PR formed due to constructive interference which later corresponded to a groove in grating after pattern transfer from PR to the top clad of the device. So along an arbitrary pump stripe, at the location where this zero optical path length difference fringe and pump stripe intersect, as labeled as $\Delta P = 0$ in Fig. 4.4, the grating has a groove. The groove and ridge profile in the center grating cycle is symmetric with respect to the $\Delta P = 0$ point. For a given duty cycle value, the location and dimension of groove and ridge can be calculated. Likewise, grating ridge and groove dimension and location are calculated for all of the rest of the grating cycles along the pump stripe.

With the method introduced above and the assumed 50% duty cycle, grating ridge dimension in each period is summation of the last quarter of the previous grating cycle and the first quarter of present cycle as shown in the Fig. 4.4. The grating profile along any arbitrary pump stripe is illustrated in the figure with all the grating periods Λ_i and horizontal grating cycle boundary coordinates u_i labeled. The last grating cycle at either of DFB laser facets might be fractional which is also taken into account in our cavity transfer matrix construction. The grating cross section profile reconstruction with calculated dimensions and locations of grating ridges/grooves as explained above was then conducted to extract the information on the equivalent layer thickness in the layer stack as shown in the Fig. 4.2, with effective refractive indices assigned to the particular layer accordingly.

In the construction of the cavity transfer matrix, the laser output medium next to cavity facets also needs to be considered in TMM simulation because of the reflection from the facet/output medium interface due to impedance mismatch. But for our laser, grating orientation is 6° tilted with respect to the facts, also the pump stripe is applied in GNC or perpendicular to the grating lines, as shown in Fig. 4.5. Because of this special configuration, the reflection from the facets does not go back to the cavity defined by pump stripe as shown. Also, the reflected light from facets will be absorbed in material and scattered away by gratings due to its non-perpendicularity to the grating lines. Mathematically, to represent this non-reflection, the refractive index of output medium (which is air actually.) is set to be the effective refractive index of the facet segments in grating, either ridge or groove to eliminate all reflection back into the laser cavity.

With all these steps explained, the transfer matrix that represents the DFB laser cavity defined by pump stripe at a particular pump position on device can be written as following.

$$M_{cavity} = T_P^{(rightfacet)} T_P^{(L-1)} T_P^{(L-2)} ... T_P^{(2)} T_P^{(leftfacet)} \tag{4.7}$$

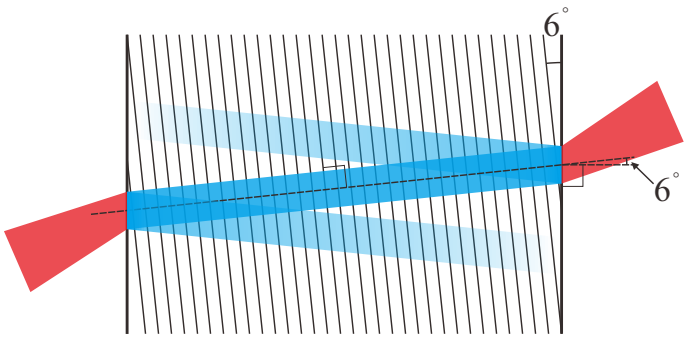

Figure 4.5: No facet reflection due to tilted grating orientation and pump stripe in grating normal configuration (GNC). The reflections from the facets of cavity defined by pump stripe deviate from cavity as shown.

Where $T_P^{(i)}$ is the transfer matrix for ith grating period that could be written according to equation 4.5 in the section 4.1, and there are L-2 full grating periods along the pump stripe, from the $2nd$ to (L-1)th. Transfer matrix for the left facet fractional grating period, $T_P^{(leftfacet)}$ represents the transfer matrix for the first grating cycle, which very likely starts with a fractional groove or ridge segment depending on the particular pump stripe position on the device. In the construction of transfer matrix for this cycle, this fractional grating segment is converted to a semi-infinitely thick layer with same effective refractive index as the fractional grating segment due to the no-facet-reflection assumption introduced above. And this layer will not appear in the multiplication of matrices for the first grating cycle transfer matrix. Instead, the transfer matrix for the interface between this fractional segment and the neighboring full grating segment (belongs to the next grating cycle) will be the first matrix (last matrix in the matrix multiplication as introduced) in the construction of the cavity transfer matrix. Likewise, the fractional segment of the right facet grating cycle will also not appear in the multiplication for the cavity transfer matrix. The interface matrix for the interface between last full grating segment and the fraction segment will be the last component of cavity (first in matrix multiplication). Basically the front and rear facet grating period transfer matrices need to be constructed especially

according to recalculated grating periods along the given pump stripe.

For brevity of description, we do not write down all the transfer matrices for different segments or interfaces of the gratings for the cavity transfer matrix. But examples of unit translation transfer matrix and interface matrix are listed as below as building blocks of the cavity transfer matrix. The translation transfer matrix can be written as

$$\begin{bmatrix} a_{m_{right}} \\ b_{m_{right}} \end{bmatrix} = \begin{bmatrix} e^{-j\tilde{n}_m k_0 W_m/\cos\theta} & 0 \\ 0 & e^{j\tilde{n}_m k_0 W_m/\cos\theta} \end{bmatrix} \begin{bmatrix} a_{m_{left}} \\ b_{m_{left}} \end{bmatrix}. \tag{4.8}$$

Where a and b stand for left/right bound propagation light waves respectively, same as before. Subscript m_{right} and m_{left} represent the location of right and left boundary of mth layer in the stack, which could be a ridge layer or groove layer. $\tilde{n}_m$ is the complex effective refractive index in the layer. And $W_m/\cos\theta$ is the optical path length of propagation inside the layer with W_m stands for the layer thickness and θ as the propagation angle with respect to the normal of the boundaries. k_0 is the vacuum wave vector of the laser emission wavelength.

And the interface transfer matrix can be written as

$$\begin{bmatrix} a_{m+1} \\ b_{m+1} \end{bmatrix} = \frac{1}{2} \begin{bmatrix} 1+\frac{\tilde{n}_t\cos\theta_t}{\tilde{n}_i\cos\theta_i} & 1-\frac{\tilde{n}_t\cos\theta_t}{\tilde{n}_i\cos\theta_i} \\ 1-\frac{\tilde{n}_t\cos\theta_t}{\tilde{n}_i\cos\theta_i} & 1+\frac{\tilde{n}_t\cos\theta_t}{\tilde{n}_i\cos\theta_i} \end{bmatrix} \begin{bmatrix} a_m \\ b_m \end{bmatrix}. \tag{4.9}$$

Where subscript $m+1$ and m are the indices of neighboring layers sharing the common interface. $\tilde{n}_i$ and $\tilde{n}_t$ are the complex effective refractive indices of incident and transmitted media. θ_i and θ_t are the propagation angles in the incident and transmitted layers determined by Snell's law, respectively. As for the calculation of the angles by Snell's law with complex refractive indices, please refer to Appendix B.

The Complex refractive index takes the form of

$$\tilde{n} = A - jB, \quad with \quad A > 0,\ B = \frac{g}{2\beta} \geq 0 \tag{4.10}$$

Where the imaginary part of the effective index, B has connection to the intensity gain, g as shown. $\beta = k_0 A$ is the wave vector of the guided mode in the slab waveguide shown early. In our device, it is the wave vector of fundamental TE mode as calculated in Chapter 2.

After the cavity transfer matrix was assembled for a particular pump stripe position on device with the procedure presented as above, the simulation first conducts a so called cold-cavity calculation of cavity reflection and transmission, with the imaginary part of effective refractive indices set to zero. These effective refractive indices were solved with method introduced in Chapter 2. Then, the imaginary part is added to effective refractive index for oscillation condition or lasing wavelength determination as introduced in section 4.5.

4.4 Simulation Program Graphic User Interface (GUI)

Before presenting the method we applied to determine the lasing wavelength of oscillation condition, I introduce briefly the simulation program interface. This simulation program was written with Eclipse integrated development environment, using programming language *Java*. Also as mentioned in the beginning of this chapter, the whole program is broken into modules as illustrated in the Fig. 4.1. Here, we only shown two particular screen snapshots of the graphic user interfaces of our simulation program.

Fig. 4.6 is the screen snapshot of device simulation parameters setting interface, with all the information such as epi-structure dimensions, effective refractive indices of fundamental TE mode in slab waveguide, chirped grating periods as function of location on the die, device dimensions and cleaving location determined with

previous calculations done in different modules of program, not shown in the figure. Mainly, the parameters to be set before start device simulation are shown in the middle section of the interface, namely the loading of the above mentioned parameters stored in the device model "Xiang device" highlighted in the list on the left-hand side window of the interface, grating duty cycle, pump stripe angle, pump stripe width and normalized pump stripe lateral position on the device (0 at one end and 1 at the other end). Cross-section of the DFB laser device is shown in the middle bottom section, and pump stripe position on device is shown in the right-hand side section on the interface as shown in the figure.

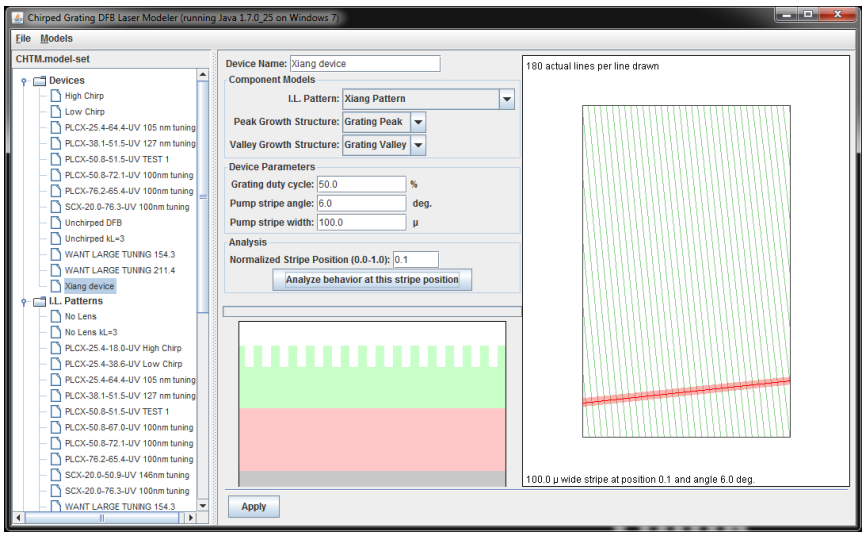

Figure 4.6: Screen snapshot of the simulation program device parameter setting interface. Normalized pump position is at 0.1, with stripe angle of 6° and stripe width of 100 μm. Chirped grating duty cycle is set at 50%, uniform along the laser cavity defined by the pump stripe shown as pink bar in the figure.

Fig. 4.7 is the real time simulation result display interface which has different tabs such as , Transmission/Reflection, $M_1 1$ Norm, Field Intensity and Field Visualization. Here shown in the figure, it is the tab of the transmission and reflection of the above laser cavity. Top half is the amplitude information of the transmission and

reflection shown in red and blue curve respectively and the bottom half is the phase difference display of the two cases, no gain or threshold gain. The wavelength range of the plots on this interface was set to be ±5 nm in the vicinity of target Bragg wavelength with calculated average grating period and effective refractive index using equation 2.6. Obviously due to the existing chirp and asymmetry in the grating in the cavity, as shown in the Fig. 4.3, the cavity reflection and transmission plot as function of wavelength is asymmetric as shown.

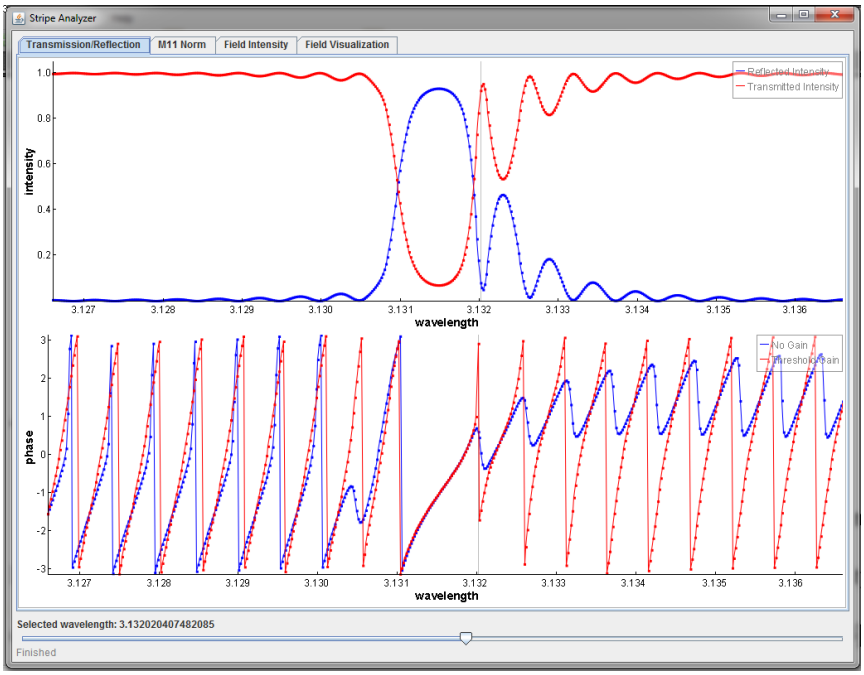

Figure 4.7: Screen snapshot of the simulation program graphic user interface. It is the tab of reflection and transmission and phases difference of the cavity defined by the particular pump stripe shown in the Fig. 4.6.

4.5 Determining Lasing Wavelength

For a laser to reach threshold, it must sustain a left-bound propagating output wave at the left facet and a right-bound output wave at the right facet without inputs at either one. Mathematically for this to occur, the cavity transfer matrix must meet the condition as shown in the following equation.

$$\begin{bmatrix} 0 \\ R \end{bmatrix} = \mathbf{M}_{cavity} \begin{bmatrix} T \\ 0 \end{bmatrix} = \begin{bmatrix} \tilde{M}_{11} & \tilde{M}_{12} \\ \tilde{M}_{21} & \tilde{M}_{22} \end{bmatrix} \begin{bmatrix} T \\ 0 \end{bmatrix} \tag{4.11}$$

Where R and T stand for left and righ-bound outputs or intensity of electric field from the cavity facets. Cavity transfer matrix $\mathbf{M}_{cavity}$ is also called characteristic matrix, with $\tilde{M}_{11}$, $\tilde{M}_{12}$, $\tilde{M}_{21}$ and $\tilde{M}_{22}$ as the four elements constructed with procedure presented in the previous sections in this chapter. The lasing condition expressed in the above equation implies that $|\tilde{M}_{11}|$=0. This oscillation condition is same as that reported in Makoto Yamada *et al.*. [188].

As shown in Fig. 4.8, in the process of determining the lasing wavelength or oscillation condition at a particular pump position on device, we first construct the cavity characteristic matrix and calculate the the value of $|\tilde{M}_{11}|$ with real effective refractive index and plot it in the vicinity of target Bragg wavelength as shown in the blue curve in the figure. Then the imaginary part of the effective refractive index is slowly increased, which will change the curve of $|\tilde{M}_{11}|$ slightly and also shift it down as seen. As the imaginary part of refractive index further increases, then at a particular value, $|\tilde{M}_{11}|$=0 condition is met as shown as the red curve in the figure. The wavelength at which $|\tilde{M}_{11}|$ reaches its zero corresponds to the lasing wavelength. The imaginary part value which lets $|\tilde{M}_{11}|$ get value of 0, can be converted to an effective threshold intensity gain using equation 4.10 and further leads to threshold carrier density. This will be part of future work on this project.

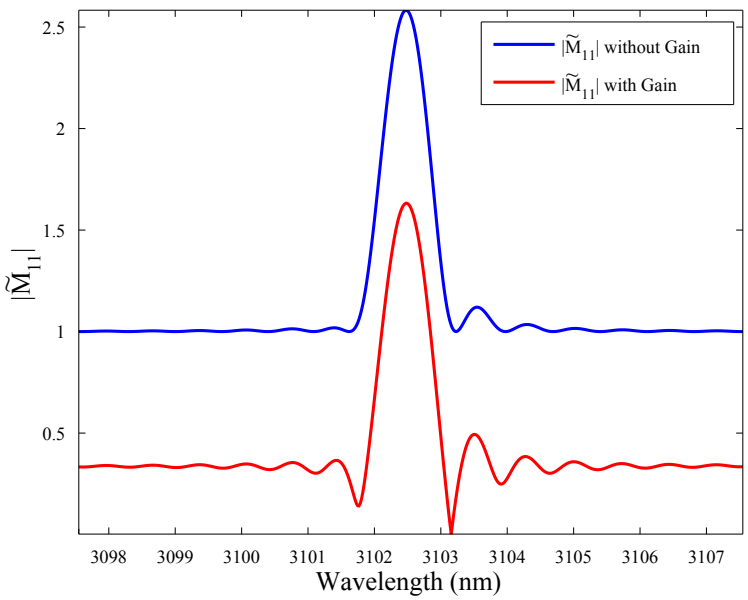

Figure 4.8: Example plot of $|\tilde{M}_{11}|$ as function of wavelength in the vicinity of target Bragg wavelength. The wavelength at which $|\tilde{M}_{11}|$ reaches zero corresponds to the lasing wavelength.

4.6 Continuous Tuning

4.6.1 Wavelength Tuning Simulation on Previously Fabricated Device with larger Longitudinal Chirp

To prove that our simulation program is capable of predicting mode hopping or wavelength tuning discontinuity on DFB devices and also for comparison reasons, wavelength tuning calculation was carried out on a previously fabricated device, V9-18-3 which has a larger longitudinal chirp. Chirped grating on V9-18-3 was patterned using a more powerful plano-convex lens, PLCX-25.4-18.0-UV with die tilting angle β=0°, $C_X = C_Y$=0 mm and C_Z=2 mm. For this device with dimensions of 2.5×4 mm in longitudinal and lateral directions respectively and cleaved from the same

location on the die as V9-18-9, the longitudinal chirp along the pump stripe in GNC is in the range of 0.57% to 0.84%, almost 10 times larger than that of the device V9-18-9 shown in the Fig. 2.23.

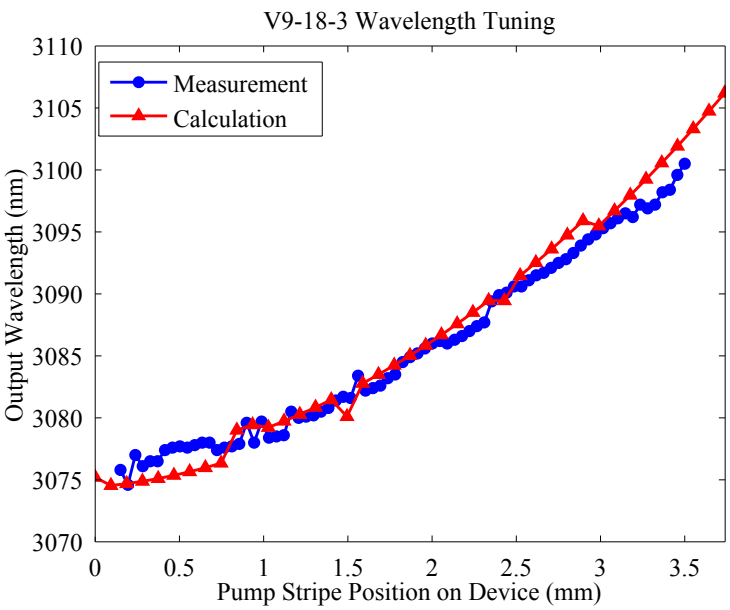

Figure 4.9: Simulated lasing wavelength as function of pump stripe position on device V9-18-3, in red. The wavelength tuning measurement result acquired at ∼2.5×threshold is shown in blue curve.

The simulated wavelength tuning curve of this device together with the actually measured output wavelength as function of pump stripe position on the device are plotted as shown in the Fig. 4.9, in red curve and blue curves, respectively. Wavelength measurement was conducted at 77 different pump stripe lateral positions and simulation calculated 41 different pump positions on this device. Although the calculated data does not match the measured values perfectly due to practical reasons such as, over-simplified model, pump power in measurement higher than threshold pump power, device fabrication/cleaving defects or uncertainties and so on, the simulation shows discontinuity of wavelength tuning at different pump positions on the device. Apparently, the simulation program is capable of predicting potential mode

hopping or discontinuity in wavelength tuning. Also, it is proved that large longitudinal chirp along the pump stripe is not desirable and will cause issues such as mode hopping in the wavelength tuning process. We think one of the reasons underlying the wavelength discontinuity issue is that different grating periods along the pump stripe select different lasing wavelengths, so that these is not enough length of grating with a particular period to select the corresponding lasing wavelength and make the lasing mode at this wavelength have a threshold significantly lower than that of the other modes. In other words, the lack of wavelength selectivity due to large longitudinal chirps makes many different wavelengths/modes have similar loss and threshold that lasing mode hops from one to another with small changes in pump stripe position.

4.6.2 Wavelength Tuning of Device V9-18-9

After proving that our simulation code is capable of predicting wavelength tuning discontinuity on tunable laser device previously fabricated, it was applied on the device V9-18-9 in hope to prove it can be continuously tuned which is also the most important feature of the device. As mentioned in Chapter 3, coarse wavelength tuning was tested on the device V9-18-9 by translating pump stripe at 51 different positions across its full lateral dimension (4 mm) at about 2.5× threshold and we did not notice kinks or discontinuity in the device output wavelength. Neither did we notice degenerate DFB mode hopping which is a very typical issue among the index-coupled DFB lasers. Because the wavelength tuning step in the above test was as large as the grating stop band width, we also conducted fine wavelength tuning test in an arbitrary section on the device with much smaller tuning step as shown in the Fig. 3.7, the test result on device was not fully conclusive but we can tentatively rule out the existence of F-P modes or degenerate DFB mode hopping issues.

As a very important part of numerical simulation of our device, we conducted wavelength tuning simulation on V9-18-9 by calculating the lasing wavelength with the above mentioned method at a series of closely spaced pump positions on the device. Across the full lateral dimension of the device V9-18-9, lasing wavelengths at 161 equally separated pump stripe positions were calculated, with pump stripe position shift of ∼23.4 μm corresponding to nominal wavelength tuning step of ∼0.5 nm, as plotted in the blue curve shown in Fig. 4.10. Together with the simulation curve, experimentally measured device output wavelengths at 51 different pump positions are also shown in the scattered red triangles as seen.

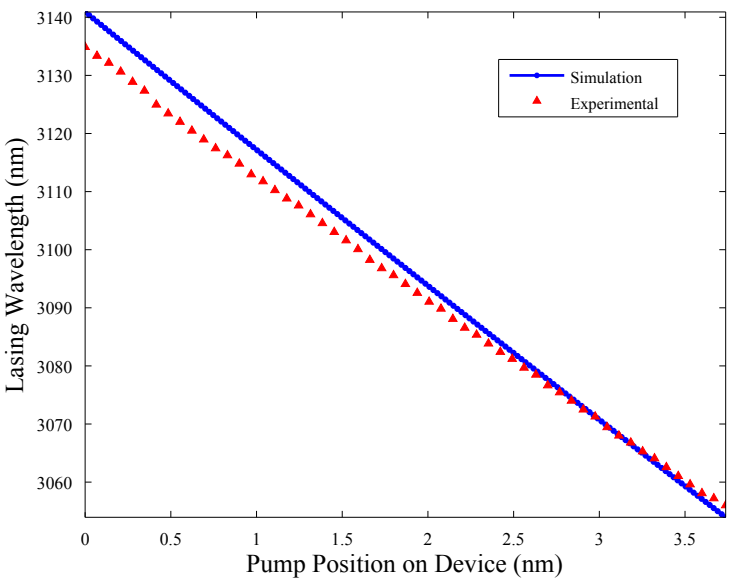

Figure 4.10: Simulated lasing wavelength as function of pump stripe position on device V9-18-9. Together with simulation results, measured output wavelength of this device at ∼2.5×threshold is also shown as red scattered triangles.

As seen in the figure, experimental results of lasing wavelength agree with our simulation within reasonable tolerance. Simulated output wavelength shown in the blue curve changes smoothly at these 161 different pump positions without showing discontinuities across the whole lateral dimension of the device V9-18-9. As men-

tioned above, the pump stripe shift of $\sim$23.4 μm was picked for a wavelength tuning step of about 0.5 nm which should be smaller than the stop band width of our DFB laser device to prove the wavelength tuning is not affected by degenerate DFB mode hopping. Although we still don't know exactly the stop band width of the device, but it should be on the order of 1 nm or slightly large according to the Fig. 4.7 and 4.8. So if mode hopping happens between degenerate DFB modes, the simulation code should be able to catch some output wavelength jumps. With this explained, we can conclude that this device V9-18-9 can be tuned continuously and does not have typical DFB mode degeneracy issue with index-coupled DFB lasers.

4.7 Summary

In this chapter, the transfer matrix method (TMM) and its application in simulation of DFB laser through effective refractive index approach was first briefly introduced. Specifically for our tunable device V9-18-9, simulation program modularization, assumptions for simulation simplification, construction of cavity transfer matrix at particular pump stripe location as well as oscillation condition were introduced consequently. Finally, continuous wavelength tuning of the device was simulated and proved by solving for the laser emission wavelengths at a series of closely spaced pump stripe positions across the whole lateral dimension of the device.

Apparently, although the present model used in simulation gives some primary results as presented, it does not work well enough to match the measurement results as shown in the discrepancy in the Fig. 4.9 and 4.10. Of course, this could also be due to not accurate enough knowledge of grating chirps. The major task in future about modeling is to develop more comprehensive model to better simulate the real device properties under actual operation conditions, including above threshold cases. The improvements in the modeling can be summarized from the following aspects.

For example, gain medium dispersion and Kramers-Kronig relationship should be taken into account in calculation of effective refractive indices. TMM should also be combined with Green's function meanwhile taking into account other physical processes such as modes competing and spatial hold burning. Lateral/longitudinal chirp from the hyperbolic grating need to be taken into account for better evaluation of various types of losses to calculate device threshold. Simulations on threshold gain margin of the different possible lasing modes if there are, spectral linewidth, side mode suppression ratio, above threshold performance with potential spatial hole burning or saturate gain, static and dynamic performances of the device and so on need to be carried out with the new model in future. Of course, correlating the device characteristics under different working conditions with design and fabrication parameters through simulation to offer theoretical guidance for design, parameter optimization and fabrication procedures should be one of the major tasks for the modeling work in future.

Chapter 5

Conclusion and Future Work

In this chapter, achievement of this tunable DFB laser project is first summarized. After that, primary future work are also proposed.

5.1 Conclusion

As shown in the previous chapters, incorporating DFB technology with type-II InGaSb/InAs multiple QWs gain medium, we have designed, fabricated and characterized an optically pumped Mid-IR tunable DFB laser which is a promising candidate for spectroscopy related applications such as remote gas sensing, chemical reaction process control. As one of the devices have be fabricated, V9-18-9 has demonstrated features including:

- Narrow spectral linewidth, with typical value of 1.2 nm at $\sim$2.5$\times$ threshold. Although this spectral linewidth is fairly wide for low pressure spectroscopy applications or fine spectral structure resolution, it should be suitable for remote gas sensing at atmospheric pressure or higher pressure.

- High output power. The highest single facet output power acquired in characterization is about 830 mW and is still limited by available pump power. We are very confident to scale up the output power to the order of several watts.
- Continuous-wave (CW) operation, which is preferable for spectroscopic applications.
- Single longitudinal mode (SLM) operation, prerequisite for most spectroscopy applications. This device did not show degenerate DFB mode issue in the characterization, which is a typical problem with index-coupled DFB lasers. The possible reason is that the longitudinal chirp in grating along the cavity breaks the symmetry of the degenerated DFB modes.
- Wide continuous wavelength tuning range. Device V9-18-9 shown about 80 nm in the tuning test. And it should be fairly easy to achieve over 100 nm tuning range with present technical approach and gain medium.
- Easy to apply wavelength modulation (WM) technique on the device for enhancement of signal noise ratio (SNR). This feature is very useful in spectroscopy and it is very convenient to implement together with our device.

Other than the above mentioned device features, we have improved technique of chirped grating control in interferometric lithography, especially for wavelength tuning or related purposes. And we believe this technique could be applied to other type of lasers or other fields.

5.2 Future Work

Despite the overall success in the development of this high-power, SLM and continuous widely-tunable DFB laser device as a suitable candidate light source for spec-

troscopic applications, several issues remain to be addressed in future work. First, spectral linewidth of the present device is still relatively broad for spectroscopy application due to longitudinal/lateral chirps or the large width of the cavity and lack of mode confinement in lateral direction due to gain guiding from pump stripe. For the goal of narrowing the linewdith down to 0.5 nm or even less to meet the requirements for higher spectral resolution, impacts from longitudinal as well as lateral chirps on spectral linewidth need to be further investigated through both simulation and experiments. Second, although no DFB mode degeneracy issue was noticed in the characterization of this index-coupled DFB laser, theoretical analysis or explanation are required for an better understanding the underlying reason of it. At this moment, we think the grating chirps, especially longitudinal chirp inherently solves the degeneracy issue as shown by the asymmetric structure in the transmission curve in the Fig. 4.8, obviously different from traditional DFB lasers. Based on that, technical approaches or parameters determination or optimization in device design and fabrication to avoid DFB degeneracy issue needs to be proposed for the goal of achieving a high dynamic range of stable single-mode operation. Third, demonstration of even wider wavelength tuning range with this approach needs to be conducted to reach the full potential of this wavelength tuning technique. Fourth, a better model needs to be developed to better simulate our device for a comprehensive and profound understanding to this type of tunable DFB laser device as mentioned at the end of Chapter 4. Last, a better performance device should be fabricated and tested in field experiment.

5.2.1 Investigation on Lateral and Longitudinal Chirps

The first two future works listed previously both involve a better understanding of the chirped grating's impacts on the characteristics of our tunable DFB laser device. At present, the biggest concern of the device V9-18-9 is its broad spectral linewidth

of ∼1.2 nm at about 2.5× threshold. Although it might be still applicable for remote sensing application at atmospheric pressure due to the pressure broadening of target gas' signature absorption spectral lines on the order of ∼ 1.2 nm [189,190], it is always better to have a narrower spectral linewidth for higher spectral resolution which also leads to a much wider range of applications. The possible reasons of the broad device spectral linewidth are presented in the section 3.4. In short, investigation into the longitudinal and lateral chirp associated with our method of hyperbolically chirped grating patterning on this type of tunable DFB laser device should be carried out theoretically and experimentally. The goal of this investigation is to optimize the chirped grating for an ideal wavelength tuning range and maintain decent spectral linewidth of ∼0.5 nm at the same time.

Longitudinal chirp in DFB lasers has been investigated by many research groups and it has effects on almost all different characteristics of DFBs. The positive ones with an appropriately designed longitudinal chirp in grating include such as high single mode yield [131, 137, 141, 143], reduced spatial hole burning [15, 135, 139], narrower spectral linewidth [132, 136], and improved mode stability [17, 133, 134]. Negative impacts include, mode competing or beating [138, 140, 142] and so on. Of course, whether longitudinal chirp improves or deteriorates the device performance is directly related to its magnitude and how longitudinal chirp is applied on the grating as described in Muhammad Arif's paper [191]. According to this paper, longitudinal chirp between 0.0002 to $0.0003\Lambda_0$ should offer maximum threshold gain margin between the lasing mode and the next strongest mode, which is much higher than normal straight grating index-coupled DFBs and is desirable for breaking of DFB mode degeneracy. For this tunable device V9-18-9, the longitudinal chirp at different pump positions in GNC is in the range of 0.025% to 0.1% as shown in the Fig. 2.23, which is significantly larger than that mentioned in the paper for optimized threshold gain margin between the lasing mode and the next strongest one. We think what needs to be investigated in the future is to find the correlation

between longitudinal chirp and the gain margin or SMSR on device. Longitudinal chirp could be changed by pumping at different positions on device as shown in the Fig. 2.23 or pattern different chirped grating with different die tilting angle β as indicated by the Fig. 2.20. Other than discussion about threshold gain margin problem, this paper concluded that symmetrically chirped grating cavity (Minimum or maximum grating period locates at the middle of cavity.) should have the biggest gain margin for DFB lasers. The laser cavity defined by pump stripe in GNC on our present device is asymmetric, because the minimum grating period is along the straight line $v = tan(96°)u$, as shown in the Fig. 2.23 A). So we should also try to shift the die around accordingly in IL patterning and cleave some devices for symmetric cavity to check if the paper's conclusion still holds for our tunable device.

To the knowledge of the author, there is no report discussing lateral chirp in DFB lasers. It is because of our special IL fabrication of this hyperbolic grating for wavelength tuning purpose that requires us to consider or analyze lateral chirp's contribution to the device performance. For this particular device, V9-18-9, the lateral chirp across the pump stripe of 100 μm wide is about 0.08%, which is on the same order of longitudinal chirp along the pump stripe for cavity length of ∼2.51 mm in GNC. Lateral chirp's impact on our device performance can be summarized from three aspects. First, due to the existence of lateral chirp, grating period on one side of the pump stripe will be different that on the other side of the stripe. Assuming the effective refractive index is uniform across the pump stripe width, then the grating period difference across the pump stripe will select different lasing wavelengths. Previous device with straight grating has spectral linewidth of ∼0.34 nm at 3.5×threshold [128]. This is absolutely one of reasons why the spectral linewidth of device V9-18-9 is wide. Second, different grating lines hold different angles with respect to the pump stripe because of the lateral chirp, even though the pump stripe is oriented in so called grating normal configuration. As shown in the Fig. 4.3, this angle variation is ∼1° along the cavity. Although not large, angle variation together

with gain guiding from pump stripe in lateral direction support some cavity modes propagating not perfectly perpendicularly to the grating lines or zigzagging in the cavity which have slightly different wavelengths. The overall results of this situation will be wider spectral linewidth of the device. Third, this grating angle variation along pump stripe or cavity will lead to extra reflection and scattering losses from the grating lines and the induced spatial refractive index modulation (index mismatch) because of non-normal incidence that causes lights to leak from the sides of the laser cavity defined by pump stripe. The direct consequence of this is cavity loss will be higher than for a straight grating case. Indirect consequence could be wider spectral line width due to thermal issues and grater linewidth enhancement factor values from more intense pumping. Although lateral chirp might have these negative impacts on the performance of our device, it is required for wavelength tuning purpose. To decrease its impact on our tunable DFB laser device, an investigation about the spectral linewidth as pump stripe width should be conducted in future.

5.2.2 Further Increase Wavelength Tuning Range

As for further increasing the wavelength tuning range, what first needs to be done is to optimize the lateral chirps on a single device to fully take advantage of the material gain bandwidth. Of course, if the gain medium itself offers wider gain bandwidth for lasing beyond the potential tuning range by lateral chirp on single device, then a series of individual chirped grating DFB laser devices can be integrated together to a selectable DFB laser array as being implemented with QCL lasers. Simply speaking, this goal to wider tuning range involves both enhancing the tuning range from the lateral chirp in the grating and also the widen the bandwidth of the gain medium.

In Chapter 2, we have mentioned that lateral chirp could be further increased by tilting the die in IL with angle larger than the present value of 45°. As shown in

the Fig. 2.19, the grating period variation along straight line $v = tan(96°)u$ that we picked to represent grating lateral chirp increases from about 8% in the present case of β =45° to over 12% when β approaches 90°. Meanwhile the longitudinal chirp stays relatively low as reflected by Fig. 2.20. Both of these indicate the FOM of the grating at this larger die tilting angle will be very high and desirable for wavelength tuning purpose and without worry about not enough feedback from large longitudinal chirp in the laser cavity. Of course, it is impractical to have die tilting angle close to 90° in IL since not enough UV light will penetrate the PR layer to provide exposure with such a grazing incident angle. So considering a relatively practical case of die tilting angle, β=70°. As shown by the Fig. 2.19, the lateral chirp will have a increment of about 50% if β increases from 45° to 70°, which roughly means the present device wavelength tuning range at β=45° could be increased from ∼80 nm as measured to more than 120 nm if the gain medium bandwidth supports that and no other practical issues limit the improvement of tuning range. Compared with other work to be improved, this is definitely the relatively simple one and should be tried first.

With full potential of single device wavelength tuning range fulfilled as result of chirped grating optimization presented above, other work to do to further widen the wavelength tuning range would be improving the gain medium bandwidth. This was actually mentioned by the previous group member, Liang Xue in his dissertation too [128] through the development of a so called dual-wavelength emission approach [192]. Basically the two sets of electrically and optically isolated QWs with gain spectral peak shifted were grown in the active region of an optically pumped Mid-IR type-II laser. With this approach, the gain bandwidth was claimed to be ∼500 nm. Then to fully use the gain bandwidth, a selectable tunable DFB array could be fabricated in the same fashion as introduced in Chapter 1 with individual tunable DFBs having offset chirped grating to cover different tuning ranges. Compared with the implementation of with QCLs in the Chapter 1, this approach needs to equivalently shift the pump stripe at different location for wavelength tuning but

does not require the electronic driving circuitry, temperature control module for individual DFB laser and the multi-mode interface (MMI) to couple out light from individual device. Author thinks it's worth investigation.

5.2.3 Develop Better Simulation Model

At the moment, the simulation of our tunable DFB laser device presented in the dissertation is limited to a single function of determining the lasing wavelength also can not be applied for situations above threshold. Besides, due to some of simplification, the present simulation can not model the present device well enough. Even the lasing wavelength result from the simulation program shows discrepancy from the experimental measurement to some extent, as introduced in Chapter 4. So for the goal of better modeling the characteristics and comprehensive understanding of our devices, more comprehensive model has to be proposed for better mathematically approach the real device and actual operation conditions. As far as author knows, incorporating TMM with Green's function for laser cavity modeling and resonance as conducted by different researchers [173, 182, 193] and meanwhile taking into account of other other physical processes should be a feasible approach to achieve this goal. Considering the chirped grating we have on our device, recursive Green's function method (RGFM) [194] should be applied which is an algorithm for computing the Green's function of a large cavity with periodic or aperiodic grating based on the knowledge of Green's function of smaller sections of the cavity, the unit cell or single period of grating for instance. In each recursion step, the Green's functions corresponding to two adjoining sections are replaced with a single Green's function of the composite section. In this manner, recursion is going on until the Green's function for the whole cavity is solved. We hope that with this approach, simulations could be carried out for all different kinds of attributes of our device for better understanding of our tunable DFB laser device and offer guidance in device design

and determination of fabrication parameters. Particularly, this model should be also able to conduct lateral/longitudinal chirp parameters optimization or trade offs for device properties such as device threshold, lasing wavelength, threshold gain margin of the different possible mode if there are, spectral linewidth, coupling strength, side mode suppression ratio, intra-cavity electric field with potential spatial hole burning or saturate gain, static and dynamic performances and so on. This model is probably the most important task in future for this project.

5.2.4 Field Demonstration

Optically-pumped type-II DFB laser is a powerful tool for spectroscopic applications such as remote sensing thanks to its features including narrow spectral linewidth, high output power, good beam quality and broad wavelength tuning range. Together with the wavelength modulation technique developed especially for this type of optically pumped tunable DFB laser as explained in section 3.5.2.2, it should be able to achieve sensitivity of $\ll 1$ ppm. Despite the present device V9-18-9 does not lase in the range where methane has strong C-H stretch absorption lines to conduct a field test or demonstration, fabricate more tunable DFB laser devices with our technical approach or method presented in this dissertation to prove its application in remote sensing of methane or other trace gases should be carried out in future.

Appendices

Appendix A

Cartesian Coordinate System Rotation around One Axis

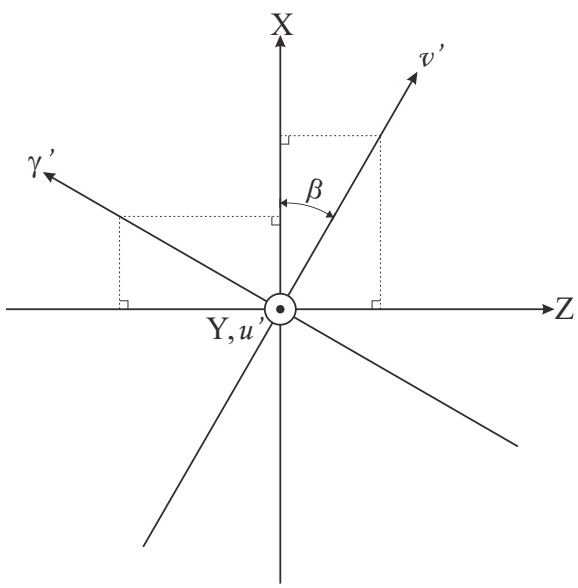

Figure A.1: Coordinate system rotation around one axis

As shown in the above Fig. A.1, when the coordinate system (X, Y, Z) rotates about Y axis for angle β to get new coordinate system (u', v', γ'), then the coordinates

X, Y and Z can be written in the expressions shown below in terms of the coordinates u', v' and γ'.

$$X = v' \cos\beta + \gamma' \sin\beta \tag{A.1a}$$

$$Y = u' \tag{A.1b}$$

$$Z = v' \sin\beta - \gamma' \cos\beta \tag{A.1c}$$

Rewrite the above expressions in matrix form, then we will get equation as shown below. It looks exactly as equation (2.10). Likewise, sample azimuthal rotation of angle α about axis γ' can be written as equation (2.11).

$$\begin{bmatrix} X \\ Y \\ Z \end{bmatrix} \equiv \begin{bmatrix} 0 & \cos\beta & \sin\beta \\ 1 & 0 & 0 \\ 0 & \sin\beta & -\cos\beta \end{bmatrix} \begin{bmatrix} u' \\ v' \\ \gamma' \end{bmatrix} = A_1 \begin{bmatrix} u' \\ v' \\ \gamma' \end{bmatrix} \tag{A.2}$$

Appendix B

Snell's Law With Complex Refractive Indices

Consider a wave propagating in a medium of complex index n_i incident on an interface to a medium of complex index n_t at an incident angle θ_i and refracted at angle θ_t as shown below.

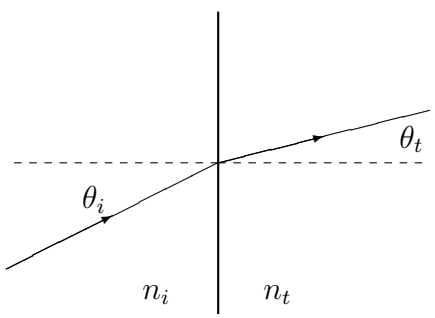

Snell's law states that $n_i \sin\theta_i = n_t \sin\theta_t$, in which case θ_t is given by the following equation.

$$\theta_t = \sin^{-1}\left(\frac{n_i}{n_t}\sin\theta_i\right) \tag{B.1}$$

We use the definition of sine as function of complex parameter z as

$$\sin^{-1} z = -j \ln \left(iz + \sqrt{1 - z^2} \right) \tag{B.2}$$

which gives the transmitted angle as

$$\theta_t = -j \ln \left[j \left(\frac{n_i}{n_t} \sin \theta_i \right) + \sqrt{1 - \left(\frac{n_i}{n_t} \sin \theta_i \right)^2} \right] \tag{B.3}$$

and then apply identity, $\ln z = \ln |z| + j \arg(z)$ which gives

$$\theta_t = -j \ln \sqrt{\left(\frac{n_i}{n_t} \sin \theta_i \right)^2 + 1 - \left(\frac{n_i}{n_t} \sin \theta_i \right)^2} + \arg \left[j \left(\frac{n_i}{n_t} \sin \theta_i \right) + \sqrt{1 - \left(\frac{n_i}{n_t} \sin \theta_i \right)^2} \right] \tag{B.4}$$

which could be simplifies as

$$\theta_t = \arg \left[\sqrt{1 - \left(\frac{n_i}{n_t} \sin \theta_i \right)^2} + j \frac{n_i}{n_t} \sin \theta_i \right]. \tag{B.5}$$

For example, if $\theta_i = 0°$, $\theta_t = \arg(1) = 0$, as expected. If $n_i = 1$, $n_t = 2$, and $\theta_i = 30°$, then

$$\theta_t = \arg \left[\sqrt{\frac{15}{16}} + \frac{j}{4} \right] = \tan^{-1}(1/\sqrt{15}) \approx 14.478°$$

which agrees with the value computed from Snell's law with real refractive indexes. If $n_i = 1$, $n_t = 1 + j$, and $\theta_i = 30°$, then

$$\begin{aligned} \theta_t &= \arg \left[\sqrt{1 - \left(\frac{1-j}{4} \right)^2} + j \frac{1-j}{4} \right] = \arg \left[\sqrt{1 + \frac{j}{8}} + \frac{j+1}{4} \right] \\ &= \arg \left[\frac{\sqrt{\sqrt{65} + 8} + 1}{4} + j \frac{\sqrt{\sqrt{65} - 8} + 1}{4} \right] \\ &\approx \arg \left[1.2519 + j 0.3124 \right] = \tan^{-1} \frac{0.3124}{1.2519} \approx 14.011° \end{aligned}$$

Finally, consider a case where $n_i = 1$, $n_t = 1 - j$, and $\theta_i = 30°$, in which case

$$\begin{aligned}\theta_t &= \arg\left[\sqrt{1 - \left(\frac{1+j}{4}\right)^2} + j\frac{1+j}{4}\right] = \arg\left[\sqrt{1 - \frac{j}{8}} + \frac{j-1}{4}\right] \\ &= \arg\left[\frac{\sqrt{\sqrt{65}+8}-1}{4} + j\frac{\sqrt{\sqrt{65}-8}+1}{4}\right] \\ &\approx \arg\left[0.7519 + j0.3124\right] = \tan^{-1}\frac{0.3124}{0.7519} \approx 22.562°\end{aligned}$$

We can conclude that waves are refracted strongly into a medium with index having positive imaginary part, and weakly into a medium having negative imaginary part.

Appendix C

Matlab Codes Used in Tunable DFB Laser Design

C.1 TE Mode Solver for 4-Layer Slab Waveguide

```
% this is the version of Yi-Fan Li and John W. Y. Lit's 4 layer slab
% waveguide, paper published in J. Opt. Soc. Am. A, page 671, Vol4,
% No.4/April 1987. Title: "General Formula for the Guiding Properties
%of a Multilayer Slab Waveguide"
clc;
close all;
% 1D 4layer slab waveguide parameters definition
% cover layer: air
% top clad layer: GaSb, refractive index:n_topclad; thickness:
% t_topclad=[half_t_core, half_t_core+t_topclad];
% core with gain: InGaSb/InAs refractive index: n_core; thickness:
% t_core=[-half_t_core, half_t_core]
```

```
% substrate: refractive index: n_sub; thickness: infinity
n_air=1;
n_topclad=3.82;
n_core=3.842;
n_sub=3.82;
t_topclad=1.5;      %unit: micrometer
half_t_core=0.75;   %unit: micrometer

% target wavelength and wavevector setting
lambda=3.06;        %unit: micrometer
k_lambda=2*pi/lambda;
k_z_step=0.001;
angle_cri=asind(n_topclad/n_core);
% just want to set the range of k_z that I need to go through for
%guided modes
k_z_ratio=cosd(angle_cri);
k_z=0:k_z_step:k_z_ratio*k_lambda*n_core;
% middle vaiables definition
%p+1 in paper
p_topclad=sqrt((n_core^2-n_topclad^2)*k_lambda^2-k_z.^2);
%p+2 in paper
p_air=sqrt((n_core^2-n_air^2)*k_lambda^2-k_z.^2);
%p-1 in paper
p_sub=sqrt((n_core^2-n_sub^2)*k_lambda^2-k_z.^2);
%phi-0 in paper
phi_n0=atan(p_sub./k_z);
%psi+1 in paper
psi_p1=p_topclad*t_topclad+atanh(p_air./p_topclad);
```

```
%phi+0 in paper
phi_p0=atan(p_topclad.*tanh(psi_p1)./k_z);
fun=k_z*2*half_t_core-phi_p0-phi_n0;
plot(k_z, fun, 'b', 'LineWidth', 1.5);
hold on;
hline=refline(0, 0);
set(hline, 'Color', 'r', 'LineWidth', 1.5);
set(gca, 'FontName', 'Times New Roman');
title('Graphic Solution of Eigenvalue Function of 4 Layer Slab...
Waveguide', 'FontSize', 16);
xlabel('k_z (1/\mum)', 'FontSize', 14);
ylabel('Left/Right HandSide Amplitude', 'FontSize', 14);
legend('Left Hand Side=k_z*Width_{core}-\Phi_{-0}-\Phi_{+0}',...
 'Right Hand Side=q\pi, q=0, 1, 2....', 'Location', 'nw');
TopCladStr=['TopClad=', num2str(t_topclad), '\mum'];
text(0.1, -0.5, TopCladStr, 'FontName', 'Times New Roman',...
 'FontSize', 12);
plot2svg('4LayerSlabWGEigenFunction.svg');
x_neg0=find(fun<=0, 1, 'last');
x_pos0=find(fun>=0, 1, 'first');
fprintf('Point Below Zero is: (%.7f, %.7f)\n', k_z(x_neg0),...
 fun(x_neg0));
fprintf('Point Above Zero is: (%.7f, %.7f)\n', k_z(x_pos0),...
 fun(x_pos0));
kz=(k_z(x_neg0)*fun(x_pos0)...
-k_z(x_pos0)*fun(x_neg0))/(fun(x_pos0)-fun(x_neg0));
fprintf('Zero is at: k_z=%.7f\n', kz);
Neff=sqrt(k_lambda^2*n_core^2-kz^2)/k_lambda;
```

```
fprintf('Effective refractive index is: %.7f\n', Neff);
figure (1);
figure (2);
%p+1 in paper
p_tc=sqrt((n_core^2-n_topclad^2)*k_lambda^2-kz^2);
%p+2 in paper
p_a=sqrt((n_core^2-n_air^2)*k_lambda^2-kz^2);
%p-1 in paper
p_s=sqrt((n_core^2-n_sub^2)*k_lambda^2-kz^2);
%psi+1 with solved kz
psi_p1_kz=p_tc*t_topclad+atanh(p_a/p_tc);
phi_n0_kz=atan(p_s/kz);
x_step=0.001;
t1=half_t_core+t_topclad;
x1=t1:x_step: 10;
E_air=cos(kz*2*half_t_core-phi_n0_kz)*...
cosh(p_tc*t_topclad-psi_p1_kz)*exp(-p_a*(x1-t1))/cosh(psi_p1_kz);
I_air=E_air.*conj(E_air);
Q_air=sum(I_air);
plot(x1, E_air, 'm', 'Linewidth', 1.5);
hold on;
x2=half_t_core:x_step:t1;
E_topclad=cos(kz*2*half_t_core-phi_n0_kz)*cosh(p_tc...
*(x2-half_t_core)-psi_p1_kz)/cosh(psi_p1_kz);
I_topclad=E_topclad.*conj(E_topclad);
Q_topclad=sum(I_topclad);
plot(x2, E_topclad, 'b', 'Linewidth', 1.5);
x3=-half_t_core:x_step:half_t_core;
```

```
E_core=cos(kz*(x3+half_t_core)-phi_n0_kz);
I_core=E_core.*conj(E_core);
Q_core=sum(I_core);
h=area(x3, E_core);
set(h,'FaceColor',[1 0 0], 'EdgeColor', 'r');
x4=-50:x_step:-half_t_core;
E_sub=cos(phi_n0_kz)*exp(p_s*(x4+half_t_core));
I_sub=E_sub.*conj(E_sub);
Q_sub=sum(I_sub);
plot(x4, E_sub, 'g', 'Linewidth', 1.5);
set(gca, 'FontName', 'Times New Roman');
xlabel('Z (\mum)','FontSize', 14);
ylabel('Electric Field Amplitude, |E_{  y}| (a.u.)', 'FontSize', 14);
title_str=['TE Mode Field Distribution of 4 Layer Slab Waveguide...
 @', num2str(lambda),'\mum'];
title(title_str, 'FontSize', 14);
topclad_str=['Top Clad: GaSb, n=', num2str(n_topclad),...
', ', num2str(t_topclad), '\mum'];
core_str=['Core: IA/InGaSb/InAs/IA, n=',num2str(n_core),...
 ', ', num2str(2*half_t_core), '\mum'];
substrate_str=['Substrate: GaSb, n=', num2str(n_sub)];
legend('Cover Layer: Air', topclad_str, core_str,...
 substrate_str, 'Location', 'Best');
Gamma=Q_core/(Q_air+Q_topclad+Q_core+Q_sub);
fprintf('Confinement Factor is: %f\n', Gamma);
NeffStr=['n_{Eff}=', num2str(real(Neff))];
GammaStr=['\Gamma=', num2str(Gamma)];
TextStr={NeffStr;GammaStr};
```

```
text(-45, 0.4, TextStr, 'FontName', 'Times New Roman', 'FontSize',...
 12);
plot2svg('TE Mode Distribution.svg');
```

C.2 Foci Locations Required for Chirped Grating Period Calculation

```
%version 1.0
%by Xiang He
%Could not get he rim and flat surface of the lens plot out in .svg
%file. So just comment out the statements in the Matlab code and
%manually add them in Inkscape. The file is still huge.
%%%%%%%%%%%%%%%%%%%%%%%%%%%%%%%%%%%%%%%%%%%%%%%%%%%%%%%%%%%%%%%%
%Coordinates:   Horizontal Axis is Z, Pointiing Right as Z Increcess
%               Vertical Axis is X, Pointing Up as X Increases
%%%%%%%%%%%%%%%%%%%%%%%%%%%%%%%%%%%%%%%%%%%%%%%%%%%%%%%%%%%%%%%%
clc;
close all;
clear all;
%spheric surface parameter definition
%%%%%%%%%%%%%%%%%MY LENS%%%%%%%%%%%%%%%%%
% R=38.6;           %unit: mm     Radius of the Front Spheric Surface
%of lens
% t_c=3.6;          %unit: mm     Center Thickness of the PlanoConvex
% Lens
% t_e=1.5;          %unit: mm     Edge Thickness of the PlanoConvex
%lens
```

```
%%%%%%%%%%%%%%%%%LIANG'S LENS%%%%%%%%%%%%%%%%%%%%%%%%
% R=18.0;           %unit: mm
% t_c=7.2;          %unit: mm
% t_e=2.0;          %unit: mm
%%%%%%%%%%%%%%%%%2 inch lens for tilted wafer exposure%%%%%%%%%%%%%%
R=51.5;         %unit: mm
t_c=10.0;       %unit: mm
t_e=3.3;        %unit: mm
%%%%%%%%%%%%%%%%%%%%%%%%%%%%%%%%%%%%%%%%%%%%%%%%%%%%%%
%Incident Beam's Angle, Corresponding to the Angle Reading on the
%Dial of the Rotation Stage Used for Grating Patterning
theta_in=21.7;
% theta_in=24.38;    %degree
%fused silica refractive index at 355nm
n_lens=1.476;
%PlanoConvex Lens CrossCut in X-Z Plane Plot
x=-t_c: R/100: -t_e;
y_p=sqrt(R^2-(x-R+t_c).^2);
fprintf('Half Aperature Phi/2=%f\n', max(y_p));
fprintf('Normals Angle Range=[%f, %f]\n', ...
atand(max(y_p)/(R-t_c+t_e)), 180+atand(-max(y_p)/(R-t_c+t_e)));
y_n=-sqrt(R^2-(x-R+t_c).^2);
%Plot Front Spheric Surfce of PlanoConvex Lens
plot(x, y_p, 'r', x, y_n, 'r', 'LineWidth', 1.5);
hold on;        %for lines plot
y=-max(y_p):max(y_p)/1000:max(y_p);
%Typical Incident Beam Lines Plot
%line euqations
```

```
x2=-20:0.01:2;
%Ramdomly Picked a Few Intercepts on X axis
intercept=-0.8*max(y_p):0.4*max(y_p):0.8*max(y_p);
%(Z, X) gives the cross point of the incident lines with the front
% spheric surface of the planoconvex lens
z=zeros(length(intercept), 1);
x=zeros(length(intercept), 1);
%K gives the slope of the normal of front spheric surface of the
%planoconvex lens at the specific cross points of the lines and
%surface (circle).
k=zeros(length(intercept), 1);
%incident angle of the lines at different cross points with respect
%to the normal at that point
angle_in=zeros(length(intercept), 1);
%transmitted angle after the incident goes in the planoconvex lens
%with respect to the normal at the cross point
angle_lens=zeros(length(intercept), 1);
%the slope of the diffracted incident lines when they propagate in
%the lens slope_lens=zeros(length(intercept), 1);
%the shift in X direction when these diffracted lines reach the back
%planar surface with respect to the x coordinates when they just
%enter the lens xshift_lens=zeros(length(intercept), 1);
x_out=zeros(length(intercept), 1);
%output angle of the lines when they go out of the back planar
% surface of the planoconvex lens
angle_out=zeros(length(intercept), 1);
%slope of these outgoing lens when they leave the back planar
%surface of the planoconvex lens
```

```
slope_out=zeros(length(intercept), 1);
x3=-12:0.01:5;
x4=-5:0.01:90;
LinesParameters=zeros(length(intercept), 2);
for i=1: length(intercept);
    plot(x2, tand(theta_in)*x2+intercept(i), 'g');
    %Get the Cross Points of Incident Lines with Front Spheric Lens
%Surface
    f=@(z)(z+t_c-R).^2+tand(theta_in)^2*z.^2+...
2*tand(theta_in)*intercept(i)*z+intercept(i)^2-R^2;
    %(Z(i), X(i)) Gives to the Coordinates of the Cross Point of Line
%with Intercept(i) and the Front Spheric Lens Surface;
    z(i)=fzero(f, [-t_c, -t_e]);
    x(i)=tand(theta_in)*z(i)+intercept(i);
    %K(i) Gives the Slope of the Normal at the Corss Point of (Z(i),
% X(i));
    k(i)=-x(i)/(R-t_c-z(i));
    %Depends on the Slope of Incident Lines and the Normals at Corss
    %Points, Calculate the Incident Angles at Different Cross Points
    if k(i)>tand(theta_in)
        angle_in(i)=atand((k(i)-tand(theta_in))/(1+tand(theta_in)...
*k(i)));
        angle_lens(i)=asind(sind(angle_in(i))/n_lens);
        slope_lens(i)=(k(i)-tand(angle_lens(i)))/(1+...
tand(angle_lens(i)*k(i)));
        x_out(i)=x(i)+abs(z(i))*slope_lens(i);
        plot(x3, slope_lens(i).*x3+x_out(i),'b');
        angle_out(i)=asind(n_lens*sind(atand(slope_lens(i))));
```

```
        slope_out(i)=tand(angle_out(i));
        plot(x4, slope_out(i).*x4+x_out(i),'m');
    elseif k(i)==tand(theta_in)
        angle_in(i)=atand(k(i));
        angle_lens(i)=0;
        slope_lens(i)=k(i);
        x_out(i)=x(i)+abs(z(i))*slope_lens(i);
        plot(x3, slope_lens(i).*x3+x_out(i),'b');
        angle_out(i)=asind(n_lens*sind(atand(slope_lens(i))));
        slope_out(i)=tand(angle_out(i));
        plot(x4, slope_out(i).*x4+x_out(i),'m');
    else
        angle_in(i)=atand((tand(theta_in)-k(i))/(1+...
tand(theta_in)*k(i)));
        angle_lens(i)=asind(sind(angle_in(i))/n_lens);
        slope_lens(i)=(tand(angle_lens(i))+k(i))/(1-...
tand(angle_lens(i)*k(i)));
        x_out(i)=x(i)+abs(z(i))*slope_lens(i);
        plot(x3, slope_lens(i).*x3+x_out(i),'b');
        angle_out(i)=asind(n_lens*sind(atand(slope_lens(i))));
        slope_out(i)=tand(angle_out(i));
        plot(x4, slope_out(i).*x4+x_out(i),'m');
    end;
    LinesParameters(i, 1)=slope_out(i);
    LinesParameters(i, 2)=x_out(i);
    fprintf('Intercept(%d)=%f:[Z=%f,X=%f],Angle_in=%f,...
x_out=%f,slope_out=%f\n', i, intercept(i), z(i), x(i),...
 angle_in(i), x_out(i),slope_out(i));
```

```
end;
axis equal;
grid on;
title('Foci Location by Ray Tracing', 'FontSize', 16, 'FontName',...
 'Times New Roman');
xlabel('Z (mm)', 'FontSize', 14, 'FontName', 'Times New Roman');
ylabel('Y (mm)', 'FontSize', 14, 'FontName', 'Times New Roman');
set(gca, 'FontName', 'Times New Roman');
plot2svg('FociLocationByRayTracing.svg');
figure (1);
figure (2);
hold on;
grid on;
for j=1: length(LinesParameters)-1
    for k=j+1: length(LinesParameters)
        par=[LinesParameters(j,1 ), -1; LinesParameters(k, 1), -1];
        incpt=[-LinesParameters(j, 2); -LinesParameters(k, 2)];
        crspt=par\incpt;
        scatter(crspt(1), crspt(2), 'x'); %,'DisplayName',...
[ '[', name ']']);
        fprintf('Line%d and line%d cross at (%.4f, %.4f).\n',...
 j, k, crspt(1), crspt(2));
    end;
end;
title('Scattering Plot of the Cross Points of Different Lines');
ylabel('x (mm)');
xlabel('z (mm)');
```

C.3 Quadratically Chirped Grating Period Contour on 10×10 mm Die

```
clc;
close all;
lambda=355;
%the half separation of the foci of the two incident interfering
%beams after the plano-convex lens
L=32.98;         %unit:mm;
%the distance of the line connecting two foci mentioned above to the
%surface of the to be exposed sample wafer surface.
D=76.47;        %unit:mm;
beta=45;            %unit: degree
C_x=0;              %unit: mm;
C_y=0;              %unit: mm;
C_z=2;              %unit: mm; I don't know if it should be negative.
% Rotation Angle in the to be exposed sample
alpha=6;            %unit: degree
%%%%%%%%%%%%Flipped the Sign Here%%%%%%%%%%%%%%%%
tic;
[u,v]=meshgrid(-5:0.01:5, 0:0.01:10);

X=v.*cosd(beta).*cosd(alpha)-u.*cosd(beta).*sind(alpha)+C_x;
Y=v.*sind(alpha)+u.*cosd(alpha)+C_y;
Z=v.*sind(beta).*cosd(alpha)-u.*sind(beta).*sind(alpha)+C_z;
f_l1=sqrt(X.^2+(Y+L).^2+(D-Z).^2);

f_l2=sqrt(X.^2+(Y-L).^2+(D-Z).^2);
```

```
Term1=(X.*cosd(beta).*cosd(alpha)+(Y+L).*sind(alpha)-...
(D-Z).*sind(beta).*cosd(alpha))./f_l1;
Term2=(X.*cosd(beta).*cosd(alpha)+(Y-L).*sind(alpha)-...
(D-Z).*sind(beta).*cosd(alpha))./f_l2;
Term3=(-X.*cosd(beta).*sind(alpha)+(Y+L).*cosd(alpha)+...
(D-Z).*sind(beta).*sind(alpha))./f_l1;
Term4=(-X.*cosd(beta).*sind(alpha)+(Y-L).*cosd(alpha)+...
(D-Z).*sind(beta).*sind(alpha))./f_l2;

pitch=lambda./sqrt((Term1-Term2).^2+(Term3-Term4).^2);
[C,h]=contour(u, v, pitch, 'LineWidth', 1.5);
clabel(C, h, 'labelspaciing', 200);
clabel(C, h, 'FontName', 'Times New Roman');
set(gca, 'FontName', 'Times New Roman');
axis square;

tiltangle=num2str(beta);
rotateangle=num2str(alpha);
Xoffset=num2str(C_x);
Yoffset=num2str(C_y);
Zoffset=num2str(C_z);

titlestr=['Contour of Grating Period on Die (nm)', ', \beta=',...
 tiltangle, '\circ, \alpha=', rotateangle, '\circ, C_x=', Xoffset,...
 'mm, C_y=', Yoffset, 'mm, C_z=', Zoffset, 'mm'];

title(titlestr, 'FontSize', 16, 'FontName', 'Times New Roman');
xlabel('u (mm)', 'FontSize', 14, 'FontName', 'Times New Roman');
```

```
ylabel('v (mm)', 'FontSize', 14, 'FontName', 'Times New Roman');
filename=['GratingPeriodContour_', 'Tilt', tiltangle, '_Rotate',...
 rotateangle', '_Cx', Xoffset, '_Cy', Yoffset, '_Cz', Zoffset,...
 '.svg'];
plot2svg(filename);
figure (1);
toc;
```

C.4 Contour of Chirped Grating Orientation on 10×10mm Die

```
clc;
close all;
lambda=355;
%the half separation of the foci of the two incident interfering
%beams after the plano-convex lens
L=32.98;         %unit:mm;
%the distance of the line connecting two foci mentioned above to the
%surface of the to be exposed sample wafer surface.
D=76.47;        %unit:mm;
beta=45;            %unit: degree
C_z=2;              %unit: mm
% Rotation Angle in the to be exposed sample
alpha=6;            %unit: degree
%%%%%%%%%%%%%%%%Flipped the Sign Here%%%%%%%%%%%%%%%%
tic;
% this is the (u, v) range on the whole die
```

```
[u,v]=meshgrid(-5:0.01:5, 0:0.01:10);
% this is the (u, v) range on the device cleaved from the middle
% from u=5:9 and v=-1.25:1.25mm
%Assume C_x=0, though it's not necessary to be ZERO
X=v.*cosd(beta).*cosd(alpha)-u.*cosd(beta).*sind(alpha);
%Assume C_y=0, though it's not necessary to be ZERO
Y=v.*sind(alpha)+u.*cosd(alpha);
Z=v.*sind(beta).*cosd(alpha)-u*sind(beta).*sind(alpha)+C_z;
f_l1=sqrt(X.^2+(Y+L).^2+(Z-D).^2);
f_l2=sqrt(X.^2+(Y-L).^2+(Z-D).^2);
% FRINGE EUQATION
Term1=(X.*cosd(beta).*cosd(alpha)+(Y+L).*sind(alpha)+...
(Z-D).*sind(beta).*cosd(alpha))./f_l1;
Term2=(X.*cosd(beta).*cosd(alpha)+(Y-L).*sind(alpha)+...
(Z-D).*sind(beta).*cosd(alpha))./f_l2;
Term3=(-X.*cosd(beta).*sind(alpha)+(Y+L).*cosd(alpha)+...
(D-Z).*sind(beta).*sind(alpha))./f_l1;
Term4=(-X.*cosd(beta).*sind(alpha)+(Y-L).*cosd(alpha)+...
(D-Z).*sind(beta).*sind(alpha))./f_l2;
% Grating Pitch Contour Plot first
pitch=lambda./sqrt((Term1-Term2).^2+(Term3-Term4).^2);
[C,h]=contour(u, v, pitch, 'LineWidth', 0.2);
clabel(C, h, 'labelspacing', 200, 'color', [0.8, 0.8, 0.8]);
axis equal;
hold on;
% Grating Line Orientation Contour overlayed on top of grating
%pitch plot.
[C, h]=contour(u, v, 180-atand((Term3-Term4)./(Term1-Term2)),...
```

```
 'LineWidth', 1.5);
% it looks weird, but i don't know why d(v)/d(u) does not carry sign
%with % it. and 180-atand is just make the orientation of the grating
%lines % actually tilt that many degrees as shown
clabel(C, h, 'FontName', 'Times New Roman');
axis tight;
title('Grating Line Orientation on 10\times10mm Die (\circ)',...
 'FontName', 'Times New Roman', 'FontSize', 16);
ylabel('v (mm)', 'FontName', 'Times New Roman', 'FontSize', 14);
xlabel('u (mm)', 'FontName', 'Times New Roman', 'FontSize', 14);
set(gca, 'FontName', 'Times New Roman');
figure (1);
toc;
```

References

[1] H. Kogelnik and C. Shank. Stimulated emission in a periodic structure. *Appl. Phys. Lett.*, 18:152–154, 1971.

[2] John Carroll, Jame Whiteway, and Dick Plumb. *Distributed Feedback Semiconductor Lasers*. IEE/SPIE Optical Engineering Press, 1998.

[3] Dr. H. Ghafouri-Shiraz. *Distributed Feedback Laser Diodes and Optical Tunable Filters*. John Wiley & Sons Ltd, The Atrium, Souther Gate, Chichester,, West Sussex PO19 8SQ, England, 2003.

[4] Toshiaki Suhara. *Semiconductor Laser Fundamentals*. Marcel Dekker, Inc., 270 Madison Avenue, New York, NY 10016, U. S. A., 2005.

[5] Jia-Ming Liu. *Photonic Devices*. Cambridge University Press, Cambridge, 2005.

[6] Ammon Yariv and Pochi Yeh. *Photonics–Optical Electronics in Modern Communications, 6th Edition*. Oxford University Press, Oxford New York, 2007.

[7] Frank Träger (Ed.). *Springer Handbook of Lasers and Optics*. Springer Science+Business Media, LLC., New York, 2007.

[8] Larry A. Coldren, Scott W. Corzine, and Milan L. Mašanović. *Diode Lasers and Photonic Integrated Circuits, 2Ed*. John WILEY & Sons, Inc., Hoboken, New Jersey, 2012.

[9] Klaus David, Geert Morthier, Patrick Vankwikelberg, and Roel G. Baets. Gain-coupled DFB lasers versus index-coupled and phase-shifted DFB lasers: A comparison based on spatical hole burning corrected yield. *IEEE J. Quantum Electron.*, 27(6):1714–1723, June 1991.

[10] Arthur J. Lowery and Dalma Novak. Performance comparison of gain-coupled and index-coupled DFB semiconductor lasers. *IEEE J. Quantum Electron.*, 30(9):2051–2063, Sep 1994.

[11] Claire Gmachl, Jerôme Faist, James N. Baillargeon, Federico Capasso, Carlo Sirtori, Deborah L. Sivco, George Chu, and Alfred Y. Cho. Complex-coupled quantum cascade distributed-feedback laser. *IEEE Photon. Technol. Lett.*, 9(8):1090–1092, August 1997.

[12] H. Kogelnik and C. V. Shank. Coupled mode theory of distributed feedback lasers. *J. Appl. Phys.*, 43:2327–2335, 1972.

[13] J. Kioshita and K. Matsumoto. Transient chirping in distributed-feedback (DFB) lasers: Effect of spatial hole-burning along the laser axis. *IEEE J. Quantum Electron.*, 24(11):2160–2169, November 1998.

[14] W. S. Rabinovich and B. J. Feldman. Spatial hole burning effects in distributed feedback lasers. *IEEE J. Quantum Electron.*, 25(1):20–30, January 1989.

[15] G. Morthier, k. David, P. Vankwikelberge, and R. Baets. A new DFB-laser diode with reduced spatial hole burning. *IEEE Photon. Technol. Lett.*, 2(6):388–390, June 1990.

[16] X. Pan, H. Olsen, and B. Tromborg. Spectral linewidth of DFB lasers including the effect of spatial hole burning and nonuniform current injection. *IEEE Photon. Technol. Lett.*, 2(5):312–315, 1990.

[17] P. Zhou and G. S. Lee. Mode selection and spatial hole burning suppression of a chirped grating distributed feedback laser. *Appl. Phys. Lett.*, 56:1400–1402, 1990.

[18] R. Schatz. Longitudinal spatial instability in symmetric semiconductor lasers due to spatial hole burning. *IEEE J. Quantum Electron.*, 28(6):1443–1449, June 1992.

[19] H. J. Wünsche, U. Bandelow, and H. Wenzel. Calculation of combined lateral and longitudinal spatial hole burning in $\lambda/4$ shifted DFB lasers. *IEEE J. Quantum Electron.*, 29(6):1751–1760, June 1993.

[20] T. Kimura and A. Sugimura. Coupled phase-shift distributed-feedback lasers for narrow linewidth operation. *IEEE J. Quantum Electron.*, 25(4):678–683, 1989.

[21] T. Kimura and A. Sugimura. Narrow linewidth asymmetric coupled phase-shift DFB lasers. *Trans. IEICE.*, 79(1):71–76, 1990.

[22] S. Ogita, Y. Kotaki, M. Hasuda, Y. Kuwahara, and H. Ishikawa. Long cavity multiple-phase shift distributed feedback laser diode for linewidth narrowing. *J. Lightwave Technol.*, LT-8(10):1596–1603, 1990.

[23] M. Aliannezhadi, F. Shahshahani, and V. Ahmadil. Improved performance of complex gain-coupled DFB laser by using tapered grating structure. *Opt. Quant. Electron*, 44:1–16, 2012.

[24] P. Werle. A review of recent advances in semiconductor laser based gas monitors. *Acta Crystallographica Section A*, 54:197–236, 1998.

[25] M. B. Frish, M. C. Ladder R. T. Wainner, A. O. Wright, A. H. Patel, J. Stafford-Evans, J. R. Morency, M. G. Allen, and B. D. Green. In *Proc. SPIE*, volume 6765, page 676506, 2007.

[26] H. Kroemer. Quasi-electric and quasi-magnetic fields in non-uniform semiconductors. *RCA Rev.*, 18:332–342, 1957.

[27] H. Kroemer. Theory of a wide-gap emitter for transistors. In *Proc. IRE*, volume 45, pages 1535–1537, 1957.

[28] H. Kroemer. A proposed class of heterojunction injiection lasers. In *Proc. IEEE*, volume 51, pages 1782–1783, 1963.

[29] Z. I. Alferov. (engl. transl. of sov. phys. semicond. **1** 358–61, 1967). *Fiz. Tekh. Poluprovodn.*, 1:436–8, 1966.

[30] Z. I. Alferov. *Sov. Phys. Solid State*, 9:208, 1967.

[31] Z. I. Alferov, V. M. Andreev, V. I. Korol'kov, E. L. Portnoi, and A. A. Yakovenko. (engl. transl. of sov. phys. semicond. **3** 785–7, 1970). *Fiz. Tekh. Poluprovodn.*, 3:930–3, 1969.

[32] Z. I. Alferov, V. M. Andreev, E. L. Portnoy, and M. K. Trukan. (engl. transl. of sov. phys. semicond. **3** 1107–10, 1970). *Fiz. Tekh. Poluprovodn.*, 3:1328–32, 1969.

[33] F. Bugge, G. Erbert, J. Fricke, S. Gramlich, R. Staske, H. Wenzel, U. Zeimer, and M. Weyers. 12W continuous-wave diode lasers at 1120 nm with InGaAs quantum wells. *Appl. Phys. Lett.*, 79:1965–1967, 2001.

[34] L. M. Dolginov, L. V. Druzhinina, P. G. Elisev, I. V. Kryukova, I. V. Leskovich, M. G. Milvidski, B. N. Sverdlov, and E. G. Shevchenko. Studies of laser action in InGaAsSb under electrical and electron beam excitation. *IEEE J. Quantum Electron.*, 13(8):609–611, 1977.

[35] A. E. Drakin, P. G. Eliseev, B. N. Sverdlov, A. E. Bochkarev, L. M. Dolginov, and L. V. Druzhinina. Study of double-hetrostruce LDs based on AlGaAsSb/InGa heterojunctions. *IEEE J. Quantum Electron.*, 23(6):1089–1094, 1987.

[36] A. E. Bochkarev, L. M. Doiginov, A. E. Drakin, P. G. Eliseev, and B. N. Sverdlov. First demonstratin of RT, CW LDs based on AlGaAsSb/InGaAsSb heterojunctions. In *Conf. Dig.of 11th IEEE Int. Semicond. Laser conf.*, volume Post-Deadline paper-8, 1988.

[37] H. K. Choi and S. J. Eglash. High-power multiple-quantum-well GaInAsSb/AlGaAsSb diode lasers emitting at 2.1 μm with low threshold current density. *Appl. Phys. Lett.*, 61:1154, 1992.

[38] D. Z. Garbuzov, R. U. Martinelli, H. Lee, R. J. Menna, P. K. York, L. A. DiMarco, M. G. Harvey, R. J. Matarese, S. Y. Narayan, and J. C. Connolly. 4 W quasi-continuous-wave output power from 2 μm AlGaAsSb/InGaAsSb single-quantum-well broadened waveguide laser diodes. *Appl. Phys. Lett.*, 70:2931, 1997.

[39] N. Bertru, A. Baranov, Y. Cuminal, G. Almuneau, F. Genty, A. Joullié, O. Brandt, A. Mazuelas, and K. H. Ploog. Long-wavelength (Ga, In)Sb/GaSb strained quantum well lasers grown by molecular beam epitaxy. *Semicond. Sci. Technol.*, 13:936–940, 1998.

[40] D. Z. Garbuzov, H. Lee, V. Khalfin, R. Martinelli, J. C. Connolly, and G. L. Belenky. 2.3-2.7-μm room temperature CW operation of InGaAsSb-AlGaAsSb broad waveduige SCH-QW diode. *IEEE Photon. Technol. Lett.*, 11:794–796, 1999.

[41] C. Lin, M. Grau, O. Dier, and M-C. Amann. Low threshold room-temperature continuous-wave operation of 2.24-3.04 μm GaInAsSb/AlGaAsSb quantum-well lasers. *Appl. Phys. Lett.*, 84:5088, 2004.

[42] T. Lehnhardt, M. Hümmer, K. Rößner, M. Müller, S. Höfling, and A. Forchel. Continuous wave single mode operation of GaInAsSb/GaSb quantum well lasers emitting beyond 3 μm. *Appl. Phys. Lett.*, 92:183508, 2008.

[43] M. Grau, C. Lin, O. Dier, C. Lauer, and M-C. Amann. Room-temperature operation of 3.26 μm GaSb-based type-I lasers with quinternary AlGaInAsSb barriers. *Appl. Phys. Lett.*, 87:241104, 2005.

[44] C. Grasse, K. Vizbaras, A. Andrejew, S. Sprengel, and M-C. Amann. Room-temperature GaSb-based quinternary type-I quantum-well lasers for the wavelength range from 3.3 to 3.6 μm. In *ESLW2001 Conference*, 2011.

[45] L. Shterengas, G. Belenky, T. Hosada, G. Kipshidze, and S. Suchalkin. Continuous wave operation of diode lasers at 3.36 μm at 12°C. *Appl. Phys. Lett.*, 93:011103, 2008.

[46] Y. Rouillard adn J. Koeth. *private communication*, 2010.

[47] E. Wintner and E. P. Ippen. Nonlinear carrier dynamics in $Ga_xIn_{1-x}As_yP_{1-y}$ compounds. *Appl. Phys. Lett.*, 44:999–1001, 1984.

[48] M. Takeshima. Effect of Auger recombination on laser operation in $Ga_{1-x}Al_xAs$. *J. Appl. Phys.*, 58:3846–3850, 1985.

[49] J. R. Meyer, C. L. Felix, W. W. Bewley, I. Vurgaftman, E. H. Aifer, L. J. Olafsen, J. R. Lindle, C. A. Hoffman, M. J. Yang, B. R. Bennett, B. V. Shanabrook, H. Lee, C. H. Lin, S. S. Pei, and R. H. Milles. Auger coefficients in type-II InAs/$Ga_{1-x}In_xSb$ quantum wells. *Appl. Phys. Lett.*, 73:2857–2859, 1998.

[50] R. F. Kazarinov and R. A. Suris. (engl. transl. of sov. phys. semicond. **5** 707, 1971). *Fiz. Tekh. Poluprovodn.*, 5:797, 1971.

[51] J. Faist, F. Capasso, D. L. Sivco, C. Sirtori, A. L. Hutchinson, and A. Y. Cho. Quantum cascade laser. *Science*, 265(5158):553–556, 1994.

[52] C. Gmachl, A. Tredicucci, F. Capasso, A. L. Hutchinson, D. L. Sivco, J. N. Baillargeon, and A. Y. Cho. High-power $\lambda \approx 8$ μm quantum cascade laser with near optimum performance. *Appl. Phys. Lett.*, 72:3130, 1998.

[53] S. Slivken, A. Evans, W. Zhang, and M. Razeghi. High-power, continuous-operation intersubband laser for wavelengths greater than 10 μm. *Appl. Phys. Lett.*, 90:151115, 2009.

[54] G. Scalari, C. Walther, M. Fischer, R. Terazzi, H. Beere, D. Ritchie, and J. Faist. THz and sub-THz quantum cascade lasers. *Laser Photon. Rev.*, 3:45, 2009.

[55] O. Cathabard, R. Teissier, J. Devenson, J. C. Moreno, and A. N. Baranov. Quantum cascade lasers emitting near 2.6 μm. *Appl. Phys. Lett.*, 96:141110, 2010.

[56] M. P. sEMTSIV, M. Wienold, S. Dressler, and W. T. Masselink. Short-wavelength (3.05 μm) inp-based strain-compensated quantum. *Appl. Phys. Lett.*, 90:051111, 2007.

[57] J. Devenson, O. Cathabard, R. Teissier, and A. N. baranov. InAs-based quantum-cascade lasers. In *Proc. SPIE*, volume 6909, page 69090U, 2008.

[58] S. Y. Zhang, D. G. Revin, J. W. Cockburn, K. Kennedy, A. B. Krysa, and M. Hopkinson. $\lambda \sim$3.1 μm room temperature InGaAs/AlAsSb/InP quantum cascade lasers. *Appl. Phys. Lett.*, 94:031106, 2009.

[59] S. Y. Zhang, D. G. Revin, J. P. Commin, K. Kennedy, A. B. Krysa, and J. W. Cockburn. Room temperature $\lambda \sim$3.3 μm InP-based InGaAs(Sb) quantum cascade lasers. *Electron. Lett.*, 46:439–440, 2008.

[60] J. S. Yu, A. Evans, S. Slivken, S. R. Darvish, and M. Razeghi. Temperature dependent characteristics of $\lambda \sim$3.8 μm room-temperature continuous-wave quantum-cascade lasers. *Appl. Phys. Lett.*, 88:251118, 2006.

[61] C. Gmachl, F. Capasso, A. Tredicucci, D. L. Sivco, R. Köhler, A. L. Hutchinson, and A. Y. Cho. Dependence of the device performance on the number of stages in quantum-cascade lasers. *IEEE J. Select. Topics Quantum Electron.*, 5:808, 1999.

[62] P. Q. Liu, A. J. hoffman, M. D. Escarra, K. J. Franz, J. B. khurgin, Y. Dikmelik, X. Wang, J-Y. Fan, and C. F. Gmachl. Highly power-efficient quantum cascade lasers. *Nat. Photon.*, 4:95–98, 2010.

[63] Y. Bai, S. Slivken, S. Kuboya, S. R. Darvish, and M. Razeghi. *Nat. Photon.*, 4:99–102, 2010.

[64] M. O. Manasreh. *Optoelectronics Properties of Semiconductors and Superlattices-Vol.3: Antimonide-Related Strained-Layer Heterostructures*. Amsterdam: Gordon and Breach, 1997.

[65] Rui Q. Yang. Infrared laser based on intersubband transitions in quantum wells. *Superlattices and Microstructures*, 17:97, 1995.

[66] C. H. Lin, R. Q. Yang, D. Zhang, S. J. Murry, S. S. Pel, A. A. Allerman, and S. R. Kurtz. Type-II interband quantum cascade laser at 3.8 μm. *Electron. Lett.*, 33:598, 1997.

[67] M. Kim, C. Canedy, W. W. Bewley, C. Kim, J. R. Lindle, J. Abell, I. Vurgaftman, and J. R. Meyer. Interband cascade laser emitting at λ=3.5 μm in continuous wave above room temperature. *Appl. Phys. Lett.*, 92:191110, 2008.

[68] A. Bauer, F. Langer, M. Dallner, M. Kamp, M. Motyka, G. Sek, K. Ryczko ad J. Misiewicz, S. Höfling, and A. Fochel. Emission wavelength tuning of interband cascade lasers in the 3–4 μm spectral range. *Appl. Phys. Lett.*, 95:251103, 2009.

[69] M. Kim, C. L. Canedy, C. S. Kim, W. W. Bewley, J. R. Lindle, J. Abell, I. Vurgaftman, and J. R Meyer. Room temperature interband cascade lasers. *Phys. Procedia*, 3:1195, 2010.

[70] M. Kim, W. W. Bewley, J. R. Lindle, C. Kim, C. L. Canedy, J. Abell, I. Vurgaftman, and J. R. Meyer. Extended tuning range in a distributed feedback ingaasp laser with sampled gratings. In *Laser Applications to Chemical, Security and Environmental analysis (San Diego, CA)(OSA Technical Digest Series(CD))*, volume LMA2, 2010.

[71] I. Vurgaftman, C. L. Canedy, C. S. Kim, M. Kim, W. W. Bewley, J. R. Lindle, J. Abell, and J. R. Meyer. Mid-infrared interband cascade lasers operating at ambient temperatures. *New J. Phys.*, 11:125015, 2009.

[72] A. Krier(Ed.). *Mid-infrared Semiconductor Optoelectronics*. Springer, 2006.

[73] M. Kamp, J. Hofmann, F. Schäfer, M. Reinhard, M. Fischer, T. Bleuel, J. P. Reithmaier, and A. Forchel. Lateral coupling - a material independent way to complex coupled DFB lasers. *Opt. Mater.*, 17:19–25, 2001.

[74] K. Kennedy, A. B. Krysa, J. S. Roberts, K. M. Groom, R. A. Hogg, D. G. Revin, L. R. Wilson, and J. W. Cockburn. Add-drop filters in three-dimensional layer-by-layer photonic crystals using waveguides and resonant cavities. *Appl. Phys. Lett.*, 89:201117, 2006.

[75] C. S. Kim, M. Kim, W. W. Bewley, J. R. Lindle, C. L. Canedy, J. Abell, I. Vurgaftman, and J. R. Meyer. Corrugated-sidewall interband cascade lasers with single-mode midwave-infrared emission at room temperature. *Appl. Phys. Lett.*, 95:231103, 2009.

[76] J. Faist, C. Gmachl, F. Capasso, C. Sirtori, D. L. Sivco, J. N. Baillargeon, and A. Y. Cho. Distributed feedback quantum cascade lasers. *Appl. Phys. Lett.*, 70:2670, 1997.

[77] N. Finger, W. Schrenk, and E. Gornik. Analysis of TM-polarized DFB laser structures with metal surface gratings. *IEEE J. Quantum Electron.*, 36:780, 2000.

[78] V. Jayaraman, D. A. Cohen, and L. A. Coldren. Extended tuning range in a distributed feedback ingaasp laser with sampled gratings. In *Presented at OFC'92*, volume WL12, 1992.

[79] V. Jayaraman adn A. Mathur, L. A. Coldren, and P. D. Dapkus. Very wide tuning range in sampled grating dbr laser. In *Presented at the 13th IEEE Laser Conf. '92*, volume PD-11, 1992.

[80] Suhyun Kim, Youngchul Chung, Su-Hwan Oh, and Moon-Ho Park. Design and analysis of widely tunable sampled grating DFB laser diode integrated with sampled grating distributed bragg reflector. *IEEE Photon. Technol. Lett.*, 16(1):15–17, JANUARY 2004.

[81] Y. Tohmori, F. Kano, H. Ishii, Y. Yoshikuni, and Y. Kondo. Wide tuning with narrow linewidth in DFB lasers with superstructure grating (SSG). *Electron. Lett.*, 29:1350–1352, 1993.

[82] H. P. Gauggel, H. Artmann, C. Geng, F. Scholz, and H. Schweizer. Wide-range tunability of GaInP-AlGaInP DFB lasers with superstructure gratings. *IEEE Photon. Technol. Lett.*, 9:14–16, 1997.

[83] I. A. Avrutsky, D. S. Ellis, A. Tager, H. Anis, and J. M. Xu. Design of widely tunable semiconductor lasers and concept of binary superimposed gratings (BSG's). *IEEE J. Quantum Electron.*, 34:729–741, 1998.

[84] M. Müller, M. Kamp F. Klopf, J. P. Reithmaier, and A. Forchel. Wide range tunable laterally coupled distributed-feedback lasers based on InGaAs-GaAs quantum dots. *IEEE Photon. Technol. Lett.*, 14:1246–1248, 2002.

[85] M. Bouda, M. Matsuda, K. Morito, S. Hara, T. Watanabe, T. Fujii, and Y. Kotaki. Compact high-power wavelength selectable lasers for WDM applications. In *Proc. OFC 2000*, volume 1, pages 178–180, 2000.

[86] N. Natakeyama, K. Kudo K. Naniwae, N. Suzuki, S. Ae S. Sudo, Y. Muroya, K. Yashiki, S. Satoh, T. Morimoto, K. Mori, and T. Sasaki. Wavelength-selectable microarray light sources for S-, C-, and L-band WDM systems. *IEEE Photon. Technol. Lett.*, 15:903–905, 2003.

[87] J. Heanue, E. Vail, M. Sherback, and B. Pezeshki. Widely tunable laser module using DFB array and MEMS selection with internal wavelength locker. In *Proc. OFC 2003*, volume 1, pages 82–83, 2003.

[88] Benjamin G. Lee, Mikhail A. Belkin, Ross Audet, Jim MacArthur, Laurent Diehl, Christian Pflügl, Federico Capasso, Douglas C. Oakley, David Chapman,

Antonio Napoleone, David Bour, Scott Corzine, Gloria Höfler, and Jérôme Faist. Widely tunable single-mode quantum cascade laser source for mid-infrared spectroscopy. *Appl. Phys. Lett.*, 91:231101, 2007.

[89] Hiroyuki Ishii, Kazuo Kasaya, Hiromi Oohashi, Yasuo Shibata, Hiroshi Yasaka, and Katsunari Okamoto. Widely wavelength-tunable DFB laser arrary integrated with funnel combiner. *IEEE J. Select. Topics Quantum Electron.*, 13(5):1089–094, SEPTEMBER 2007.

[90] C. Gmachl, R. Köhler, F. Capasso, A. Tredicucci, A. L. Ilutchinson, D. L. Sivco, J. N. Baillargeon, and A. Y. Cho. Single-mode, tunable quantum cascade distributed feedback (QC-DFB) lasers between 4.6 and 10 μm wavelength. In *CLEO 2000*, volume CWF1, page 264, 2000.

[91] C. J. Chang-Hasnain. Tunable VCSEL's. *IEEE J. Select. Topics Quantum Electron.*, 6:978–987, 2000.

[92] K. J. Knopp, D. Vakhshoori, P. D. Wang, M. Azimi, M. Jiang, P. Chen, Y. Matsui, K. McCallion, A. Baliga, F. Sakhitab, M. Letsch, B. Johnson, R. Zhu, and R. Gurjar. High power MEMS-tunable vertical-cavity surface-emitting lasers. In *Proc. Advanced Semiconductor Lasers, Dig. LEOS Summer topical Meet., Copper Mountain, CO.*, pages 31–32, 2001.

[93] A. Ouvrard, A. Garnache, L. Cerutti, F. Genty, and D. Romanini. Single-frequency tunable Sb-based VCSELs emitting at 2.3 μm. *IEEE Photon. Technol. Lett.*, 17(10):2020–2022, 2005.

[94] Maximilian Lackner, Michael Schwarzott, Franz Winter, Benjamin Kögel, Sandro Jatta, Hubert Halbritter, and Peter Meissner. CO and CO_2 spectroscopy using a 60 nm broadband tunable MEMS-VCSEL at 1.55 μm. *Opt. Lett.*, 31(21):3170–3172, Nov 2006.

[95] Karolina Zogal, Christian Gierl, Hooman Davani, Christian Grasse, Markus Maute, Peter Meissner, and Markus Amann. Tuning dynamics of a¿70nm continuously tunable MEMS-VCSEL with a hybrid curved mirror. In *Proceedings of CLEO/Europe and EQEC 2011 Conference Digest.*

[96] F. Taleb, C. Levallois, C. Paranthoen, J. P. Gauthier., N. Chevalier, M. Perrin., Y. Leger, O. De Sagazan, and A. Le Corre. VCSEL based on inas quantum-dashes with a lasing operation over a 117-nm wavelength span. *IEEE Photon. Technol. Lett.*, 25(21):2126–2128, Nov 2013.

[97] M. Ito and T. Kimura. Oscillation properties of AlGaAs DH lasers with an external grating. *Electron. Lett.*, 16:69–77, 1980.

[98] R. Wyatt and W. J. Devlin. 10 KHz linewidth 1.5 μm InGaAsP external cavity laser. *IEEE J. Quantum Electron.*, 19:110–112, 1983.

[99] B. Glance, C. A. Burrus, and L. W. Stulz. Fast frequency-tunable external-cavity laser. *Electron. Lett.*, 23:98–100, 1987.

[100] Y. Hori, H. Asakura, F. Sogawa, M. Kato, and H. Serizawa. External-cavity semiconductor laser with focusing grating mirror. *IEEE J. Quantum Electron.*, 26:1747–1755, 1990.

[101] R. Maulini, M. Beck, J. Faist, and E. Gini. Broadband tuning of external cavity bound-to-continuum quantum-cascade lasers. *Appl. Phys. Lett.*, 84:1659, 2004.

[102] G. Wysocki, R. F. Curl, F. K. Tittel, R. Maulini, J. M. Bulliard, and J. Faist. Widely tunable mode-hop free external cavity quantum cascade laser for high resolution spectroscopic applications. *Appl. Phys. B: Laser Opt.*, 81:769, 2005.

[103] R. Maulini, A. Mohan, M. Giovannini, J. Faist, and E. Gini. External cavity quantum-cascade laser tunable from 8.2 μm to 10.4 μm using a gain element with a heterogeneous cascade. *Appl. Phys. Lett.*, 88:201113, 2006.

[104] G. Wysocki, R. Lewicki., R. F. Curl, F. K. Tittel, L. Diehl, F. Capasso, M. Troccoli, G. Hofler, D. Bour, S. Corzine, R. Maulini, M. Giovannini, and J. Faist. Widely tunable mode-hop free external cavity quantum cascade lasers for high resolution spectroscopy and chemical sensing. *Applied Physics B*, 92(3):305–311, 2008.

[105] Andreas Hugi, romain Terazzi, Yargo Bonetti, Andreas Wittmann, Milan Fischer, Mattias Beck, Jerôme Faist, and Emilio Gini. External cavity quantum cascade laser tunable from 7.6 μm to 11.4 μm. *Appl. Phys. Lett.*, 95:061103, 2009.

[106] Yitang Dai and Jianping Yao. Numerical study of a DFB semiconductor laser and laser array with chirped structure based on the equivalent chirp technology. *IEEE J. Quantum Electron.*, 44(10):938–945, 10 2008.

[107] Andrew J. Ward, David J. Robbins, Giacinto Busico, Elena Barton, Lalitha Ponnampalam, Jeremy P. Duck, Neil D. Whitbread, Peter J. Williams, Douglas C. J. Reid, Andrew C. Carter, and Michael J. Wale. Widely tunable DS-DBR laser with monolithically integrated SOA: Design and performance. *IEEE J. Select. Topics Quantum Electron.*, 11:149–156, 1 2005.

[108] M. Öberg, S. Nilsson, K. Streubel, J. Wallin, L. Bäckbom, and T. Klinga. 74 nm wavelength tuning range of an InGaAsP/InP vertical grating assisted

codirectional coupler laser with rear sampled grating reflector. *IEEE Photon. Technol. Lett.*, 5:735–738, 1993.

[109] M. Öberg, P. J. Rigole, S. Nilsson, T. Klinga, L. Bäckbom, K. Streubel, J. Wallin, and T. Kjellberg. Complete single mode wavelength coverage over 40 nm with a super structure grating dbr laser. *J. Lightwave Technol.*, 13:1892–1898, 1995.

[110] P. J. Rigole, S. Nilsson, L. Bäckbom, T. Klinga, J. Wallin, B. Stålnacke, E. Berglind, and B. Stoltz. 114 nm wavelength tuning range of a vertical grating assisted codirectional coupler laser with a super structure grating distributed Bragg reflector. *IEEE Photon. Technol. Lett.*, 7:697–699, 1995.

[111] B. Broberg, P. J. Rigole, S. Nilsson, L. Andersson, and M. Renlund. Widely tunable semiconductor lasers. In *Proc. OFC/IOOC'99*, volume 2, pages 137–139, 1999.

[112] B. Pezeshki, E. Vail, J. Kubicky, G. Yoffe, S. Zou, J. Heanue, P. Epp, S. Rishton, D. Ton, B. Faraji, M. Emanuel, X. Hong, M. Sherback, V. Agrawal, C. Chipman, and T. Razazan. 20-mW widely tunable laser module using DFB array and MEMS selection. *PTL*, 14(10):1457–1459, Oct 2002.

[113] Yong-Duck Chung, Jae-Sik Sim, Sung-Bock Kim, and Jeha Kim. Wavelength-selectable 8-channel WDM optical transmitter. *JKPS*, 45(3):605–608, September 2004.

[114] Shiwei Bao, Yanping Xi, Sangzhi Zhao, and Xun Li. Sampled grating DFB laser array by periodic injection blocking. *IEEE J. Quantum Electron. Selected Topics*, 19(5):1–8, Sept 2013.

[115] S. T. Zhou, Z. Q. Lin, and W. S. C. Chang. Precise periodically control in the fabrication of holographic gratings. *Appl. Opt.*, 20:1270–1272, 1981.

[116] K. I. Hibino and Z. S. Hegedus. Hyperbolic holographic gratings: Analysis and interferomtric tests. *Appl. Opt.*, 33:2553–2559, 1994.

[117] K. I. Hibino and Z. S. Hegedus. Aberration compensation in a grating interferometer. *Appl. Opt.*, 33:4156–4163, 1994.

[118] J. Ferrera, M. L. Schattenburg, and H. I. Smith. Analysis of distortion in interferometric lithography. *J. Vac. Sci. Technol.*, B 14:4009–4013, 1996.

[119] J. R. Meyer, C. A. Hoffman, F. J. Bartoli, and L. R. Ram-Mohan. Type-II quantum-well lasers for the mid-wavelength infrared. *Appl. Phys. Lett.*, 67:757–759, 1995.

[120] A. K. Goyal, G. W. Turner, H. K. Choi, P. J. Foti, M. J. Manfra, T. Y. Fan, and A. Sanchez. Proc. IEEE LEOS 2000. volume 1, pages 249–250, 2000.

[121] R. Kaspi, A. P. Ongstad G. C. Dente, J. R. Chavez, M. L. Tilton, and D. M. Gianardi. High performance optically pumped antimonide lasers operation in the 2.4–9.3 μm wavelength range. *Appl. Phys. Lett.*, 88:041122, 2006.

[122] A. P. Ongstad, R. Kaspi, C. E. Moeller, M. L. Tilton, J. R. Chavez, and G. C. Dente. Gain and loss in an optically pumped mid-infrared laser. *J. Appl. Phys.*, 95:1619–1624, 2004.

[123] G. C. Dente. Low confinement factor for suppressed filaments in semiconductor lasers. *IEEE J. Quantum Electron.*, 37:1650–1653, 2001.

[124] R. Kaspi, A. Ongstad, C. Moeller, and G. C. Dente. Optically pumped integrated absorber 3.4 μm laser with InAs/InGaAsSb type-II transition. *Appl. Phys. Lett.*, 79:302–304, 2001.

[125] R. Kaspi, A. Ongstad, G. C. Dente, J. Chavez, M. L. Tilton, and D. Gianardi. High power and high brightness from an optical pumped InAs/InGaSb type-II midinfrared laser with low confinement. *Appl. Phys. Lett.*, 81:406–408, 2002.

[126] A. P. Ongstad, R. Kaspi, J. R. Chavez, G. C. Dente, M. L. Tilton, and D. M. Gianardi. High-temperature performance in $\sim$4 μm type-II quantum well laser with increased strain. *J. Appl. Phys.*, 92:5621–5626, 2002.

[127] A. P. Ongstad, R. Kaspi, M. L. Tilton, J. R. Chavez, and G. C. Dente. Performance composition of optically pumped type-II midinfrared lasers. *J. Appl. Phys.*, 98:043108, 2005.

[128] Liang Xue. Tunable high-power midwave-infrared distributed-feedback lasers. , 2009. Dissertation, The University of New Mexico.

[129] Yi-Fan Li and John W. Y. Lit. General formulas for the guiding properties of a multilayer slab waveguide. *J. Opt. Soc. Am. A*, 4(4):671–677, April 1987.

[130] A. M. Sarangan, W. P. Huang, G. P. Li, and T. Makino. Selection of transverse oscillation modes in tilted ridge DFB lasers. *J. Lightwave Technol.*, 14(8):1853–1858, 1996.

[131] Hart Hillmer and Bernd Klepser. Low-cost edge-emitting DFB laser arrays for DWDM communication systems implemented by bent and tilted waveguides. *IEEE J. Quantum Electron.*, 40(10):1377–1383, 2004.

[132] M. Okai, T. Tsuchiya, K. Uomi, N. Chinone, and T. Harada. Corrugation-pitch modulated MQW-DFB lasers with narrow spectral linewidth. *IEEE J. Quantum Electron.*, 27(6):1767–1772, 1991.

[133] P. Zhou and G. S. Lee. Phase-shifted distributed-feedback lasers with linearly chirped grating for narrow linewidth and high-power operation. *Appl. Phys. Lett.*, 58:331–333, 1991.

[134] P. Zhou and G. S. Lee. Mechanism of phase-shifted distributed-feedback laser with linearly chirped grating for stable-mode operation. *J. Appl. Phys.*, 70:1902–1904, 1991.

[135] A. Talneau, J. Charil, A. Ougazzaden, and J. C. Bouley. High power operation of phase-shifted DFB lasers with amplitude modulated coupling coefficient. *Electron. Lett.*, 28(15):1395–1396, 1992.

[136] M. Okai, M. Suzuki, and T. Taniwatari. Strained multiquantum-well corrugation-pitch-modulated distributed feedback laser with ultranarrow (3.6KHz) spectral linewidth. *Electron. Lett.*, 29(19):1696–1697, 1993.

[137] H. Hillmer, A. Grabmaier, S. Hansmann, and H.Burkhard. Continuously distributed phase shifts in chirped DFB lasers using bent waveguides. *Electron. Lett.*, 30(18):1483–1384, 1994.

[138] Yuan-Hwang Liao and H. G. Winful. Extremely high-frequency self-pulsation in chirped-grating distributed-feedback semiconductor lasers. *Appl. Phys. Lett.*, 69(20):2989–2991, 1996.

[139] H. Hillmer, A. Grabmaier, and H. Burkhard. Continuously distributed phase shifts by chirped distributed-feedback gratings for 1.55 μm distributed-feedback lasers. In *IEE Proc. Optoelectron.*, volume 14, pages 256–260, 1997.

[140] T. Fessant. Large signal dynamics of distributed feedback lasers with spatial modulation of their coupling coefficient and grating pitch. *Appl. Phys. Lett.*, 71(20):2880–2882, 1997.

[141] M. Arif and M. A. Karim. Threshold analysis of a chirped-grating distributed-feedback laser with the power series method. *Appl. Opt.*, 38(27):5775–5780, 1999.

[142] Kim A. Winick. Longitudinal mode competition in chirped grating distributed feedback lasers. *IEEE J. Quantum Electron.*, 35(10):1402–1411, 1999.

[143] M. Möhrle, A. Sigmund, R. Steingrüber, W. Fürst, and A. Suna. All-active tapered 1.55μm InGaAsP BH-DFB laser with continuously chirped grating. *IEEE Photon. Technol. Lett.*, 15(3):365–367, 2003.

[144] H. Hillmer, C. Prott, F. Römer, and S. Hansmann. Theoreticl model calculations of long-haul edge-emitting communication laser: Comparison of fractally mixed, fine-pitched and continuously chirped DFB gratings. *Semicond. Sci. Technol.*, 19(27):939–945, 2004.

[145] CVI Melles Griot Ltd. `https://www.cvimellesgriot.com/Products/Laser-Quality-Fused-Silica-Plano-Convex-Lenses.aspx`.

[146] CVI Melles Griot Ltd. `https://www.cvimellesgriot.com/Products/Documents/TechnicalGuide/Gaussian-Beam-Optics.pdf`. Eqn 2.33 on Page2.13.

[147] G. Morthier and P. Vankwikelberge. *Handbook of Distributed Feedback Diode Laser*. Artech House, 1997.

[148] C. S. Kim, M. Kim, W. W. Bewley, J. R. .Lindle, C. L. Canedy, I. Vurgaftman, and J. R. Meyer. Single-mode distributed-feedback interband cascade laser for the midwave infrared. *Appl. Phys. Lett.*, 88:191103, 2006.

[149] A. H. paxton and G. C. Dente. Filament formation in semiconductor laser gain regions. *J. Appl. Phys.*, 70:2921–2925, 1991.

[150] J. R. Marciante and G. P. Agrawal. Filament formation in semiconductor laser gain regions. *J. Appl. Phys.*, 32:590–596, 1996.

[151] J. R. Marciante and G. P. Agrawal. Spatio-temporal characteristics of filamentation in broad-area semiconductor lasers: Experimental results. *IEEE Photon. Technol. Lett.*, 10:54–56, 1998.

[152] S. A. Anson, J. T. Olesberg, M. E. Flatte, T. C. hasenberg, and T. F. Boggess. Differential gain, differential index, and linewidth enhancement factor for a 4 μm superlattice laser active layer. *J. Appl. Phys.*, 86:713–718, 1999.

[153] I. Vurgaftman, W. W. Bewley, R. E. Bartolo, C. L. Felix, M. J. Jurkovic, J. R. Meyer, M. J. Yang, H. Lee, and R. U. Martinelli. Far-field characteristics of mid-infrared angle-grating distributed feedback laser. *J. Appl. Phys.*, 88:6997–7005, 2000.

[154] M. Lerttamrab, S. L. Chuang, R. Q. Yang, and C. J. Hill. Linewidth enhancement factor of a type-II interband-cascade laser. *J. Appl. Phys.*, 96:3568–3570, 2004.

[155] K. Namjou, S. Cai, E. A. Whittaker, J. Faist, C. Gmachi, F. Capaso, D. L. Sivco, and A. Y. Cho. Sensitive absorption spectroscopy with a room-temperature distributed-feedback quantum-cascade laser. *Opt. Lett.*, 23:219–221, 1998.

[156] QCL based WMS. `http://www.ru.nl/tracegasfacility/trace_gas_research/experimental-setups/qcl-based-wms/`.

[157] I. D. Lindsay, P. GroBeta, C. J. Lee, B. Adhimolam, and K. J. Boller. Mid-infrared wavelength- and frequency modulation spectroscopy with a pump-modulated singly-resonant optical parametric oscillator. *Opt. Experss*, 14:12341–12346, 2006.

[158] D. D. Arslanov, M. Spunei, A. K. Y. Ngai, S. M. Cristescu, I. D. Lindsay, S. T. Persijn, K. J. Boller, and F. J. M. Harren. Rapid and sensitive trace gas detection with continuous wave optical parametric oscillator-based wavelength modulation spectroscopy. *Applied Physics B*, 103:223–228, 2011.

[159] P. Werle and F. Slemr. Signal-to-noise ratio analysis in laser absorption specrometers using optical multipass cells. *Appl. Opt.*, 30:430–434, 1991.

[160] David S. Bomse, Alen C. Stanton, and Joel A. Silver. Frequency modulation and wavelength modulation spectroscopies: comparison of exprimental methods using a lead-salt diode laser. *Appl. Opt.*, 31:718–731, 1992.

[161] Louis C. Philippe and Ronald K. Hanson. Laser diode wavelength-modulation spectroscopy for simultaneous measurement of temperature, pressure, and velocity in shock-heated oxygen flows. *Appl. Opt.*, 32:6090–6013, 1993.

[162] F. S. Pavone and M. Inguscio. Frequency- and wavelength-modulation spectroscopies: Comparisons of experimental methods using an AlGaAs diode laser. *Applied Physics B*, 56(2):118–122, February 1993.

[163] James M. Supplee, Edward A. Whittaker, and Wilfried Lenth. Theoretical description of frequency modulation and wavelength modulation spectroscopy. *Appl. Opt.*, 33:6294–6302, 1994.

[164] G. Hancock, J. H. Van Helden, R. Peverall, G. A. D. Ritchie, and R. J. Walker. Direct and wavelength modulation spectroscopy using a CW external cavity quantum cascade laser. *Appl. Phys. Lett.*, 94:201110–1–201110–3, 2009.

[165] Jayeeta Bhattacharyya, Sandip Ghosh, and B. M. Arora. Wavelength modulation spectroscopy using novel mechanical light chopper blade designs. *Review of Scientific Instruments*, 76:083903–1–083903–6, 2005.

[166] Xin Zhou. Diode-laser absorption sensors for combustion control. `http://hanson.stanford.edu/dissertations/Zhou_2005.pdf`, 2005. Dissertation.

[167] Tingdong Cai, Tu Tan, Guishi Wang, Weidong Chen, and Xiaoming Gao. Gas temperature measurements using wavelength modulation spectroscopy at 1.39 μm. *Optica Applicata*, XXXIX(1):13–29, 2009.

[168] Gregory Brian Rieker. Wavelength-modulation spectroscopy for measurements of gas temperature and concentration in harsh envrionments. `http://hanson.stanford.edu/dissertations/Rieker_2009.pdf`, 2009. Dissertation.

[169] T. Makino and J. Glinski. Transfer matrix analysis of the amplified spontaneous emission of DFB semiconductor laser amplifiers. *IEEE J. Quantum Electron.*, 24(8):1507–1518, Aug 1988.

[170] T. Makino. Transfer-matrix formulation of spontaneous emission noise of DFB semiconductor lasers. *J. Lightwave Technol.*, 9(1):84–91, Jan 1991.

[171] L. M. Zhang, S. F. Yu, M. C. Nowell, D. D. Marcenac, J. E. Carroll, and R. G. S. Plumb. Dynamic analysis of radiation and side-mode suppression in a second-order DFB laser using time-domain large-signal traveling wave model. *IEEE J. Quantum Electron.*, 30(6):1389–1395, Jun 1994.

[172] J. Hong, W. P. Huang, and T. Makino. Static and dynamic simulation for ridge-waveguide MQW DFB lasers. *IEEE J. Quantum Electron.*, 31(1):49–59, Jan 1995.

[173] J. D. Freeze, M. A. Jensen, and Richard H. Selfridge. A unified Green's function analysis of complicated DFB lasers. *IEEE J. Quantum Electron.*, 33(8):1253–1259, Aug 1997.

[174] Alain Champagne, J. Came, R. Maciejko, K. J. Kasunic, D. M. Adams, and B. Tromborg. Linewidth broadening in a distributed feedback laser integrated with a semiconductor optical amplifier. *IEEE J. Quantum Electron.*, 38(11):1493–1502, Nov 2002.

[175] K. Paschke, A. Bogatov, F. Bugge, A. E. Drakin, J. Fricke, R. Guther, A. A. Stratonnikov, H. Wenzel, G. Erbert, and G. Trankle. Properties of ion-implanted high-power angled-grating distributed-feedback lasers. *IEEE J. Quantum Electron. Selected Topics*, 9(5):1172–1178, Sept 2003.

[176] H. Wenzel, R. Guther, A. M. Shams-Zadeh-Amiri, and P. Bienstman. A comparative study of higher order Bragg gratings: coupled-mode theory versus mode expansion modeling. *IEEE J. Quantum Electron.*, 42(1):64–70, Jan 2006.

[177] J. Hong, Weiping Huang, and T. Makino. On the transfer matrix method for distributed-feedback waveguide devices. *J. Lightwave Technol.*, 10(12):1860–1868, December 1992.

[178] Stefan Hansmann. Transfer matrix analysis of the spectral properties of complex distributed feedback laser structures. *IEEE J. Quantum Electron.*, 28(11):2589–2595, November 1992.

[179] Toshihiko Makino. Transfer-matrix theory of modulation and noise of multi-element semiconductor lasers. *IEEE J. Quantum Electron.*, 29(11):2762–2770, Novenmber 1993.

[180] Toshihiko Makino. Threshold condition of DFB semiconductor lasers by the local-normal-mode transfer-matrix method: Correspondence to the coupled-wave method. *J. Lightwave Technol.*, 12(12):2092–2099, December 1994.

[181] T. Makino, H. Lu, and G. P. Li. Transfer-matrix dynamic model of partly gain-coupled 1.55 μm DFB lasers with a strained-layer MQW active grating. *IEEE J. Quantum Electron.*, 30(11):2443–2448, November 1994.

[182] T. Makino. Transfer matrix method with applications to distributed feedback optical devices. *Progress In Electromagnetics Research*, PIER 10:271–319, 1995.

[183] Drew N. Maywar and Govind P. Agrawal. Transfer-matrix analysis of optical bistability in DFB semiconductor laser amplifiers with nonuniform gratings. *IEEE J. Quantum Electron.*, 33(11):2029–2037, November 1997.

[184] Ahmed A. Abouelsaood. A rigorous, couple-wave transfer matrix method for two-dimensional threshold analysis of distributed feedback semiconductor lasers. 3:67–80, 2004.

[185] William Streifer, D. R. Scifres, and R. Burnham. Coupled wave analysis of DFB and DBR lasers. *IEEE J. Quantum Electron.*, 13(4):134–141, Apr 1977.

[186] P. Verly, R. Tremblay, and J. W. Y. Lit. Application of the effective-index method to the study of distributed feedback in corrugated waveguides. TE polarization. *J. Opt. Soc. Amer.*, 70(8):964–968, August 1980.

[187] J. Buus. The effective index method and its application to semiconductor lasers. *IEEE J. Quantum Electron.*, 18(7):1083–1089, Jul 1982.

[188] Makoto Yamada and Kyohei Sakuda. Analysis of almost-periodic distributed feedback slab waveguides via a fundamental matrix approach. *Applied Optics*, 26(16):3474–3478, August 1987.

[189] G. Millot, B. Lavorel, and J. I. Steinfeld. Collision broadening, line shifting, and line mixing in the stimulated raman $2\nu 2$ Q branch of CH_4. *J. Chem. Phys.*, 95:7938–7946, 1991.

[190] A. S. Pine. Self-, N_2, O_2, H_2, Ar, and He broadening in the $\nu 2$ band Q branch of CH_4. *J. Chem. Phys.*, 97:773–785, 1992.

[191] Muhammad Arif and Mohammad A. Karim. Threshold analysis of a chirped-grating distributed-feedback laser with the power series method. *Applied Optics*, 38(27):5775–5780, Sep 1999.

[192] R. Kaspi, A. P. Ongstad, G. C. Dente, M. L. Tilton, and A. Tauke-Pedretti. Optically pumped mid-Infrared laser width simultaneous dual-wavelength emission. *IEEE Photon. Technol. Lett.*, 20:1467–1469, 2008.

[193] Keith B. Kahen. Analysis of distributed-feedback lasers using a recursive green's functional approach. *IEEE J. Quantum Electron.*, 33(8):1253–1259, August 1997.

[194] D. J. Thouless and S. Kirkpatrick. Conductivity of the disordered linear chain. C14:235–245, 1981.